TU Delft

Delft University of Technology

Flip-Chip Optomechanics

Cooling Mechanics and Mitigating Noise with Feedback and Nonlinearity

van Soest, J. P.

DOI
10.4233/uuid:6cccd808-a2ac-4f8a-8cca-431dfc0ad6dc

Publication date
2025

Document Version
Final published version

Citation (APA)
van Soest, J. P. (2025). *Flip-Chip Optomechanics: Cooling Mechanics and Mitigating Noise with Feedback and Nonlinearity*. [Dissertation (TU Delft), Delft University of Technology].
https://doi.org/10.4233/uuid:6cccd808-a2ac-4f8a-8cca-431dfc0ad6dc

Important note
To cite this publication, please use the final published version (if applicable).
Please check the document version above.

Copyright
Other than for strictly personal use, it is not permitted to download, forward or distribute the text or part of it, without the consent of the author(s) and/or copyright holder(s), unless the work is under an open content license such as Creative Commons.

Takedown policy
Please contact us and provide details if you believe this document breaches copyrights.
We will remove access to the work immediately and investigate your claim.

This work is downloaded from Delft University of Technology.
For technical reasons the number of authors shown on this cover page is limited to a maximum of 10.

Flip-Chip Optomechanics

Cooling Mechanics and Mitigating Noise with Feedback and Nonlinearity



Jean-Paul van Soest

Flip-Chip Optomechanics

Cooling Mechanics and Mitigating Noise
with Feedback and Nonlinearity

Flip-Chip Optomechanics

Cooling Mechanics and Mitigating Noise
with Feedback and Nonlinearity

Dissertation

for the purpose of obtaining the degree of doctor
at Delft University of Technology
by the authority of the Rector Magnificus, Prof.dr.ir. T.H.J.J. van der Hagen
chair of the Board for Doctorates
to be defended publicly on
Thursday 20 November 2025 at 10:00 o'clock

by

Jean-Paul van Soest

Master of Science in Physics,
Leiden University, the Netherlands
born in Zaanstad, the Netherlands

This dissertation has been approved by the promotors.

Composition of the doctoral committee:

Rector Magnificus,	chairperson
Prof.dr. G.A. Steele	Delft University of Technology, promotor
Prof.dr. S. Gröblacher	Delft University of Technology, promotor

Independent members:

Prof.dr. W. Wieczorek	Chalmers University of Technology, Sweden
Prof.dr. S. Deléglise	Sorbonne University, France
Prof.dr. P.G. Steeneken	Delft University of Technology, the Netherlands
Dr.ir. B.J. Hensen	Leiden University, the Netherlands
Dr. R.A. Norte	Delft University of Technology
Prof.dr.ir. H.S.J. van der Zant	Delft University of Technology, reserve member





Copyright © 2025 by Jean-Paul van Soest

ISBN 978-94-6384-864-0

An electronic version of this dissertation is available at
http://repository.tudelft.nl/.

for Inês & Emily

Contents

Summary xi

Samenvatting xiii

1 Introduction 1
- 1.1 History of the Study of Radiation Pressure . . . 2
- 1.2 Modern Cavity Optomechanics . . . 2
- 1.3 Motivation for Flip-Chip Optomechanics . . . 4
- 1.4 Thesis Structure . . . 5

2 Theory and Background 7
- 2.1 Mechanical Harmonic Oscillators . . . 8
  - 2.1.1 Classical Harmonic Motion . . . 8
  - 2.1.2 Mechanical Harmonic Oscillator Quantization . . . 10
  - 2.1.3 Mode Shapes and Effective Mass . . . 12
  - 2.1.4 Mechanical Loss Mechanisms . . . 13
  - 2.1.5 Mechanical Dissipation Dilution and Phononic Shield Isolation . . . 14
- 2.2 Electromagnetic Harmonic Oscillators . . . 15
  - 2.2.1 Simple Electromagnetic Harmonic Oscillator . . . 15
  - 2.2.2 Circuit Quantization . . . 17
  - 2.2.3 Microwave Resonators . . . 18
  - 2.2.4 Microwave Loss Channels . . . 18
- 2.3 Optomechanical Coupling . . . 19

3 Design and Fabrication 23
- 3.1 Microwave Chip . . . 24
  - 3.1.1 Design and Simulation of the Microwave Circuit . . . 24
  - 3.1.2 Nanofabrication Techniques . . . 30
- 3.2 Membrane Chip . . . 42
  - 3.2.1 Phononic Shield Design . . . 42
  - 3.2.2 Membrane Chip Fabrication . . . 44
- 3.3 Optomechanical Flip-Chip Device . . . 45
  - 3.3.1 Design of the Flip-Chip Holder . . . 45
  - 3.3.2 Flip-Chip Assembly . . . 47
- 3.4 Cryogenic Setup . . . 48
  - 3.4.1 Vibration Isolation . . . 48
  - 3.4.2 Wiring and Measurement Setup . . . 51

4 Multitone Microwave Frequency Locking to a Noisy Cavity via Real-Time Feedback 53
4.1 Introduction . . . 54
4.2 Experimental Setup . . . 54
4.3 Feedback System . . . 56
4.4 Noise Reduction . . . 57
4.5 Multitone Locking . . . 59
4.6 Optomechanical Experimental Validation . . . 61
4.7 Conclusions . . . 62
4.8 Supplementary Information . . . 63
4.8.1 Homodyne Phase Matching . . . 63
4.8.2 Spectral Density Calibration . . . 64

5 Subtleties in Optomechanical Sideband Cooling and Calibration of a Mechanical Resonator 67
5.1 Introduction . . . 68
5.2 Experimental Setup . . . 69
5.3 Dynamical Backaction . . . 70
5.4 Thermal Calibration of the Mechanical Mode . . . 72
5.5 Cooling the Mechanical Mode . . . 75
5.6 Conclusion & Discussion . . . 77
5.6.1 Contributions . . . 78
5.7 Supplementary Information . . . 79
5.7.1 Measurement Setup . . . 79
5.7.2 The Optomechanical Cavity . . . 79
5.7.3 OMIT Fitting Routine . . . 83
5.7.4 Further Discussion on Thermal Calibration . . . 84
5.7.5 Mechanical Noise Fitting Routine . . . 84

6 Suppressing Cavity Frequency Noise Using a Kerr Nonlinearity 89
6.1 Introduction . . . 90
6.2 Experimental Setup . . . 91
6.3 Dispersive Cavity-Qubit Coupling . . . 92
6.4 Kerr Locking the Nonlinear Cavity . . . 94
6.5 Discussion & Outlook . . . 96
6.5.1 Contributions . . . 97
6.5.2 Acknowledgments . . . 97
6.6 Supplementary Information . . . 98
6.6.1 Measurement Setup . . . 98
6.6.2 The Microwave Resonances . . . 98
6.6.3 Interchip Distance Estimation . . . 102
6.6.4 Signal and Idler Resonances . . . 104

7 Conclusion & Outlook 107
7.1 Feedback Locking a Noisy Microwave Cavity . . . 108
7.2 Linear and Nonlinear Flip-Chip Devices . . . 109
7.3 Future Nonlinear Optomechanical Experiments . . . 110

Acknowledgements **113**

Curriculum Vitæ **117**

List of Publications **119**

Bibliography **121**

Summary

Detecting and influencing the motion of mechanical resonators has been a major topic in the study of fundamental physics and sensor technology. Optomechanical systems are particularly suitable for this due to their flexibility in design, causing them to be applicable in a wide range of parameter regimes. However, for all optomechanical systems there is a long-standing challenge to increase the single photon coupling strength. Whereas there are many ongoing developments in the field of linear optomechanics, there has been an increasing interest in nonlinear optomechanical systems. Namely, as this is a requirement for the creation of a massive superposition state in these platforms, treading the boundary between quantum mechanics and general relativity.

In this thesis we couple a mesoscopic membrane to a superconducting microwave cavity in a flip-chip geometry. The silicon nitride membrane is embedded inside an in-substrate phononic shield. Its resonance mode has a large effective mass, while retaining a considerable zero-point fluctuation, making it an excellent candidate for gravitational quantum experiments. Developing this platform, we overcome multiple challenges, such as mitigating noise and increasing the single photon coupling rate. Furthermore, we include a nonlinearity by coupling a cavity to a superconducting qubit, taking a first step towards nonlinear optomechanical experiments in a flip-chip system.

Chapter 1 will provide a broad introduction to the field of optomechanics. Starting with the history of the study of radiation pressure, it describes its development into the modern field of cavity optomechanics. Furthermore, we will discuss an outlook of prospective research directions.

Chapter 2 gives the theoretical foundation necessary for the understanding of the physics in the systems studied in this thesis. The mechanical and electromagnetic harmonic oscillator are treated, building up from the classical view to the quantum mechanical interpretation. Moreover, the parametric coupling of these two systems is discussed, leading to the optomechanical interaction.

In **Chapter 3** we describe the design, simulation and nanofabrication techniques used in this thesis. We discuss in detail the microwave and membrane chips, and the assembly of the nonlinear flip-chip device. We conclude with an illustration of the cryogenic setups used for the experiments.

Chapter 4 introduces the experimental challenge of cavity fluctuations. We present a dynamic feedback system implemented by the locking of a microwave drive to the cavity, removing low-frequency noise. This scheme is then scaled to

enable multitone experiments locked to the same feedback signal. This technique's application is demonstrated by observing optomechanically induced transparency in a locked cavity.

In **Chapter 5** we measure the mechanical properties of an optomechanical device. The membrane mode is cooled using a multitone sideband driving scheme. We highlight the subtleties and assumptions necessary for the calibration of the mechanical mode temperature and discuss a general calibration procedure.

In **Chapter 6** we present a flux-tunable nonlinearity in a flip-chip device. A microwave cavity is coupled to a superconducting qubit. The nonlinear cavity experiences frequency noise, which is mitigated by Kerr locking to a microwave tone. Signal and idler modes emerge, which are stabilized against low-frequency noise.

Finally, **Chapter 7** concludes the work performed in this thesis. The main findings are discussed and an outlook for further research in the field of nonlinear optomechanics is provided.

Samenvatting

Het detecteren en beïnvloeden van de beweging van mechanische resonatoren is een groot onderwerp in de studie naar fundamentele natuurkunde en in de sensor technologie. Optomechanische systemen zijn hiervoor uitermate geschikt door de flexibiliteit in hun ontwerp, waardoor ze toepasbaar zijn in een wijd scala aan parameterregimes. Echter, voor alle optomechanische systemen is er de uitdaging om de koppelingssterkte van een enkel foton te versterken. Terwijl er voortdurend veel ontwikkelingen zijn in het veld van lineaire optomechanica is er een groeiende interesse in niet-lineaire optomechanische systemen. Dit is namelijk een vereiste voor het creëren van een massieve superpositietoestand in deze platformen, wat zich bevindt op het snijvlak van kwantummechanica en de algemene relativiteitstheorie.

In dit proefschrift koppelen we een mesoscopisch membraan aan een supergeleidende microgolf trilholte in een flip-chip geometrie. Het membraan van siliciumnitride bevindt zich binnen een akoestisch kristal in het substraat. Zijn resonantie heeft een grote effectieve massa, terwijl het een aanzienlijke nulpuntsfluctuatie behoudt, waardoor dit een uitstekende kandidaat is voor kwantumexperimenten beïnvloed door gravitatie. Tijdens het ontwikkelen van dit platform zijn meerdere uitdagingen aangepakt, zoals het verminderen van ruis en het versterken van de enkel-foton koppelingssterkte. Daarnaast voegen we een niet-lineariteit toe door een trilholte te koppelen aan een supergeleidende qubit, waarmee we de eerste stap nemen voor niet-lineaire optomechanische experimenten in een flip-chip systeem.

Hoofdstuk 1 geeft een brede introductie op het gebied van optomechanica. Beginnend met de historie van de studie naar stralingsdruk wordt de ontwikkeling van het moderne onderzoeksveld van optomechanica met resonatoren beschreven. Daarnaast worden vooruitzichten naar toekomstige onderzoeksrichtingen behandeld.

Hoofdstuk 2 geeft de theoretische grondslag die nodig is voor het begrijpen van de natuurkunde die plaatsvindt in de systemen in dit proefschrift. De mechanische en elektromagnetische harmonische oscillator worden behandeld, opbouwend vanuit het klassieke oogpunt naar de kwantummechanische interpretatie. Verder wordt de parametrische koppeling van deze twee systemen besproken, wat leidt tot de optomechanische interactie.

In **Hoofdstuk 3** beschrijven we het ontwerp, de simulatie en de nanofabricagetechnieken die gebruikt zijn in dit proefschrift. We behandelen in detail de microgolf en membraan chips, en de montage van het niet-lineaire flip-chip apparaat. Tot slot illustreren we de cryogene opstellingen die gebruikt zijn voor de experimenten.

Hoofdstuk 4 introduceert de experimentele uitdaging van fluctuaties van de trilholte. We presenteren een dynamisch terugkoppelingssysteem, geïmplementeerd door het linken van een microgolf aandrijftoon aan de trilholte. Hiermee wordt laagfrequente ruis verwijderd. Deze regeling wordt daarna opgeschaald voor het in staat stellen van experimenten met meerdere tonen gelinkt aan hetzelfde terugkoppelingssignaal. De toepassing van deze techniek wordt gedemonstreerd door middel van de observatie van optomechanisch geïnduceerde transparantie in een gelinkte trilholte.

In **Hoofdstuk 5** meten we de mechanische eigenschappen van een optomechanisch apparaat. De resonantie van het membraan wordt gekoeld door middel van een zijbandaandrijfschema. We benadrukken de subtiliteiten en de aannames die nodig zijn voor de temperatuurkalibratie van de mechanische trilling en behandelen een algemeen kalibratieproces.

In **Hoofdstuk 6** presenteren we een flux-afstembare niet-lineariteit in een flip-chip apparaat. Een microgolf trilholte is gekoppeld aan een supergeleidende qubit. De niet-lineaire trilholte ondergaat frequentiefluctuaties, wat verholpen wordt door middel van het Kerr-vergrendelen aan een microgolftoon. Signal en idler resonanties ontstaan die gestabiliseerd zijn tegen laagfrequente ruis.

Tot slot, in **Hoofdstuk 7** wordt het uitgevoerde werk in dit proefschrift samengevat. De belangrijkste bevindingen worden besproken en er worden vooruitzichten geboden voor verder onderzoek op het gebied van niet-lineaire optomechanica.

1

Introduction

This chapter provides a brief historical overview of the study of radiation pressure and presents the accomplished achievements in the field of optomechanics. Moreover, we focus on the challenges and prospects of linear and nonlinear optomechanical research. The chapter concludes with the structure of this thesis.

1

1.1. History of the Study of Radiation Pressure

The idea whether two fundamental substances, light and matter, can interact with each other has intrigued scientists for hundreds of years. Its discovery has improved our understanding of the physics in the world around us and has lead to applications from quantum sensing to light sail spacecrafts [1–4].

Already in the early 17th century, when studying the trajectories of comets, Kepler observed that their dust tails always point away from the sun. He postulated that therefore a force must be acting on the matter [5]. More than two hundred years later Maxwell formulated that light must possess the property of momentum and can therefore exert a pressure on a surface [6]. This was later independently proven experimentally by Lebedew, and by Nichols and Hull [7, 8]. Einstein then formulated the statistics of this radiation pressure exchanging energy with a movable mirror [9]. The invention of the laser provided access to optical fields with large intensity that could be used to manipulate mechanical objects. Using the radiation pressure of a laser, Ashkin worked on trapping levitated dielectric particles. The spheres could be controlled in motion and temperature using optical feedback cooling [10, 11].

The start of cavity optomechanical experiments can be seen as the work by Braginskiĭ, who built a microwave Fabry–Pérot interferometer to measure the dynamical properties of a suspended mirror. He predicted and demonstrated the retardation of the radiation pressure force on the mirror due to the finite cavity lifetime, leading to damping and driving of the motion of the mirror. Originally called the ponderomotive action, this was the first demonstration of dynamical backaction [12, 13].

Here we see the parametric interaction that set off the field of cavity optomechanics and that is the foundation of the work presented in this thesis. The essence of this effect is as follows. The optical mode inside a Fabry-Pérot cavity has a resonance frequency defined by the length of the system. The light field inside the cavity influences the motion of the movable mirror at the end of the cavity. This motion, in turn, changes the cavity length and thereby induces a frequency shift, which changes the intensity of the intracavity field. Naturally, however, there are limits on the reachable accuracy of position measurements on the mechanical component. Braginskiĭ also already discussed the quantum fluctuations of the radiation pressure. This theory was later developed to the standard quantum limit (SQL) [14–16]. In the following years there was a growing interest in the theoretical possibilities of such coupled systems. Experimentally, much progress was made utilizing the radiation pressure force for detection and manipulation of mechanical resonators.

1.2. Modern Cavity Optomechanics

To overcome the experimental limitations scientists reached out to new platforms. The technological advances in the field of nanofabrication enabled the development

of a large variety of cavity optomechanical systems. Maybe most astonishing is the difference in scale of these experiments, with mechanical resonators of a mass from zg to kg, and cavities ranging from nm to km in size [17–20]. Some examples of these optomechanical systems and their respective accomplishments are discussed here. Microtoroid resonators and photonic crystals, in which an optical and mechanical mode can physically overlap, have been used for radiation pressure cooling and generation of self-oscillations [19, 21–24]. Similar cooling has been demonstrated in micromirrors at the end, and membranes and nanorods in the middle of a Fabry-Pérot cavity [25–28]. Furthermore, whispering gallery microdisks [29–31], microspheres [32] and even cold atoms [18, 33] have been used as the mechanical element. Moreover, optomechanical systems have been established using Brillouin scattering [34]. Finally, the largest optomechanical experiments in size have been used in the observation of gravitational waves [20, 35].

At the same time three-dimensional and thin-film microwave cavities were being integrated into electromechanical systems. Especially the ability to fabricate superconducting resonant circuits with a mechanical compliant element has proven to be successful. Typically in this case, a vibrating capacitance modulates the cavity frequency, giving rise to the same parametric interaction. Bringing the optical mode from the THz to GHz regime also significantly simplifies reaching the sideband-resolved regime for heavier mechanical resonators with lower eigenfrequencies. This allows, among other things, for sideband cooling of the mechanical mode to the ground state [36, 37]. Furthermore, superconducting circuits are compatible with circuit quantum electrodynamics (cQED) in relation to their cryogenic temperature, frequency range and fabrication techniques [38, 39], which facilitates the regime of cavity quantum optomechanics.

Also in microwave optomechanics, or electromechanics, there exists a large collection of systems, each with their own advantages. This coupling was first realized with the fabrication of a nanomechanical beam in a transmission line resonator [40]. The first phonon occupation of a mesoscopic mechanical oscillator was measured in a film bulk acoustic resonator (FBAR) [41]. Other experiments include quantum acoustics in a high-overtone bulk acoustic wave resonator (HBAR) [42] and displacement detection of a suspended nanowire below the standard quantum limit [43]. Furthermore, suspended microdrums were used to access the strong coupling regime [44] and the mechanical ground state using sideband cooling [36]. Moreover, these systems have been used for generation of non-classical states of motion by squeezing [45, 46] and for entanglement between two mechanical resonators [47]. Other incorporated mechanical resonators include high-stress silicon nitride membranes [48] and graphene membranes [49, 50]. Lastly, membranes have been used for microwave to optical photon transduction, which is a promising technique to be included in systems for quantum computation [51].

1

1.3. Motivation for Flip-Chip Optomechanics

Naturally, despite all these major achievements, there are still open challenges. The largest of which being the problem of how quantum mechanics describing these experiments is incompatible with the theory of general relativity. To test this experimentally, a system needs to access a parameter regime in which both effects significantly take place [52–54]. To reach this goal, there are generally two opposite approaches. One could start with a gravitational experiment and reduce the size in order to be able to create quantum mechanical states in the masses [55–58]. Alternatively, starting with a mechanical element in a quantum state, one could increase the mass of the resonator [59, 60]. With masses that vary over twenty orders of magnitude, cavity optomechanics is a natural platform to take on this challenge [61–63].

One of the mechanical resonators that could access both regimes is the high-stress silicon nitride membrane, as its resonance mode can have a large effective mass while retaining a considerable zero-point fluctuation. Furthermore, its frequency can be large enough to be in the sideband-resolved regime, a necessary condition for ground state cooling. Coupling the membrane to a superconducting microwave cavity can be achieved with the flip-chip technique [48, 51, 57, 64–75]. In this work, we present an increased coupling in a mechanically clamped flip-chip device.

However, cavity frequency noise can be a limiting factor in optomechanical experiments [76, 77]. Therefore, in this thesis we developed a dynamic feedback system that can lock multiple tones to an unstable microwave cavity. As any source of low-frequency cavity noise can be reduced, this feedback method has applications in various fields, such as reducing two-level system (TLS) noise [78], locking to coplanar waveguide resonators [79], SQUID cavities [80], gravitational wave detectors [81], axion dark-matter detectors [82], and magnomechanical experiments [83–86].

Another requirement for the preparation of massive superposition states is the integration of a nonlinearity in the system. Coupling the cavity to a qubit has been proposed to prepare mechanical quantum states [87–91], as well as coupling a qubit to the mechanics directly [75]. However, these methods require strong sideband drives to first cool the mechanical resonator to its ground state, which is incompatible with the limited critical photon number in Kerr cavities [36]. Nevertheless, theoretical proposals and experimental realizations have shown advantages of nonlinear optomechanical cavities. This has been used to create flux-mediated optomechanical systems [92–96], cool a mechanical mode to the ground state [97], enhance sideband cooling in the bad-cavity limit [98–102], create classical bimodal states of mechanical motion [103], and for remote sensing of a levitated mechanical resonator [104]. In this work we present a flux-tunable nonlinearity in an optomechanical flip-chip device. The cavity is stabilized via Kerr locking to a microwave tone and amplification of the intracavity field is observed, demonstrating a promising platform for nonlinear optomechanical experiments. Moreover, nonlinear optomechanical cavities have been predicted to exhibit an increased single

photon coupling rate [105] and quantum-limited amplification [106].

Furthermore, in recent work a superconducting qubit was longitudinally coupled to a linear resonator analogous to the radiation-pressure interaction in optomechanical systems [107]. Integration of a similar coupling in our flip-chip device would allow for a dynamical modulation of the coupling between the cavity and the qubit. The large critical photon number would enable strong drives in the linear circuit to cool the mechanical resonator. This combined system has been proposed to prepare Schrödinger cat states in the linear resonator, which could be swapped into the mechanical mode via a beam-splitter interaction pulse [88, 107, 108]. This would provide a promising platform to generate and control massive, macroscopic superpositions to test gravitational decoherence [61–63].

1.4. Thesis Structure

In this chapter we presented an introduction to the field of optomechanics as well as an outlook of prospective research directions. In **Chapter 2** we provide the necessary theoretical foundation for understanding the underlying physics of the experimentally studied systems in this thesis. The mechanical and electromagnetic harmonic oscillator are treated, in both the classical as the quantum mechanical interpretation. We take a close look at the vibrational mode of a high-stress membrane, its energy dissipation mechanisms and how to mitigate these. Subsequently, we discuss the parametric coupling of these two systems, leading to the optomechanical interaction. In **Chapter 3** we describe the design, simulation and nanofabrication techniques of the nonlinear flip-chip device. We focus separately on the microwave and membrane chips, and the assembly of the flip-chip device. We conclude with a discussion on the cryogenic measurement setup. The next **Chapter 4** introduces the experimental challenge of cavity noise. We demonstrate a dynamic feedback system implemented by the locking of a microwave drive to the cavity, removing low-frequency noise. This scheme is then scaled to enable multitone experiments locked to the same feedback signal, where we observe optomechanically induced transparency. In **Chapter 5** we measure the large quality factor of the membrane and perform multitone sideband cooling of the mechanical mode. Furthermore, we highlight the subtleties and assumptions necessary for the calibration of the mechanical mode temperature and discuss a general calibration procedure. In **Chapter 6** we present a flux-tunable nonlinearity in an optomechanical flip-chip device. We characterize the dispersive coupling between the cavity and a superconducting qubit. The nonlinear cavity is stabilized by Kerr locking to a microwave tone, where signal and idler modes are created in which we observe amplification of the intracavity field. Finally, in **Chapter 7**, we conclude the work performed in this thesis and discuss the main findings, as well as an outlook for further research in the field of nonlinear optomechanics. All data, measurement scripts and analysis scripts can be found in the following DOI: 10.5281/zenodo.15689953

2

Theory and Background

In this chapter we will provide the necessary theoretical foundation for understanding the underlying physics of the experimentally studied systems in the following chapters. We start from the classical description of a mechanical resonator as a harmonic oscillator, which we will then relate to the quantum mechanical description. The mode shapes of a rectangular membrane and its effective mass are discussed, as well as its energy loss mechanisms and the dissipation dilution countering these. Secondly, we will follow a similar treatment for an electromagnetic resonator. Finally, we will consider the parametric coupling of these resonators to form an optomechanical system.

The experiments presented in this work are built upon a variety of theoretical foundations. In this chapter we will discuss the bases of two different systems: the mechanical harmonic oscillator and the electromagnetic harmonic oscillator. The parametric coupling of these systems to each other forms the core of the devices treated in this thesis.

2

2.1. Mechanical Harmonic Oscillators

Vibrating mechanical resonators are among the most well-known physical systems in nature, and are one of the main components of optomechanical experiments. Specifically, in the flip-chip devices fabricated during this work, the mechanical motion of thin high-tensile stress membranes is detected and controlled. The harmonic approximation of these oscillators is especially useful and will be treated in this section, as well as properties of the vibrational modes and the alleviation of their energy dissipation mechanisms.

2.1.1. Classical Harmonic Motion

We start with a simple model of a mass on a spring, as illustrated in Figure 2.1**a**. When the system is out of equilibrium, the equation for the restoring force is given by

$$F = -kx \tag{2.1}$$

where k is the spring constant of the system, and x its position relative to its rest position. Using Newton's second law of motion $F = m\ddot{x}$, where m is the mass of the system, we can write a second order differential equation

$$\ddot{x} + \frac{k}{m}x = 0 \tag{2.2}$$

Solving this equation, we obtain the time-dependent solution

$$x(t) = A \cdot \cos(\Omega_m t + \phi) \tag{2.3}$$

where A is the amplitude of the motion and ϕ its phase. The system's resonance frequency is given by $\Omega_m = \sqrt{\frac{k}{m}}$. However, any physical system will always suffer from energy dissipation, originating from one or multiple loss mechanisms. This effect can be included by adding a loss term Γ_m. Moreover, detection or control over the resonator in an experiment will produce a driving force $F_{drive}(\Omega) = \frac{F_0}{m} \cdot e^{-i\Omega t}$ at a frequency Ω. The differential equation can now be written as

$$\ddot{x} + \Gamma_m \dot{x} + \Omega_m^2 x = \frac{F_{drive}}{m} \tag{2.4}$$

Converting the solution of this equation to the frequency domain, we obtain

$$x(\Omega) = \frac{F_0}{m\left(\Omega_m^2 - \Omega^2 - i\Omega\Gamma_m\right)} = \chi_m F_0 \tag{2.5}$$

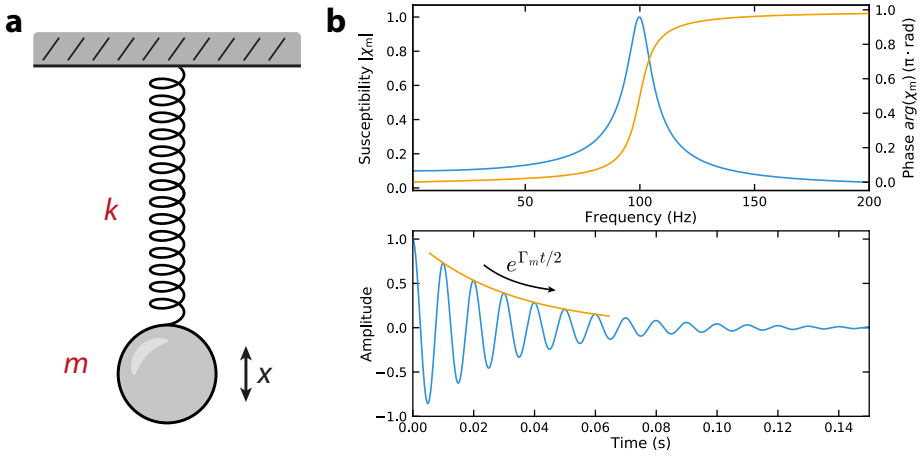


Figure 2.1: A mechanical harmonic oscillator and its response. **a** Schematic of a mass-spring system with mass m and spring constant k representing a mechanical harmonic oscillator. An external excitation can cause a deflection x from its equilibrium position. **b** Magnitude (blue) and phase (orange) of the normalized absolute mechanical susceptibility of a system with a resonance frequency $\Omega_m = 2\pi \cdot 100$ Hz and linewidth $\Gamma_m = 2\pi \cdot 10$ Hz. Panel **c** shows the decaying amplitude of the resonator over time.

with the mechanical susceptibility

$$\chi_m(\Omega) = \frac{1}{m\left(\Omega_m^2 - \Omega^2 - i\Omega\Gamma_m\right)} \tag{2.6}$$

This describes the response of the mechanical displacement to an exerted force at frequency Ω. The magnitude (blue) and phase (orange) of the frequency response function of a resonator are shown in Figure 2.1**b**. Starting from an initial excitation, or deflection of the mass, in Figure **c** the system's decay over time is shown. The damped motion follows the envelope $e^{-\Gamma_m t/2}$.

An intuitive quantity to introduce here is the quality factor, or Q-factor. This dimensionless parameter can be used to describe the resonant properties of any resonator. Historically, there are two different definitions of the quality factor [109]. However, these two definitions become equivalent in the limit of underdamped resonators, where $Q \gg 1$. The first, intuitive, definition is the ratio of the energy stored in the oscillation to the energy dissipation per cycle

$$Q = 2\pi \cdot \frac{\text{energy stored}}{\text{energy dissipated per cycle}} \tag{2.7}$$

The second definition is more useful for systems with high frequencies and is given by the ratio between the resonance frequency to its linewidth. For the mechanical

resonator this can be written as

$$Q_m = \frac{\Omega_m}{\Gamma_m} \tag{2.8}$$

A larger quality factor means slower energy dissipation and thus a resonator that rings down over an extended period of time. In optomechanical experiments one typically aims for high-Q mechanical resonators.

2.1.2. Mechanical Harmonic Oscillator Quantization

The classical Hamiltonian, which describes the total energy of the system, of a mechanical harmonic oscillator can be written in terms of its momentum p and position x

$$\mathcal{H} = \frac{p^2}{2m} + \frac{1}{2} m\Omega_m^2 x^2 \tag{2.9}$$

In the experiments performed in this thesis, the mechanical resonators are operated at low temperatures and will therefore contain a low amount of energy. In this case, it is especially useful to quantize the motion of the mechanical oscillators, describing its energy as discrete phonons. As first described by Dirac [110], we begin by using the quantum operators

$$\hat{x} = x \quad \text{and} \quad \hat{\mathrm{p}} = \mathrm{p} \tag{2.10}$$

With this, we can write the Hamiltonian as

$$\hat{\mathcal{H}} = \frac{\hat{p}^2}{2m} + \frac{1}{2} m\Omega_m^2 \hat{x}^2 \tag{2.11}$$

We will now introduce the phonon creation and annihilation operators $\hat{b}^\dagger$ and $\hat{b}$ in terms of $\hat{x}$ and $\hat{p}$. These ladder operators act by adding and removing one quantum of energy to the oscillator.

$$\hat{b}^\dagger = \sqrt{\frac{m\Omega_m}{2\hbar}} \cdot \left(\hat{x} - \frac{i\hat{p}}{m\Omega_m} \right) \tag{2.12}$$

$$\hat{b} = \sqrt{\frac{m\Omega_m}{2\hbar}} \cdot \left(\hat{x} + \frac{i\hat{p}}{m\Omega_m} \right) \tag{2.13}$$

These operators obey the commutation relation $[\hat{b}, \hat{b}^\dagger] = 1$, as the phonon excitation can be described as a boson quasiparticle. The quantized Hamiltonian can now be written as

$$\hat{\mathcal{H}} = \hbar\Omega_m \cdot \left(\hat{b}^\dagger \hat{b} + \frac{1}{2} \right) \tag{2.14}$$

This is an intuitive way to write the Hamiltonian in terms of the number operator $\hat{n}_m = \hat{b}^\dagger \hat{b}$. The total energy of the mechanical resonator based on its average phonon occupation $\bar{n}_m = \langle \hat{b}^\dagger \hat{b} \rangle$ can be found by

$$E = \hbar\Omega_m \cdot \left(\bar{n}_m + \frac{1}{2}\right) \tag{2.15}$$

The system's energy levels are discrete and are split by an energy of $\hbar\Omega_m$. The harmonic energy potential is shown in Figure 2.2, together with the probability density of the wave function $|\psi(x)|^2$ for the ground state and the first three excitations. Inversely, in order to regain a more intuitive picture, we can write the quantum operators for position and momentum in terms of the ladder operators.

$$\hat{x} = x_{zpf} \cdot \left(\hat{b}^\dagger + \hat{b}\right) \tag{2.16}$$

$$\hat{p} = i p_{zpf} \cdot \left(\hat{b}^\dagger - \hat{b}\right) \tag{2.17}$$

where $x_{zpf} = \sqrt{\frac{\hbar}{2m\Omega_m}}$ is the zero-point fluctuation of the position of the mechanical oscillator. $p_{zpf} = \sqrt{\frac{\hbar m\Omega_m}{2}}$ is that of its momentum. These quantities are the uncertainty that is obtained when measuring respectively the position or momentum of the oscillator in the ground state. It is noteworthy to look at the commutation relation $[\hat{x}, \hat{p}] = i\hbar$. Therefore, the Heisenberg uncertainty limit is given by $x_{zpf}p_{zpf} = \frac{1}{2}\hbar$, which sets a fundamental limit on the measurement sensitivity.

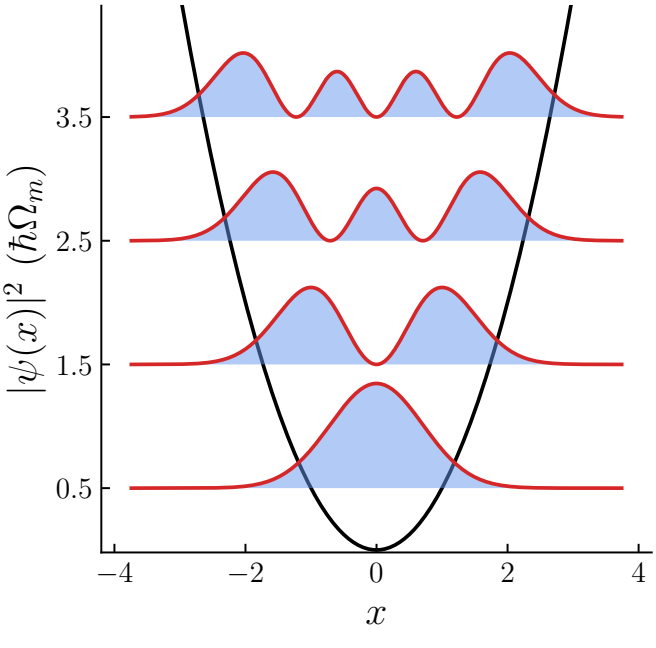


Figure 2.2: Energy potential and phononic states of the harmonic oscillator. The probability density of the phononic wave function $|\psi(x)|^2$ is plotted for the ground state $\left(\frac{1}{2}\hbar\Omega_m\right)$. The first three excited states are shown with an energy spacing of $\hbar\Omega_m$.

The zero-point energy, when the resonator is in its ground state, is thus given by $\frac{1}{2}\hbar\Omega_m$. However, the average phonon occupation due to the resonator's thermal energy is given by the Bose-Einstein relation

$$\bar{n}_m = \frac{1}{e^{\frac{\hbar\Omega_m}{k_B T}} - 1} \approx \frac{k_B T}{\hbar\Omega_m} \tag{2.18}$$

where k_B is the Boltzmann constant and T the mode temperature. The approximation is true for $k_B T \gg \hbar\Omega_m$, which is generally true for the MHz mechanical resonators at mK temperatures used in this work.

Returning to the mechanical linewidth Γ_m introduced in the previous section, quantum mechanically, this quantity can be seen as the rate at which a single phonon dissipates from the resonator. Therefore, we can define the mechanical coherence time as

$$t_{coh} = \frac{1}{\bar{n}_m \Gamma_m} \tag{2.19}$$

2.1.3. Mode Shapes and Effective Mass

Going forward from our simple one-dimensional model of a mass on a spring, we will now look at the motion of a two-dimensional membrane. In this work, we have used thin, high-stress silicon nitride (Si_3N_4) membranes. The equation of motion for a rectangular membrane is

$$\frac{\partial^2 z}{\partial x^2} + \frac{\partial^2 z}{\partial y^2} - \frac{\rho_r}{\sigma}\frac{\partial^2 z}{\partial t^2} = 0 \tag{2.20}$$

where the membrane is clamped in the xy-plane [111]. Here, ρ_r is the density of the resonator's material, and σ its tensile stress. The membrane will have an infinite number of modes (u, v) in the x- and y-direction. In the real device, the membrane will be fixated at the edges. This equation of motion is solved in Ref. [112], which results in eigenmodes with mode shapes $\psi_{u,v}$ and frequencies $f_{u,v}$ of a square membrane of size L.

$$\psi_{u,v}(x, y) = \sin\left(\frac{u\pi x}{L}\right)\sin\left(\frac{v\pi y}{L}\right) \tag{2.21}$$

$$f_{u,v} = \frac{\omega_{u,v}}{2\pi} = \sqrt{\frac{\sigma}{4\rho_r L^2}(u^2 + v^2)} \tag{2.22}$$

The membranes used in our experiments have a density $\rho_r \approx 3180\,\mathrm{kg/m^3}$ and stress $\sigma = 0.95$ GPa. The lateral size is $L = 300\,\mu\mathrm{m}$, resulting in a fundamental frequency around $f_{1,1} \approx 1$ MHz. Additionally, the fundamental and higher order modes are calculated using finite-element simulations using *COMSOL Multiphysics* [113] and are shown in Figure 2.3.

However, since a membrane displacement has a non-uniform spatial distribution, the way we define the amplitude of the mode is not trivial. In order to calibrate the

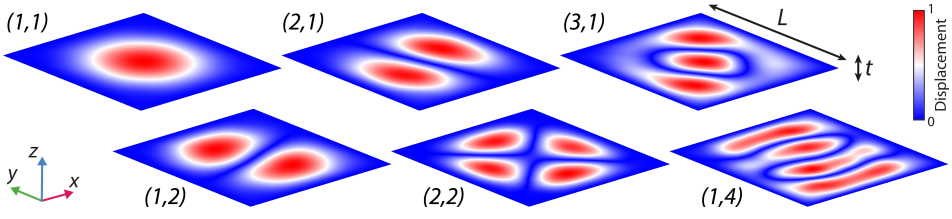


Figure 2.3: Simulated mode shapes of a square membrane. The normalized displacement of the fundamental mode $(1,1)$, which is the dominant mode coupling to the microwave cavity, is shown. Moreover, five higher modes are plotted, each labeled with its mode index (u,v).

motion of the device, the amplitude we use must obey the equipartition theorem. In literature there are many methods to fulfill this condition, e.g. see Ref. [114–121]. In this work, we define the amplitude as the physical displacement at the position and time of maximum deflection. We then apply a correction to the mass of the mode. The effective mass of our vibrational modes can be calculated with

$$m_{eff} = \frac{m}{L^2}\int_0^L\int_0^L |\psi_{u,v}(x,y)|^2\, dxdy = \frac{1}{4}m \tag{2.23}$$

Interestingly, this integral is constant, and thus independent of the mode, which is a property of rectangular membranes [112]. For the membranes uses in our devices we calculate an effective mass of $m_{eff} = 7.15$ ng. From this, we find a zero-point fluctuation of $x_{zpf} = 1.09$ fm and $p_{zpf} = 0.0487$ aNs. In the devices treated in this work we couple our microwave cavity to the fundamental vibrational mode of the membrane.

2.1.4. Mechanical Loss Mechanisms

There are many mechanisms that cause dissipation of energy from the membrane [122], the most prominent of which are treated here. We can distinguish energy transfer from the mechanical mode to other media, and energy dissipation in the material of the membrane itself.

Energy loss can occur when a mechanical resonator is located in a medium, such as a gas or a liquid. However, for silicon nitride membrane resonators with a frequency around 1 MHz viscous damping becomes negligible at pressures below 10^{-3} mbar [123, 124]. As all presented optomechanical experiments are performed at cryogenic temperatures, we can therefore ignore this source of energy dissipation, as the vacuum reached is on the order of 10^{-7} mbar [125].

Loss mechanisms that take place inside the silicon nitride can be grouped under the term internal friction. Any vibrating object will suffer a certain amount from thermoelastic damping [126, 127]. The vibrational mode shape of the membrane will result in temperature differences throughout the material. This results in an irreversible heat flow due to the periodical deformation of the material, in-

creasing the entropy of the system, and thereby causing energy to dissipate. At mK temperatures, however, thermoelastic damping becomes negligibly small [124].

One of the main energy dissipation mechanisms in our system is bending loss. For the fundamental mode, the largest contribution of bending losses will be at the clamping points around the edges, as this is where the curvature is largest [124, 128–131]. However, by increasing the tensile stress of the membrane, as well as designing soft clamping points, this source of friction can be reduced.

The mechanical resonator can also lose energy to its surrounding. This can be inside the silicon substrate or to the sample holder, and can be caused by acoustic radiation losses (also called clamping losses) [130–132]. Acoustic loss comes from elastic energy transfer, where vibrational energy is radiated into the substrate. A specific example of clamping losses is called phonon tunneling, which nanomechanical resonators are known to suffer from [133–138]. There will be more acoustic loss if the membrane mode overlaps with the substrate modes [128, 139–141]. This source of energy dissipation can be reduced by increasing the acoustic impedance mismatch between the membrane mode and the substrate modes [124, 142]. Analytical models have been developed on how membrane modes couple to a semi-infinite substrate [133, 141]. However, it is clear that this is highly dependent on how the resonator (in our case the membrane chip) is attached to its sample holder. A common method to attach silicon chips is by using glue [57, 64–74, 128, 143–145]. However, glue is known to have high mechanical losses due to a large nonlinear response. Therefore, in this work devices were fabricated in which the membrane chip is mechanically clamped without the use of glue. More details on the device assembly are discussed in Chapter 3.

Every loss mechanism adds another channel for the membrane to lose energy, increasing its linewidth and decreasing its coherence time. The total loss is the sum of these factors, resulting in a total mechanical quality factor that can be written as

$$\frac{1}{Q_m} = \frac{1}{Q_{viscous}} + \frac{1}{Q_{thermoelastic}} + \frac{1}{Q_{bending}} + \frac{1}{Q_{clamping}} + \cdots \tag{2.24}$$

An extremely successful method to reduce clamping losses and phonon tunneling is the implementation of mechanical dissipation dilution.

2.1.5. Mechanical Dissipation Dilution and Phononic Shield Isolation

In this subsection we zoom in on the clamping losses of the membrane, as this is typically the dominant contribution in our experiments. Especially, we focus on the reduction of energy loss at the membrane's anchor points. The quality factor due to clamping losses for a square membrane is given by

$$Q_{clamping} \approx \frac{3u^2v^2}{2(u^2+v^2)^{3/2}} \frac{L}{d} \sqrt{\frac{\rho_r}{\rho_s}} \left(\frac{E_s}{\sigma}\right)^{3/2} \tag{2.25}$$

with the mass densities ρ_s and ρ_r of the substrate and resonator, the substrates Young's modulus E_s, the membrane's tensile stress σ [124, 141]. The length and thickness of the membrane are defined by L and d respectively. The quality factor can evidently be increased by maximizing the length to thickness ratio (3000 for our devices).

Clamping and bending losses can be alleviated with the implementation of dissipation dilution, first formulated in the field of gravitational-wave interferometers [146]. The first observation of this effect, however, was during the study on the stress of silicon and polymer membranes [147, 148]. Particularly useful for micromechanical membranes is the use of an acoustic crystal [128, 149].

Such a phononic shield can either be made by removing material of the substrate or resonator periodically, or by corrugating the material [150]. One can place an existing mechanical resonator into a two-dimensional structure, designed to have a bandgap around the resonator frequency. Another method is to introduce a defect in the periodic structure to localize the vibrational waves. When the defect mode falls within the bandgap, the energy dissipation is greatly reduced [151]. One specific feature of dissipation dilution with an in-membrane phononic shield is that the resonator can be softly clamped. The advantage of soft clamping a membrane is twofold. First, the resonator mode is isolated from its surrounding, thereby creating less energy dissipation into the substrate. Second, the resonator mode shape decays more fluently intro the substrate, creating softer bending at the clamping points [132, 152–157]. Details on the design of the acoustic crystal used in this work is presented in Chapter 3.

2.2. Electromagnetic Harmonic Oscillators

This section will introduce the theoretical background for electromagnetic harmonic oscillators. We will discuss both the classical and quantized Hamiltonian of the circuits used in our devices, after which we zoom in on microwave frequency resonators and their loss mechanisms.

2.2.1. Simple Electromagnetic Harmonic Oscillator

The second half of our optomechanical system consists of an electromagnetic resonator. Similar as with the mechanical resonator, this can be represented with a simple harmonical oscillator model. Our resonators are thin film superconducting electrical circuits, that are build up from components such as capacitors and inductors. We will treat these as lumped elements, as shown in Figure 2.4.

We begin with a simple electrical circuit consisting of a capacitor and an inductor,

which we will call the LC-circuit. The voltage (V) and current ($I = \frac{dq}{dt}$, with q the charge) follow the relations

$$V = L \cdot \frac{dI}{dt} \tag{2.26}$$

$$I = -C \cdot \frac{dV}{dt} \tag{2.27}$$

where L is the inductance and C the capacitance of the circuit. With this we can write the second order differential equation

$$\ddot{V} + \frac{1}{LC} V = 0 \tag{2.28}$$

We can solve this equation to get the time-dependent solution

$$V(t) = A \cdot \cos(\omega_c t + \phi) \tag{2.29}$$

where A is the voltage amplitude and ϕ its phase. The circuit's resonance frequency is given by $\omega_c = \frac{1}{\sqrt{LC}}$. Note here the similarity with the solution for the mechanical harmonic oscillator in Equation 2.3. Similarly, in the case of the electromagnetic resonator there will be important loss mechanisms and drives. These will be introduced in Section 2.2.4.

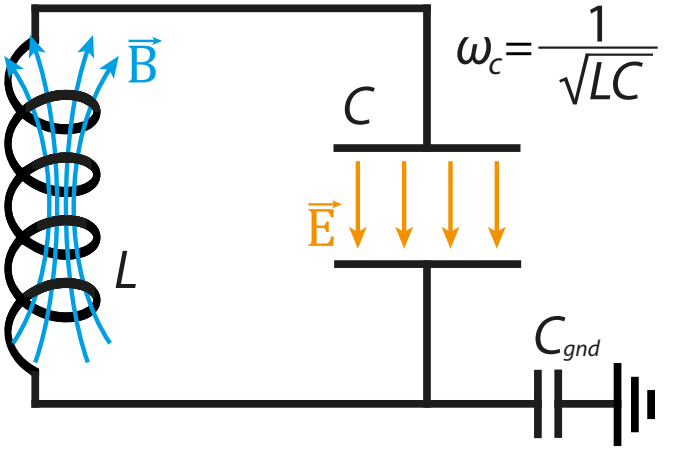


Figure 2.4: Schematic diagram of an LC-resonator. The basis for the circuits used in the experiments. The energy is alternately stored in the magnetic field $\vec{B}$, created by the current flowing through the inductor L, and in the electric field $\vec{E}$, caused by the voltage over the capacitor pads C. These elements define the circuit's resonance frequency ω_c.

2.2.2. Circuit Quantization

The classical Hamiltonian of this circuit can be written as

$$\mathcal{H} = \frac{1}{2}LI^2 + \frac{1}{2}L\omega_c^2 q^2 \tag{2.30}$$

Using Faraday's law to describe the magnetic flux through the inductor $\Phi = LI$, we can rewrite the Hamiltonian as

$$\mathcal{H} = \frac{\Phi^2}{2L} + \frac{q^2}{2C} \tag{2.31}$$

We see that the total energy description of the electromagnetic resonator is analogous to that of the mechanical harmonic oscillator. Again, we will quantize the Hamiltonian using quantum operators

$$\hat{\Phi} = \Phi \quad \text{and} \quad \hat{\mathrm{q}} = \mathrm{q} \tag{2.32}$$

$$\hat{\mathcal{H}} = \frac{\hat{\Phi}^2}{2L} + \frac{\hat{q}^2}{2C} \tag{2.33}$$

We can now introduce the photon creation and annihilation operators $\hat{a}^\dagger$ and $\hat{a}$ in terms of $\hat{\Phi}$ and $\hat{q}$. These ladder operators act by adding and removing one quantum of energy to the oscillator.

$$\hat{a}^\dagger = \frac{1}{\sqrt{\hbar\omega_c}} \cdot \left(\frac{\hat{\Phi}}{\sqrt{2L}} + i\frac{\hat{q}}{\sqrt{2C}} \right) \tag{2.34}$$

$$\hat{a} = \frac{1}{\sqrt{\hbar\omega_c}} \cdot \left(\frac{\hat{\Phi}}{\sqrt{2L}} - i\frac{\hat{q}}{\sqrt{2C}} \right) \tag{2.35}$$

These operators obey the commutation relation $[\hat{a}, \hat{a}^\dagger] = 1$. Therefore, the discrete excitation, or photon, in the circuit can be described as a boson. The Hamiltonian can now be written as

$$\hat{\mathcal{H}} = \hbar\omega_c \cdot \left(\hat{a}^\dagger\hat{a} + \frac{1}{2} \right) \tag{2.36}$$

This is an intuitive way to write the Hamiltonian in terms of the number operator $\hat{n}_c = \hat{a}^\dagger\hat{a}$. Now we can write the total energy of the LC-resonator based on the average number of photons $\bar{n}_c = \langle \hat{a}^\dagger\hat{a} \rangle$ it contains

$$E = \hbar\omega_c \cdot \left(\bar{n}_c + \frac{1}{2} \right) \tag{2.37}$$

The ground state of the LC-resonator has an energy of $\frac{1}{2}\hbar\omega_c$, and each energy level is split by $\hbar\omega_c$. We can express the zero-point fluctuation of the magnetic flux and charge as $\Phi_{zpf} = \sqrt{\frac{\hbar}{2C\omega_c}}$ and $q_{zpf} = \sqrt{\frac{\hbar C\omega_c}{2}}$. Following the Bose-Einstein relation stated in Equation 2.18, the GHz resonators used in this work will be in their ground state at mK temperatures.

2.2.3. Microwave Resonators

In this subsection we will take a closer look at a specific group of LC-resonators: the microwave cavity. Two-dimensional superconducting films are convenient to design meander inductor lines and capacitors with values that can produce microwave resonators. A common geometry is the coplanar waveguide (CPW), a central superconducting line enclosed on both sides by a ground plane at a fixed distance. The length of the line changes both the inductance and the capacitance of the waveguide [158]. This results in standing-wave excitations with known eigenfrequencies.

There are two common geometries for CPWs. The first is where one of the ends of the line is connected to ground, called a $\lambda/4$ resonator. The second is where both ends of the line are shorted, and is called a $\lambda/2$ resonator. At the location where the line is shorted it will share the 0 voltage of the ground plane, creating a node in the electric field. Moreover, at this location the amplitude of the flowing current will be maximum. This, thereby, creates an anti-node in the magnetic field. Contrary, at an open end of the line the opposite will take place. The terminations and the total length of the line therefore determine the eigenfrequencies of the resonator [159].

Another possible microwave cavity geometry to use is a lumped resonator, where every element is considered to contribute localized properties to the circuit. Every component can be approximated to only contribute either to the capacitance or to the inductance of the total circuit. As we aim to couple a superconducting LC-resonator capacitively to a metallized membrane in a flip-chip geometry, we want to focus the electric field between these two systems. It is therefore advantageous to localize the capacitance of the circuit in order to maximize the coupling to the membrane. The design of the microwave cavities used in the devices for thesis is described in Chapter 3.

2.2.4. Microwave Loss Channels

Another use of the CPW is as a feedline to transmit in- and output signals over the chip. For this, we design the line's width and its gaps to ground such, as to result in an impedance of $50\,\Omega$ at GHz frequencies. The CPW performs as a perfect transmission line, or waveguide, and is the connection between the cavity and the measurement setup.

A microwave resonator can either be coupled capacitively or inductively to a feedline. In this work we will use both a reflection and transmission geometry. Importantly, when using a reflection line, one has to take the amplitude of the electric or magnetic field into account with respect to the distance to the end of the feedline. Therefore, a higher drive power might be required to produce the same photon occupation in a coupled resonator. However, a disadvantage of a transmission line is that only half of the signal will be delivered at the device output.

Coupling the resonator to the feedline introduces an extra dissipation channel where the resonator loses energy. This coupling rate we call κ_{ex}. Furthermore, any physical resonator will also have internal decay mechanisms, where energy is transmitted to the environment, which are captured together into κ_{in}. Typically, the dominant internal loss mechanism for thin film superconducting resonators is the dielectric loss tangent of the substrate. For silicon, the substrate material used in this work, a few nanometer thin layer of silicon dioxide grows on the surface within seconds when exposed to air [160]. Energy is dissipated due to polarization of the electric dipoles and excitation of two-level systems (TLS) in the dielectric material [161]. The total linewidth of the cavity is given by $\kappa_{tot} = \kappa_{in} + \kappa_{ex}$. The quality factor of the microwave cavity is given by

$$Q_c = \frac{\omega_c}{\kappa_{tot}} = \frac{\omega_c}{\kappa_i + \kappa_e} \tag{2.38}$$

This feedline is also used to drive the resonator by sending a microwave signal with frequency ω_d. We can write the equation of motion of the intracavity field, including the loss channels and the input field $\hat{a}_{in}$ as

$$\dot{\hat{a}} = \left(i\Delta - \frac{1}{2}\kappa_{tot}\right)\hat{a} + \sqrt{\kappa_{ex}}\hat{a}_{in} \tag{2.39}$$

where $\Delta = \omega_d - \omega_c$. Solving this equation for a steady-state solution gives

$$\langle\hat{a}\rangle = \frac{\sqrt{\kappa_{ex}}\langle\hat{a}_{in}\rangle}{\frac{1}{2}\kappa_{tot} - i\Delta} \tag{2.40}$$

Using the number operator, we find the cavity's steady-state photon occupation dependent on the microwave power $P = \hbar\omega_d \left|\langle\hat{a}_{in}\rangle\right|^2$ at the input of the cavity

$$\bar{n}_c = \left(\frac{\kappa_{ex}}{\left(\frac{1}{2}\kappa_{tot}\right)^2 + \Delta^2}\right)\frac{P}{\hbar\omega_d} \tag{2.41}$$

In experiments we typically perform measurements on the reflection coefficient S_{21} of the resonator, which relates the measured output signal to the input signal. For a cavity coupled to a transmission feedline this is [162, 163]

$$S_{21}(\omega) = \frac{\kappa_{ex}}{\frac{1}{2}\kappa_{tot} - i(\omega - \omega_c)} = \kappa_{ex}\chi_c \tag{2.42}$$

with the electromagnetic susceptibility

$$\chi_c(\omega) = \frac{1}{\frac{1}{2}\kappa_{tot} - i(\omega - \omega_c)} \tag{2.43}$$

2.3. Optomechanical Coupling

Now that we have seen the quantization of both the mechanical and the electromagnetic harmonic oscillator, we can couple these two systems. For the flip-chip devices used in this work the mechanical resonator is capacitively coupled to the

bare superconducting cavity. When the metallized membrane moves, the capacitance of the cavity changes, and thereby also its resonance frequency. This parametric interaction is the core of our devices. An optical analogue would be, for example, a Fabry-Pérot cavity with one oscillating mirror, dispersively coupling the light field to the mirror's motion. A schematic diagram of an optomechanical device coupled to a feedline, where each system is thermalized to its respective bath, is shown in Figure 2.5. The position dependent cavity resonance frequency can be Taylor-expanded as

$$\omega_c(x) \approx \omega_c + x \cdot \frac{\partial \omega_c}{\partial x} + \dots \tag{2.44}$$

When we fill this expression into the combined Hamiltonian we obtain

$$\hat{\mathcal{H}}/\hbar = \omega_c \hat{a}^\dagger \hat{a} + \Omega_m \hat{b}^\dagger \hat{b} - g_0 \hat{a}^\dagger \hat{a} \left(\hat{b} + \hat{b}^\dagger\right) + \dots \tag{2.45}$$

where we made use of the optomechanical single photon coupling rate $g_0 = G x_{zpf}$, dependent on the frequency pull factor $G = \frac{\partial \omega_c}{\partial x}$ [164]. The coupling g_0 is the frequency shift of the microwave cavity resonance due to the vacuum fluctuations of the coupled mechanical resonator. Using Equation 2.16, we find the radiation pressure force that the mechanical resonator experiences from the intracavity photons as the derivative of the Hamiltonian with respect to the displacement

$$\hat{F} = \frac{\partial \hat{\mathcal{H}}}{\partial \hat{x}} = \frac{\hbar g_0}{x_{zpf}} \bar{n}_c \tag{2.46}$$

Experimentally, the interaction can thus be increased by raising the cavity field with an external source. In superconducting cavities this can be done by sending a coherent drive tone ω_d (close) to the cavity. At this point, it is illustrative to transform to the rotating frame of the drive frequency, where we can write the linearly approximated Hamiltonian as

$$\hat{\mathcal{H}}/\hbar = -\Delta \hat{a}^\dagger \hat{a} + \Omega_m \hat{b}^\dagger \hat{b} - g_0 \hat{a}^\dagger \hat{a} \left(\hat{b} + \hat{b}^\dagger\right) \tag{2.47}$$

where again $\Delta = \omega_d - \omega_c$. Let us now consider the intracavity field as an average coherent amplitude with a fluctuating contribution $\hat{a} = \bar{\alpha} + \delta\hat{a}$. Then, the linearized optomechanical interaction Hamiltonian becomes

$$\begin{aligned} \hat{\mathcal{H}}_{int} &\approx -\hbar g_0 \cdot (\bar{\alpha} + \delta\hat{a})^\dagger (\bar{\alpha} + \delta\hat{a}) \left(\hat{b} + \hat{b}^\dagger\right) \\ &\approx -\hbar g_0 \cdot \left(\bar{n}_c + \sqrt{\bar{n}_c} \left(\delta\hat{a} + \delta\hat{a}^\dagger\right)\right) \left(\hat{b} + \hat{b}^\dagger\right) \end{aligned} \tag{2.48}$$

where we omitted the term containing $\delta\hat{a}^\dagger \delta\hat{a}$ for being small. In the second step we have made the assumption that the average field amplitude in the cavity is real $\bar{\alpha} = \sqrt{\bar{n}_c}$. Note that the first term in Equation 2.48 results in a constant radiation pressure force. This translates to a static displacement of the mechanical resonator and can thus be incorporated in the cavity frequency. What remains is

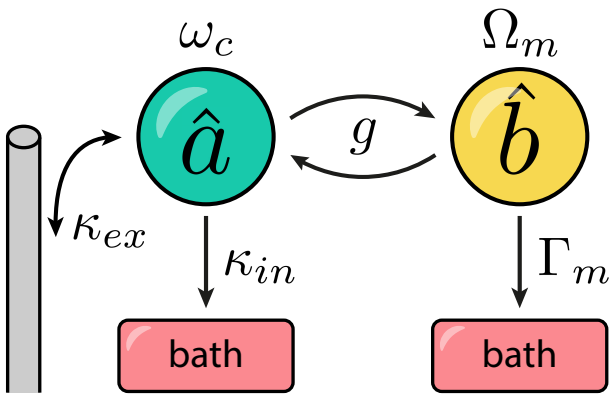


Figure 2.5: Schematic diagram of an optomechanical device coupled to a reflection feedline. Detailed information about the different couplings is provided in main text.

the term proportional to $\sqrt{\bar{n}_c}$. The interaction between the two systems is thus enhanced by the drive to the multi-photon coupling rate [165]

$$g = g_0\sqrt{\bar{n}_c} \tag{2.49}$$

The resulting linearized Hamiltonian in the rotating frame reads

$$\hat{\mathcal{H}}/\hbar = -\Delta\delta\hat{a}^\dagger\delta\hat{a} + \Omega_m\hat{b}^\dagger\hat{b} - g\left(\delta\hat{a} + \delta\hat{a}^\dagger\right)\left(\hat{b} + \hat{b}^\dagger\right) \tag{2.50}$$

If we now consider the sideband-resolved regime, where $\kappa_{tot} \ll \Omega_m$, we can enhance certain terms of this interaction while suppressing others by choosing an appropriate drive frequency [38]. Placing the drive tone red-detuned from the cavity by the mechanical frequency ($\Delta \approx -\Omega_m$) the interaction Hamiltonian becomes

$$\hat{\mathcal{H}}_{int}/\hbar \approx -g \cdot \left(\delta\hat{a}^\dagger\hat{b} + \delta\hat{a}\hat{b}^\dagger\right) \tag{2.51}$$

known as the beam-splitter interaction. Here, we have applied the rotating wave approximation (RWA) where we omit fast-rotating terms [163]. The photons from the drive induce a three-wave mixing process. The former term in Equation 2.51 creates one photon in the cavity while annihilating a phonon of the mechanical resonator. This process thus reduces the energy of the mechanical mode by transferring its energy into the cold microwave mode. The energy difference is accounted for by the drive photon. The latter term, however, does the opposite. It annihilates a cavity photon and creates of a phonon. Both these processes take place, creating sidebands around the drive tone. However, as only this upper sideband significantly overlaps with the cavity susceptibility, the former process is dominant and the mechanical mode is effectively cooled. This results in an increase of the mechanical linewidth as $\Gamma_{eff} = \Gamma_m + \Gamma_{OM}$. Note that by instead placing the drive blue-detuned from the cavity $\Delta \approx +\Omega_m$ the opposite process is conducted, and

the mechanical mode is parametrically amplified. This is known as the two-mode squeezing interaction and can drive the mechanical resonator into self-oscillations and the chaotic regime [166, 167]. Finally, if the drive is resonant with the cavity $\Delta \approx 0$, both processes happen symmetrically and one can observe a π phase shift of the cavity field. This technique can me used to improve the mechanical displacement detection.

The parametric coupling, however, goes both ways. The mechanical motion induces a frequency shift of the cavity and changes the intensity of the intracavity field. This, in turn, changes the radiation pressure force, which influences the mechanical motion. Besides the cavity frequency shift, there is thus also an additional mechanical damping rate Γ_{OM} due to the parametric coupling, which can either be positive or negative. This process is called dynamical backaction and will be discussed in detail in Chapter 5. The optimal case of largest damping is, as discussed above, in the case of a red sideband drive.

3

Design and Fabrication

This chapter presents the design and fabrication processes for the realization of the optomechanical flip-chip device. We begin with the concept and simulations of our microwave resonators, followed by the cleanroom fabrication of the complete microwave circuit. Here, we will focus on the numerous details of each technique, and discuss many potential pitfalls. The second half of the device comprises the high-stress silicon nitride membrane, where we treat the design of the acoustic crystal and the metallization of the mechanical resonator. We combine these two parts to finish the flip-chip device. Here, we will discuss the technical aspects required for the final assembly. We conclude this chapter with an overview of the cryogenic measurement setup.

During the course of this work, many devices have been designed, simulated, fabricated and measured. Two of which have become the core of the research chapters in this thesis. However, for these devices to work, many stages of development and iteration had to be taken beforehand. The designs are based on previous devices made in the research group. In this chapter we will describe the continuation of this process and discuss the new design choices, simulation techniques, fabrication recipes and hardware technologies used in this work.

3.1. Microwave Chip

The microwave devices used in this thesis are designed for two different sets of experiments. The device used in Chapters 4 and 5 was designed and fabricated as described in detail in Ref. [71]. This was aimed at performing linear optomechanical experiments with an increased coupling between the two chips. Building up on these concepts, the device of Chapter 6 was designed to introduce a tunable nonlinearity in the optomechanical cavity, the process of which will be discussed here.

3.1.1. Design and Simulation of the Microwave Circuit

In order to improve the design of the linear optomechanical device in previous work [71], we make three large adjustments in the design of the microwave chip. First, we expect the distance between the chips to be smaller. As the frequency of our cavity is dependent on the square root of the distance, the original resonance will be pushed below our measurable bandwidth of 4 to 8 GHz. Therefore, the microwave cavity was redesigned to have a higher bare frequency without the membrane. Second, we introduce a nonlinearity in the system by capacitively coupling a transmon qubit to the cavity. Third, we want to make our fabrication process more reliable and reproducible. We designed a ring of spacers to, among other reasons discussed below, protect the membrane chip from crashing into the bottom chip [168]. This subsection will discuss the development and design of each of these topics.

Starting with the core of our device, the microwave cavity is a lumped element resonator (LER). Here, we assume the physical dimensions to be much smaller than the wavelength at the resonance frequency. The resonator alternately stores its energy in an electric field between the capacitor pads, and in a magnetic field produced by a current running through the meander inductor [159]. When the metallized membrane is flipped above the pads, an additional large capacitance is created, reducing the frequency of the cavity.

$$\omega_c(x) = \frac{1}{\sqrt{LC}} = \frac{1}{\sqrt{L_{tot}\left(C_0 + C_m(x)\right)}} \tag{3.1}$$

where L_{tot} is the total inductance of the resonator, C_0 its capacitance in the absence of the membrane. The capacitance between the pads and the membrane C_m increases as the distance between the chips x is reduced. Therefore, the frequency of our resonator will be determined by the gap between the two chips. As we do

not have full control over this parameter, as will be discussed in Subsection 3.3, we design the cavity such, to have a resonance frequency between 4 to 8 GHz for the range of distances we expect to obtain. A cavity design with and without membrane is shown in Figure 3.1. In order to know the values above, we need to simulate and calibrate the device.

We design part of the microwave chip using the Python library *Qiskit Metal*, developed by IBM Quantum [169]. Two advantages of this software are that it can export a *GDSII* file, which can be read by our lithography instruments, and the capability to convey the designed elements to the multiphysics finite-element simulation software *Ansys Electronics* [170]. We use some of the standard circuit elements from existing libraries and create custom objects, which is most or our design, by parametrically drawing the circuit elements. In *Ansys HFSS (high frequency simulation software)* we use eigenmode analyses to find the resonance frequencies in our circuit. With *Ansys Q3D Extractor* we use lumped oscillator model (LOM) calculations to find the capacitance between each circuit element. The found values are then compared with an independent *QuCAT* simulation based on the circuit quantization method [171].

When a high-frequency alternating voltage is applied to a metal, its electrons will experience a continuously changing electromotive force (EMF). For a superconductor, the energy required to change the inertia of the Cooper pairs contributing to the supercurrent manifests as an additional impedance. This is called kinetic inductance and is defined by

$$L_k = \frac{m_e}{2n_s e^2}\frac{l}{A} \tag{3.2}$$

where m_e and e are the electron mass and charge, n_s the Cooper pair density, and A the cross section and l the length of the circuit element of interest [172, 173]. For superconducting circuits fabricated in thin films the kinetic inductance can be of the same order as the geometric inductance and, therefore, needs to be incorporated during the design as $L_{tot} = L_k + L_g$. In *Ansys* one can assign properties to materials, such as conductivity, dielectric loss tangent etc. However, the standard material library does not contain any superconductors. Fortunately, there are various ways of including kinetic inductance in the simulation. For example. one approach is to assign a lumped impedance to the metal film [174, 175].

An equivalent method is to define a complex conductivity for the superconducting metal. This method has been used for the work in this thesis. Here, we treat the charge carriers in the metal according to the two-fluid model of classical electrons and Cooper pairs [176, 177]. Where the Drude model describes the classical electrons contributing to conductive losses, the Cooper pairs are lossless [178]. The ratio of the normal electron density and the Cooper pair density is given by

$$\frac{n_n}{n_s} = \left(\frac{T}{T_c}\right)^4 \tag{3.3}$$

where T_c is the critical temperature of the superconductor. The real and imaginary parts of the frequency dependent complex conductivity can be defined as [179]

$$\begin{aligned}\sigma_{Re}(\omega) &= \frac{1}{\mu_0\lambda_L^2}\left(\frac{n_n}{n_s}\cdot\frac{\tau}{1+(\omega\tau)^2}\right)\\ \sigma_{Im}(\omega) &= \frac{1}{\mu_0\lambda_L^2}\left(\frac{n_n}{n_s}\cdot\frac{\omega\tau^2}{1+(\omega\tau)^2}+\frac{1}{\omega}\right)\end{aligned} \tag{3.4}$$

with λ_L the London penetration depth and μ_0 the vacuum magnetic permeability. τ is the mean collision time of the electrons, depending on the vacuum permittivity ϵ_0, the plasma frequency ω_{pe} and the DC conductivity σ_{DC} as

$$\tau = \frac{\sigma_{DC}}{\epsilon_0\omega_{pe}^2} \tag{3.5}$$

Since the circuit elements will be fabricated from 100 nm thin film NbTiN ($T_c \approx 14.4$ K) and Al ($T_c \approx 1.2$ K) and the device measured in a cryostat at ~ 20 mK, the ratio in Equation 3.3 goes to 0 and we treat the materials as lossless [180, 181]. However, the remaining imaginary part of the conductivity contributes to the kinetic inductance of the superconductor. This now depends on the London penetration depth as the only unknown parameter.

The London penetration depth, and thereby the kinetic inductance, is material-dependent and depends, among others, on the thickness of the film [181]. Therefore, in practice, to target the cavity resonance frequency accurately one needs to calibrate the value used for the kinetic inductance for each wafer. We have performed this calibration by fabricating lumped element resonators with a range of frequencies, where we keep the geometric inductance constant and vary the capacitance by changing the geometry of a finger capacitor (substituting the membrane capacitance). We then place the same geometry in *Ansys HFSS* and perform an eigenmode analysis. The London penetration depth is calibrated when our eigenmode simulation agrees with the resonance frequencies of the measured devices. We find a London penetration depth of 510 nm. Although it seems counterintuitive, for thin superconducting films λ_L can indeed be larger than the metal film thickness [180, 182–184].

Now that we calibrated our eigenmode simulation with the materials to use, we can design our circuit. For the flip-chip device we expect to reach a gap size below 1 µm. In order to obtain a measurable cavity frequency we design a short meander inductor ($L_{tot} = 2.66$ nH) and configure a flip-chip geometry in *Ansys*. We draw the top chip to include the phononic shield and etched membrane to account for the relative permittivity of the dielectric material, as shown in Figure 3.1**b**. We parametrically sweep the distance $d = \langle x \rangle$ between the two chips while performing a eigenmode simulations. The charge density on the surface of the superconducting metal is plotted in Figure 3.2**a** for a bare cavity without a membrane. The resonance frequency's dependency on the distance between the

two chips is shown in **b**. For an ideally aligned membrane chip with a distance between 100 and 500 nm we obtain a cavity resonance frequency between 4.1 and 7.9 GHz. The simulated eigenfrequencies are fit by the simple theoretical equation for an LC-resonator (3.1), composed of parallel plate capacitors, given by

$$C = C_{pads} + \frac{\epsilon_0}{d} \cdot \frac{A_1 A_2}{A_1 + A_2} = C_{pads} + \frac{\epsilon_0 A_1}{2d}. \tag{3.6}$$

where $A_{1,2}$ are the overlapping areas of each pad with the membrane. The last equation simplifies the expression for the case of perfect alignment ($A_1 = A_2$). We can calculate the expected single photon coupling rate, as discussed in Chapter 2. Assuming a zero-point fluctuation of $x_{zpf} = 1.09$ fm, based on the effective mass of the mechanical mode $m_{eff} = 7.15$ ng [112], we find the distance dependent coupling $g_0 \propto d^{-3/2}$ as shown in Figure 3.2**b**. For the range of gap sizes we expect to obtain this is an order of magnitude larger than reported in previous work [71].

The second addition to this device is the introduction of a tunable nonlinearity to the optomechanical cavity. This is achieved by capacitively coupling a floating double-island transmon qubit to the linear cavity [185]. The qubit induces a self-Kerr nonlinearity into the cavity. The transmon is flux-tunable by the magnetic flux threaded through the SQUID loop with an area of 125.5 μm^2. The Kerr nonlinearity of the cavity is dependent on the detuning with the qubit and thereby also becomes tunable. In order to retain a large degree of flexibility, we design the qubit and its dipole coupling such that the induced nonlinearity can be brought negligibly small or tuned up significantly large. This would allow for linear optomechical experiments where a large intracavity photon number is required. Moreover,

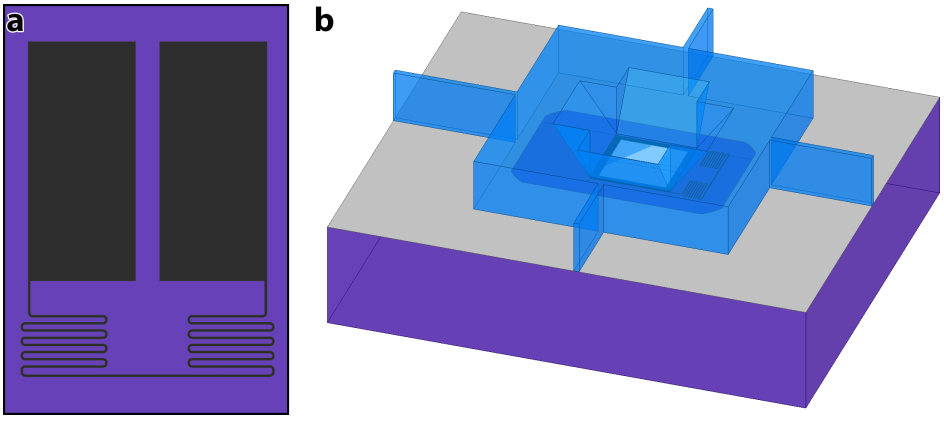


Figure 3.1: Geometry of the microwave cavity and flip-chip device used in *Ansys* simulations. For the eigenmode simulations we use part of the intended design. Panel **a** shows the bare cavity, **b** the flipped device. The silicon bottom chip (purple) with a superconducting ground plane (gray) contain the lumped element resonator (black). A small distance above is the aluminum (white) on the membrane with an excerpt of the silicon phononic shield (blue).

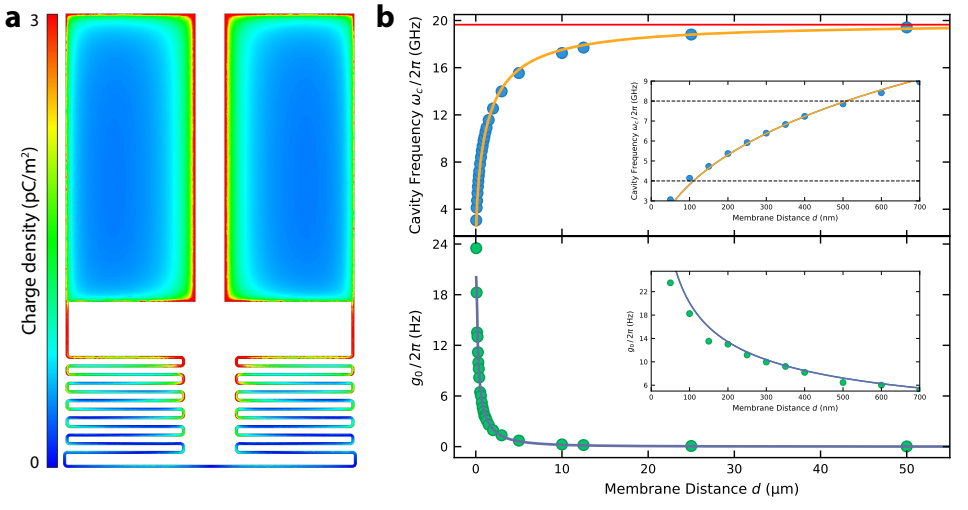


Figure 3.2: Simulated eigenmode of a bare and flip-chip cavity. a *Ansys HFSS* simulated charge density on the surface of the superconducting NbTiN bare cavity for its resonance mode. The charge is localized on the edges between the capacitor pads, confining the electric field in between. The cavity acts as a lumped element resonator. **b** Simulated eigenfrequency and single photon coupling rate g_0 of the optomechanical cavity for a parameter sweep of the distance d between two perfectly aligned chips. Simulated frequencies are shown as blue circles with the red line the asymptotic limit. The fit is the orange line. The inset shows the measurable bandwidth in the experiments between the dashed lines. The calculated single photon coupling rate is shown as green circles and the purple line.

nonlinear optomechanical experiments would likewise be possible, as will be discussed in Chapter 6.

The qubit is designed as a simple transmon qubit, where the inductance of the transmon almost entirely comes from the Josephson junctions. We choose to fabricate Manhattan style junctions, as we have the most experience with this in our research group [186, 187]. More details on the junction fabrication and the applied magnetic field will be discussed in Sections 3.1.2 and 3.4. *Ansys* eigenmode and capacitance simulations were performed to couple the transmon to a readout resonator. We then swept the distance between the qubit and the optomechanical cavity, with the qubit's dipole moment in-line with the cavity, and perform *Ansys* LOM calculations. The charge density on the surface of the NbTiN circuit is plotted in Figure 3.3**a**. In this simulation the top chip with the superconducting metal square on the membrane is located 1 μm above the cavity. Note that these are omitted from the plot for clarity. The meander inductor line of the cavity is cut into two, to treat the capacitor pads as individual objects, such that each couples to the membrane and both islands of the qubit. It can be seen that the charge density is almost entirely located in cavity pads coupled to the membrane, however the coupling to the transmon pads is non-neglectable. We

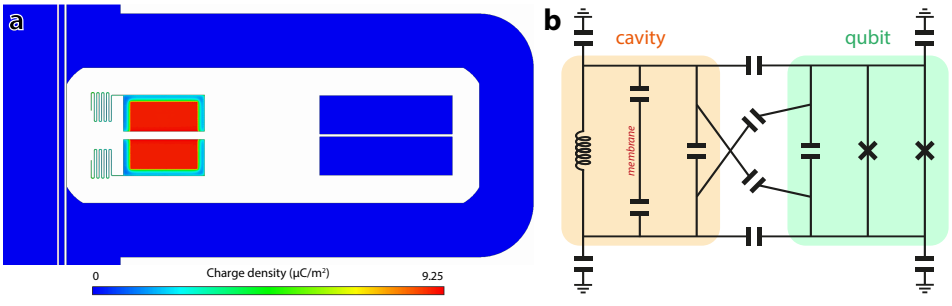


Figure 3.3: Simulated charge density on the NbTiN surface and *QuCAT* implementation. a Simulated charge density on the surface of the circuit of the bottom chip, in flip-chip configuration with a gap of 1 µm. The top chip and membrane metallization have been omitted from the plot for clarity. The resulting capacitances between each element are used in a *QuCAT* model, of which a schematic is shown in **b**.

found that including the phononic shield and membrane etch geometry in the top chip is important, as the permittivity of the material influences the electric field lines coupling the qubit with the cavity. The capacitance matrix of each configuration is implemented in a *QuCAT* circuit modeling our system, as shown in Figure 3.3**b**. From this we extract, with a coupling $g_{cq} = 1$ MHz, the cavity to have an induced Kerr nonlinearity possible to range between 10 µHz and 100 MHz.

In the remainder of this section we briefly discuss the rest of the chip design, shown in Figure 3.4. The coupling of the readout resonator to the qubit is designed to be $g_{ro,q} = 192$ MHz. The readout resonator is coupled to a shorted reflection coplanar waveguide (CPW) feedline. The optomechanical cavity is side-coupled to a transmission feedline [159]. Accordingly, we are able to measure the qubit both through the readout resonator and through the cavity.

The next element is added as a security measure. There are many reasons why a fabricated device would not work, as will be discussed in detail in the rest of the chapter. When the device is cold in the cryostat we can only interact with it through the microwave lines and the DC line to the magnet. To tell us that the main circuit is intact, we add four reference resonators coupled to the transmission line. These have the same meander inductor as the optomechanical cavity, with each a different interdigital capacitor (IDC) to not overlap in frequency [188, 189].

The final part of our main circuit is the ground plane. In the development of this design we aimed for the possibility of a deep-etch into the substrate to prevent contaminating particles to limit the distance between the chips [168, 190]. For this, we have removed almost all of the ground plane, leaving a strip of 200 µm around the circuit. Calibration chips with many resonators including full and reduced ground planes were measured in a cryostat. This resulted in the background spectrum only being slightly altered. Furthermore, there was no significant change in resonator frequencies and their in- and external coupling factors κ_{in}, κ_{ex}, or in

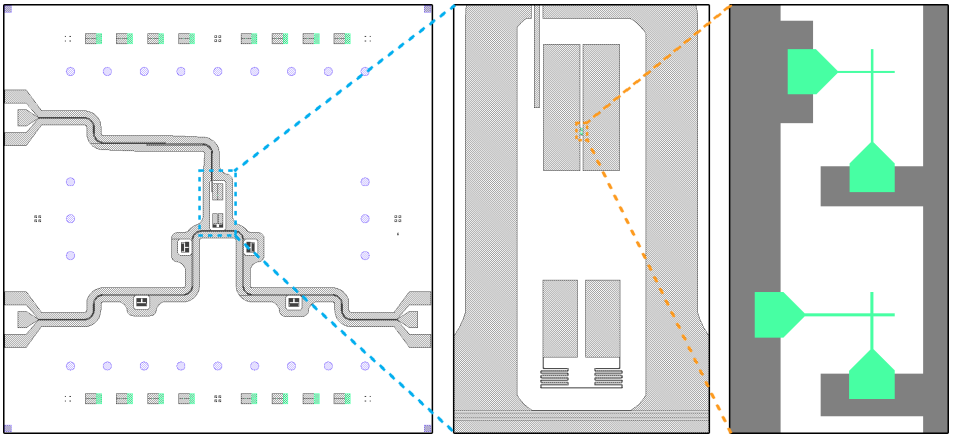


Figure 3.4: Design of the microwave chip. The NbTiN circuit is shown in gray, the ring of silicon oxide spacers in purple, and the aluminum Josephson junctions and qubit probe pads in green.

the transmission and reflection through the feedlines. However, due to maintenance to the plasma etcher at the time of fabrication we were not able to perform this process in the device used in Chapter 6.

The fabrication of the Josephson junctions is a delicate process, as will be discussed the following section. This can lead shorted or disconnected junctions, and in a variability in junction width, leading to an uncertainty in SQUID inductance. Therefore, we design an additional 15 replicas of the qubit and 1 set of islands without junctions at the edge of the chip. These junctions can be probed before the final assembly of the device. A zoom-in of the junction design is shown on the right side in Figure 3.4.

The last addition to the microwave design is a ring of pillars. These spacers prevent the membrane chip from crashing into the bottom chip, and also to help reducing the tilt between the two chips. Moreover, it allows for a more uniform pressure to be applied by the flip-chip pusher, which reduces the risk of breaking the membrane and phononic shield. This step will be discussed in detail in Section 3.3. The 24 cylindrical silicon oxide spacers have a diameter of 250 µm, are 900 nm tall, and are placed underneath the outer frame of the membrane chip, far away from the microwave circuit to prevent dielectric losses.

3.1.2. Nanofabrication Techniques

The devices used for the work in this thesis were fabricated in the cleanroom of the *Kavli Nanolab* at Delft University of Technology [191]. As in the previous section, for the fabrication of the device of Chapter 4 and 5 we refer to Ref. [71]. The fabrication process of the microwave chip used in Chapter 6 will be discussed here. We will treat every technique in the process, and also discuss failed attempts

to emphasize important details. An overview of the fabrication recipe is shown in Figure 3.5.

In order to increase the single photon-phonon coupling, and to introduce a nonlinear element in the circuit the fabrication procedure was extended to five distinct steps. The first step is the preparation of the silicon wafer and deposition of the NbTiN film. The second step treats the patterning and etching of the main microwave circuit in the NbTiN film. Then, the third step contains the deposition and patterning of the silicon dioxide spacers. The patterning and deposition of the Al-AlOx-Al junctions is discussed in the fourth step. Finally, in the fifth step we look at wirebonding the chip to the printed circuit board (PCB) and the final preparation before the membrane chip can be flipped on top.

Step 1: Preparation of the Wafer, Film and Chips

The first choice we have to make for our devices is the materials to use. Our devices are designed to contain microwave resonators, therefore, we are aiming for low losses at radio frequency excitations and a large degree of freedom in design. This points us to superconductors and dielectrics. A more practical, but not less important, motivation for the chosen materials is the expertise in the research group and availability of treatment processes in and the laboratory.

Typically, for superconducting resonator devices with high quality factors, the substrate consists of silicon or sapphire (Al_2O_3). These materials have low bulk dielectric loss tangents at cryogenic temperatures. Moreover, these material grow no or a thin self-limiting oxide layer, which contain radicals that would introduce microwave losses [192]. For the superconducting thin film there is a larger group of materials that are commonly used [161, 193, 194]. For our devices we use niobium titanium nitride (NbTiN), because of its relatively high critical temperature $T_c \approx 14.4$ K and low quasiparticle density at millikelvin temperatures [181, 195, 196]. Both for the bulk substrate and the thin film there are various treatment processes available.

All devices made for this research were made on chips diced from wafers supplied by the *Netherlands Institute for Space Research (SRON)* [197]. The wafers consist of a 100 nm thick NbTiN film deposited on a (100) double-sided polished (DSP), high-resistivity, 525 µm thick, 4 inch silicon wafer [181]. The metal layer is deposited with a customized *Evatec LLS801* sputtering machine, using a 99.8% pure $Nb_{0.7}Ti_{0.3}$ target and a continuous N_2 flow. It has a normal state surface resistivity of $\rho_s = 103\,\mu\Omega$cm and a superconducting surface inductance of $L_s \approx 1$ pH [198]. The metal thickness is expected to be uniform over the wafer within a few percent.

When the wafer is transferred into our cleanroom we first dice it into chips. For this, we prepare the wafer by spin coating *S1805* photoresist at 1000 rpm to create a 1 µm thick layer. It is then baked at 90 °C for 5 minutes on a hotplate. This creates a protection layer to prevent chipping of the edges and contamination of particles during dicing. We place the wafer in the *DISCO Corporation DAD3220*

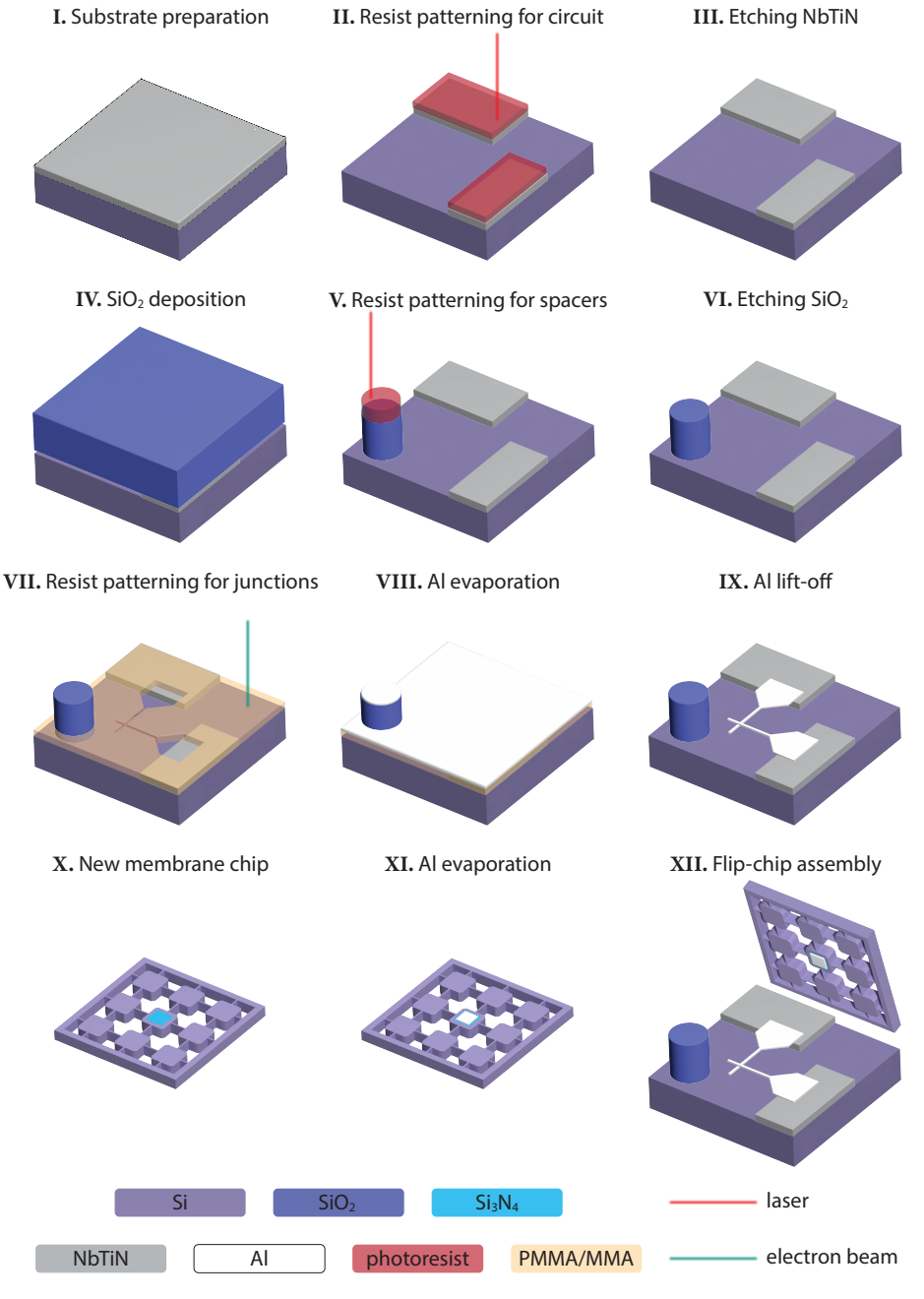


Figure 3.5: Schematic fabrication process of the flip-chip device. Panels **I-IX** show the process of the fabrication of the microwave chip. Panels **X-XI** the steps for the membrane chip. Panel **XII** depicts the procedure of the flip-chip assembly.

dicing machine. For the flip-chip device the microwave chips are 13×13 mm in size, which means we obtain 27 chips per wafer. After the dicing of the individual chips we clean off the resist. The chip is placed at the bottom of a beaker filled with *PRS3000* and warmed up in a bain-marie to 80 °C for several hours. Typically, we leave this process overnight to ensure to get rid of any organic material on the chip. After the stripper, we sonicate the chip for a few minutes consecutively in acetone and IPA, and blow-dry the chip with nitrogen. Before we start the fabrication of the individual chips we inspect them under the microscope.

Step 2: Patterning and Etching of the Microwave Circuit

Now that we have individual clean chips we can start patterning the microwave circuit and two sets of alignment markers on the NbTiN film. We create a mask by spinning *S1805* photoresist at 6000 rpm to create a 400 nm thick layer. Immediately after, we bake the chip at 115 °C for 1 minute on a hotplate. Next, we inspect the resist layer under a microscope with UV filters to prevent exposure. Here, we ensure that the resist layer is uniform and does not contain any contaminations or "comet tails" from solid bits that were in the photoresist. We place the chip into the *Heidelberg μMLA* laser writer and align the chip with the machine to an error of below 10 mrad. As we will have to align the 10×10 mm membrane chip with respect to the 13×13 mm microwave chip, this first alignment step needs to be precise in angle and position. We expose the resist mask with a 365 nm beam with a dose of 120 $\frac{mJ}{cm^2}$. *S1805* is a positive photoresist, meaning the chemical structure degrades when exposed to light, causing it to be more soluble. Afterwards, we develop the sample in the developer *MF-21A* for 70 seconds, after which we proceed by sequentially 40 seconds and 120 seconds in two beakers of distilled water, followed by blow-drying the chip with nitrogen. We inspect the patterned structure under the microscope as shown in Figure 3.6**a**. With this process we typically obtain a resolution of $\sim 1\,\mu$m.

To create the circuit structures in the metal film we need to convey the pattern of the resist to the metal. For this, we perform a reactive ion etch (RIE), using the *Sentech Etchlab 200*. The sample is placed onto an electrically isolated quartz plate at the bottom of a vacuum chamber. An oscillating voltage is applied between the bottom and the top plates and, when a gas is flown through the chamber, the electric field ionizes the gas molecules to create a plasma. The radio frequency (RF) field moves the heavy positive ions very little. However, it accelerates the electrons much faster, which collect on the isolated bottom wafer and sample, creating a negative DC bias voltage. This, in turn, creates a DC electric field which pulls the positive ions to bombard the sample. The ions can collide with the atoms of the sample and sputter the material, and can react chemically. The vertical motion of the ions results in an anisotropic etch, which is favorable for the structures we fabricate. The ions react with the exposed metal, the leftover resist and also, later, the substrate. The selectivity of the etch is determined by the etch rate of each material, depending on the etchant and process parameters used, such as pressure, gas flow and the applied AC power.

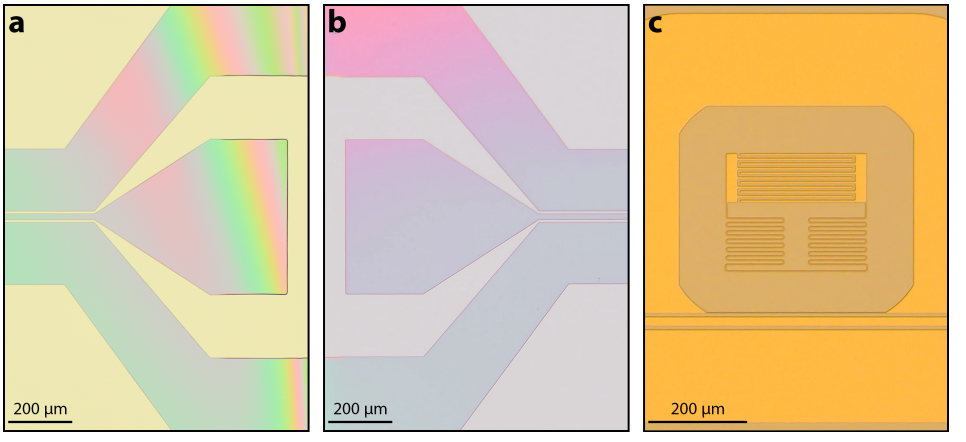


Figure 3.6: Microscopy images of the microwave chip at different stages in the process of circuit fabrication. Panel **a** and **b** show micrographs of parts of the microwave circuit respectively after development of the photoresist and after the plasma etch. **c** Micrograph of a reference cavity after stripping the leftover resist.

In our process we use 50 sccm tetrafluoromethane (CF_4) as the reacting gas at a pressure of 40 µbar [199]. Applying a 100 W RF power ionizes the gas primarily to the ions CF_3^+ and F^+, and the radicals $CF_3^\bullet$ and $F^\bullet$. The etch rate of the NbTiN film is 1.4 $\frac{\text{nm}}{\text{sec}}$. We perform the etch for a total of 78 seconds, of which 6 seconds over-etch to ensure the complete removal of the NbTiN in case of a nonuniform etch rate over the area of chip. As the ions also react to the silicon substrate we perform laser end-point detection in order to prevent a too deep over-etch. Removing too much of the silicon substrate can create a rough surface that affects the adhesion of the aluminum junctions later on. Additionally, it increases the step-height from the substrate to the NbTiN film, which can cause the thin aluminum layer to break. The deposition of the aluminum layer will be discussed in Subsection 3.1.2. Figure 3.6**a** and **b** show part of the circuit before and after the dry etch. The yellow-appearing NbTiN is replaced for the purple silicon substrate, and the leftover resist is thinner, as seen by the color gradient. Figure 3.7**a** shows a failed attempt of a dry etch using SF_6, where the resist layer was too thin. Except for the edge of the chip, all metal structures were removed.

Importantly, due to the variety of chemical species in the vacuum chamber other chemical reactions between these compounds, or between these compounds and the sample, can occur. Most significant is the creation of fluorocarbons. When polymers of this variety are deposited on the surface, large loss channels can be created for our microwave resonators, severely reducing their quality factor. These polymers can form with an imperfect ratio between fluorine and carbon, or compound residues on the sample react with air when opening the vacuum chamber. To prevent this, we perform an *in situ* 50 sccm, 10 second oxygen plasma, at an RF power of 100 W and pressure of 0.5 mbar, after the metal etch, before breaking

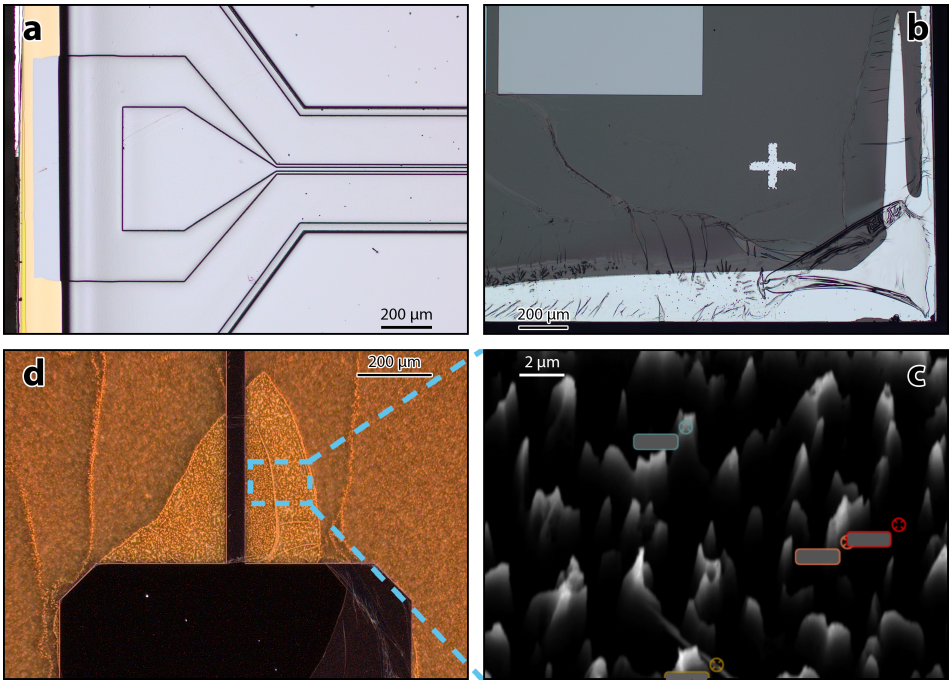


Figure 3.7: Optical and SEM images of failed fabrication attempts. Panel **a** shows an example after RIE-etching where the resist layer was too thin. Except for the edge of the chip, every metal structure was etched away, leaving only the silicon substrate. **b** Micrograph of a failed attempt after a plasma etch using the etchant SF_6. Fluorocarbon sheets are formed and folded over the chip. Panel **c** shows a dark-field micrograph of an SF_6 etch that suffered from micromasking caused by the teflon-like material. Zooming in with an SEM image in **d** shows micropillars of silicon.

the vacuum. Figure 3.7**b** shows a sample where the oxygen plasma was not performed and fluorocarbon sheets were folded over the sample. Another issue that can arise is micromasking. Here, the surface is covered in spots that are etched at a much slower rate or not at all, creating micropillars. A result of micromasking is shown in a darkfield micrograph and a scanning electron microscopy (SEM) image in Figure 3.7**c** and **d**, revealing silicon pillars, as measured with energy-dispersive X-ray spectroscopy (EDX).

Before the final step of removing the left-over resist, we inspect the chip under the microscope to estimate by the color if we indeed etched through the entire metal film. The resist is stripped with the solvent *PRS3000* and cleaned by the same process described earlier. A final microscopy inspection is performed on the etched circuit, as shown in Figure 3.6**c**.

Step 3: Deposition and Patterning of the Spacers

To prevent the membrane chip from crashing into the bottom chip during the assembly of the flip-chip device we fabricate spacers. This also aids the parallelism of the two chips. Silicon oxide (SiO_2) is chosen for the spacers, as this is compatible with the following fabrication steps described below. We deposit silicon oxide over the entire chip using plasma enhanced chemical vapor deposition (PECVD) with the *Oxford Instruments Plasmalab 80 Plus*. We place the sample on a single-sided polished (SSP) silicon oxide carrier wafer on the bottom plate of the vacuum chamber, which is heated to 300°C. Importantly, we place a mosaic of silicon chips all around the sample, as shown in Figure 3.8**c**. This prevents edge effects where the deposited silicon oxide is thicker, which can extend a few mm from the sides of the chips. The deposition process uses 8.5 sccm silane (SiH_4), 710 sccm nitrous oxide (N_2O) and 165 sccm nitrogen (N_2), which are radicalized and ionized by an RF electric field. SiO_2 is deposited at a rate of 1.2 $\frac{\text{nm}}{\text{sec}}$ and the dielectric layer grows 900 nm tall in 12:52 minutes. After the deposition, we clean the chip again in the same way as described above.

For the second patterning step we again spin *S1805* photoresist on the chip, now at 4000 rpm to create a 500 nm thick layer, and bake the chip at 115°C for 1 minute on a hotplate. Next, we place the chip in the laser writer and align to the first set of four alignment markers. The resist is exposed in two steps. First, the spacers are written with a dose of 120 $\frac{mJ}{cm^2}$. Second, the edge of the chip is written again with a dose of 160 $\frac{mJ}{cm^2}$ to counter any edge effects which could result in leftover

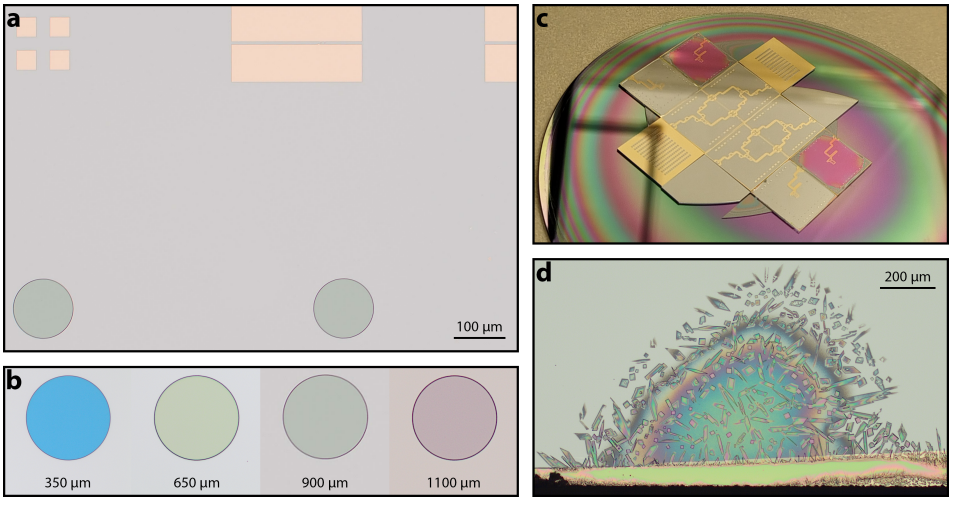


Figure 3.8: Fabrication process of silicon oxide spacers. **a** Micrograph of two 900 nm tall spacers underneath NbTiN structures. Panel **b** displays the color difference for four different spacer heights. **c** The "mosaic" technique of placing chips around the samples to prevent edge effects. Panel **d** shows a micrograph of an attempt where the silicon oxide was only partly etched away, leaving a crystal structured residue.

silicon dioxide close to the launchpads and feedlines. The exposed resist is developed using *MF-21A* following the same recipe as before.

We remove the silicon oxide with a buffered oxide etch (BOE). The solution consists of 7 : 1 volume ratio of 40% ammonium fluoride (NH_4F) and 49% hydrofluoric acid (HF). The latter etches the silicon oxide. We use the BOE solution rather than pure HF to retain a constant HF concentration and thus a constant etch rate [200]. The etch rate for the deposited silicon oxide is 1.1 $\frac{\text{nm}}{\text{sec}}$. We place the chip vertically in a basket, ensuring all of the top surface is exposed, and submerge it in the acid for 13:30 minutes. The basket is transferred twice to a water bath for several minutes, before blow-drying the chip with nitrogen. If not all silicon dioxide has been etched away there will be a thin film of water on the surface before blow-drying, as silicon dioxide is hydrophilic. Immediately after, we strip the leftover resist in *PRS3000* with the same recipe as before, after which we inspect the spacers under the microscope, as shown in Figure 3.8**a**. The color of the oxide is thickness dependent, as shown in **b**, and is dark green (900 nm) for our device. If the etch is not done uniformly, regions of thin oxide can remain and small pieces can be redeposited, as shown in **d**. Silicon dioxide being a lossy dielectric material can reduce the quality factor of the microwave resonators. The spacers are therefore designed to be far removed from the circuit.

Step 4: Patterning and Deposition of the Junctions

To create a nonlinear optomechanical device we need to introduce a nonlinearity in the circuit. This is done by fabricating a double-island transmon qubit. The NbTiN capacitor plates we already made and, here, we fabricate a superconducting quantum interference device (SQUID) connecting those. In this step, we describe the fabrication process of the Josephson junctions of the SQUID.

To obtain the resolution needed for junctions with an overlap area of the order of 100 nm we use electron beam lithography (EBL). First, we prepare the substrate by performing a 50 sccm, 2 minute oxygen plasma at an RF power of 50 W and pressure of 10 µbar, to clean the surface. Then, we build a bilayer resist stack of MMA 8.5% EL6 and PMMA 950K A6. The first step is to bake the chip on a hotplate at 120 °C for 2 minutes. Next, we spin coat the MMA at 2000 rpm to create a 180 nm thick layer and perform a post-bake at 180 °C for 3 minutes. For the second layer we spin coat the PMMA at 1500 rpm to create a 500 nm thick layer and perform a post-bake at 180 °C for 5 minutes. We pattern the junctions using a *Raith EBPG-5200* electron beam with a spot size of 5 nm and a dose of 1700 $\frac{\mu\text{C}}{\text{cm}^2}$. The e-beam resist stack is then developed in a cold (7 °C) IPA : H_2O 3 : 1 solution in a sonicator at the lowest setting for 2 minutes. Afterwards, the chip is transferred to an IPA bath for 15 seconds and blow-dried with nitrogen. After inspection under the microscope to check the alignment of the junctions, the chip is ready for the aluminum evaporation.

The aluminum evaporation is a delicate deposition step and requires a clean surface. For this, we perform the next steps as quickly as possible to prevent the

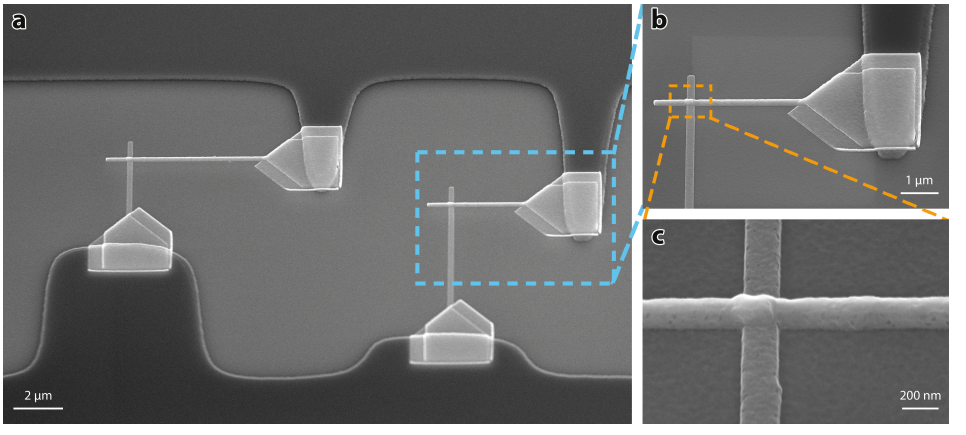


Figure 3.9: Scanning electron micrographs of the aluminum SQUID of a transmon qubit. Three different magnifications of a SQUID made of evaporated aluminum (white). Each image is taken with a tilt of 40°. Panel **a** shows the entire SQUID with an area of 134 µm^2. Zooming in, panel **b** shows the intact step edges of the aluminum from the silicon substrate (gray) to the NbTiN circuit (black). **c** The Manhattan-style Al-AlOx-Al Josephson junction.

growing of oxides or contamination of particles. First, we again perform a 10 second oxygen plasma (50 sccm, 100 W, 10 µbar). Then we do a short submersion in a BOE-solution: H_2O for 10 seconds, 7 : 1 BOE for 1 minute, twice H_2O for 1 minute, H_2O for 5 minutes, and finally blow-dring the sample.

After the acid clean, the chip is immediately mounted on the evaporator cassette and transported into the load-lock of the *Plassys MEB550 S2* to be pumped vacuum. For fabrication of Josephson junctions the main challenge is to create a good connection between the two metal layers. There are several common geometries for these kind of Josephson junctions, each with their own characteristics and fabrication process [201, 202]. We choose to fabricate Manhattan-style junctions, as this process knowledge was already available in the research group [186, 187]. Using the tall resist stack we can evaporate aluminum into the narrow streets individually by performing double-angle shadow evaporation [203–208].

The evaporator system is capable of depositing metal on the sample with freedom of tilt and angle. An electron beam is aimed into a crucible filled with high-purity aluminum, which heats up and evaporates. The evaporated atoms move towards the sample, where the entire surface of the chip will be covered. The deposition rate and total amount is monitored using a piezoelectric material. An RF source drives the material while its resonance frequency is measured. The deposition rate is determined from its frequency shift. Inside the main chamber we are also able to perform dynamic oxidation, where the pressure and flow of oxygen in the vacuum chamber is remained stable. This allows for a constant rate of growth of the AlO_x layer.

After the loading of the sample, it is transferred to the main chamber which is then pumped down to a pressure of $6.0 \cdot 10^{-7}$ mbar. A preparation step is first performed to lower the pressure of the chamber further. This is to prevent impurities in the junctions. The electron beam is aimed into a crucible with titanium, which is evaporated into the main chamber, acting as a titanium sublimation pump (TSP) [209]. The walls of the chamber become coated with a thin layer of titanium. Components of the remaining gas can react with the titanium, which results in solid products, thereby reducing the pressure in the chamber. The sample is shielded from this process, as titanium would be undesirable on the chip. This lowers the pressure to $1.1 \cdot 10^{-7}$ mbar, where we can start the deposition of the junctions.

The first layer of 35 nm thick aluminum is evaporated under a tilt of 35° at a temperature of 23 °C with a deposition rate of 2 $\frac{\text{Å}}{\text{sec}}$. The high tilt angle of evaporation means that we can deposit aluminum at the bottom of one of the resist trenches, while for the other trench 90° rotated the aluminum will only reach the side wall of the developed resist. Secondly, a few nm thick aluminum oxidation layer is created that will be the core of the Josephson junction. This is grown at a pressure of 1.3 mbar in 11 minutes with the cassette perpendicular to the source (0° tilt). The chamber is then pumped back to a pressure of $2.2 \cdot 10^{-7}$ mbar. The cassette is rotated 90° with respect to the first step and again placed at a tilt angle of 35°. Here, the 75 nm thick second aluminum layer is deposited at a rate of 5 $\frac{\text{Å}}{\text{sec}}$ in the second street while the shadow deposition only reaches the side wall of the first trench. Lastly, another 11 minute oxidation step is performed to grow a cap layer over the junctions, as the thin layer is self-terminating. This prevents the junctions to react with air when the vacuum chamber is vented.

This technique results in Josephson junctions with a reproducible width, thickness of each layer and overlap area, and thereby a consistent inductance L_J. Furthermore, it leads to a consistent and good connection between the aluminum junction and the NbTiN capacitor pads of the qubit [186, 187].

We inspect the deposited aluminum under the microscope before we perform lift-off. The chip is placed in a beaker of hot N-methyl-2-pyrrolidone (NMP) at 80 °C and left overnight. The solvent strips the resist stack to which the aluminum is adhered. We use a pipette to flow the hot NMP over the surface, such that the resist and aluminum film are released from the substrate. The chip is then transferred to two beakers of IPA (each 5 minutes) and blow-dried. We inspect under the microscope whether the junctions are aligned with the NbTiN pads of the qubit. Figure 3.9 shows SEM images of an aluminum SQUID fabricated with this recipe. It can be seen that the over-etched substrate is smooth and the step edges onto the transmon islands are intact. The higher magnifications show one of the Josephson junctions.

However, one has to be cautious with fabrication processes performed after the junction deposition. In Figure 3.10 we show a failed fabrication attempt. After

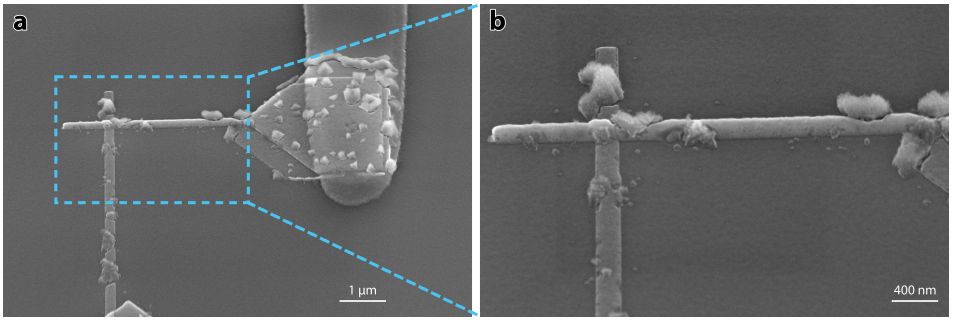


Figure 3.10: Scanning electron micrographs of crystalline aluminum fluoride defects in a Josephson junction. Fluor residues react with the aluminum to form crystals, thereby destroying the junction. The SEM images are taken with a tilt of 40°.

the junction evaporation another dry etch was performed using SF_6 without special post-etch treatment. Residual fluorocarbon polymers reacted with moisture in the air, creating crystalline aluminum fluoride defects in the aluminum, thereby destroying the junctions [210, 211]. The crystal growth can be prevented by subsequently an *in situ* oxygen plasma, direct transfer to distilled H_2O, and lastly a warm overnight organic material stripper (e.g. *PRS3000*). No crystalline defects were observed for multiple weeks on chips treated as such.

In the design we have included several test qubits of the same geometry outside the spacer area, as shown in Figure 3.4. These are used to measure the room temperature conductance between the two capacitor plates of the transmon, as these are directly related to the Josephson inductance. First, another 1 minute oxygen plasma is performed at 50 W, which does not impact the junctions. Second, two tungsten probe needles with a 7 µm tip radius are scratched into an additional aluminum layer, which covers part of the qubit capacitor pads. A low DC current is applied and the voltage drop across the junctions is measured with a custom-built multimeter. We then convert the measured voltage to a resistance and inductance of the SQUID. Assuming an increased critical temperature for thin film aluminum [180, 212], we can estimate the superconducting energy gap for our junction thickness to be $\frac{1}{\pi\hbar}\Delta_{gap} \approx 84$ GHz. For the Josephson inductance we obtain the relation

$$L_J = \frac{e^2\Phi_0^2}{\pi^3\hbar\Delta_{gap}} \cdot R_N \approx 1.20 \cdot R_N \left(\frac{\mathrm{nH}}{\mathrm{k\Omega}}\right) \tag{3.7}$$

where R_N is the measured normal state resistance [213, 214]. If the measured inductance of all probed qubits are within the expected range, we can expect the qubit coupled to the cavity also to be intact and we proceed with the last fabrication steps on this chip. The designed Josephson junctions shown in Figure 3.4 have a width of 157 nm and 191 nm respectively, from which we expect a SQUID inductance of 4.77 nH. The average probed inductance is $L_{\mathrm{SQUID}} = 4.91$ nH. Therefore, we expect the evaporated junctions to have widths only $\sim 3\%$ smaller, using the

calibrated conversion in our research group as discussed in Ref. [186, 187]. After the probe measurements, we perform another cleaning step, using acetone and IPA in the sonicator at the lowest power, and inspect the chip under the microscope.

Step 5: Preparation for Flip-Chip Assembly

As this is the first stage of the assembly of our flip-chip device, we will dive into all the meticulous details. After all elements on the microwave chip have been made, we prepare it to flip the membrane chip on top by securing the chip in a printed circuit board. The PCB is designed to tightly fit in the flip-chip holder, while the top chip is still able to move and be secured without damaging the bottom chip. Outside the cleanroom, sub miniature push-on (SMP) connectors are soldered to the PCB. The PCB has a square recess in which the chip can lie. A flat surface is chosen over a ledge, such that, when we on push the top chip, the bottom chip cannot bow and remains parallel [215]. However, there are disadvantages to this base below the chip. There is a possibility to create a box mode, which can couple to the cavity mode if the frequencies overlap. Furthermore, crosstalk between the different ports can occur. We carefully clean the PCB to ensure no particles lie in the recessed area. Then, we place the chip inside, importantly without any varnish. Although varnish can ensure a good thermal contact between the chip and the PCB, it will be nonflat on a scale larger than the expected gap size between the two chips. Moreover, when cooling the device down to mK temperatures the expansion rate of the varnish is different from that of silicon, creating tension in the chip, which can cause the chip to bow. Instead, we ensure the chip is thermalized by hard clamping in into the PCB, which is described in Section 3.3.2.

The chip is connected to the PCB by ultrasonic wedge bonding with the *West · Bond 4KE* wirebonder. A 25 µm thin AlSi alloy (99 : 1) wire is used. As there is a risk of breaking the bonds during the flip-chip assembly, in order to prevent losing electrical contact, we place as many bonds as possible between the CPW feedline on the PCB and the launch pad, typically three or four. Additionally, on the top and bottom edges of the chip we place many wirebonds to secure the chip in place, and for additional thermalization, as shown in Figure 3.11. Note that, because we do not use any varnish, the chip tends to slide during the first few bonds. A translation or rotation of the chip will result in a misalignment with the membrane. Furthermore, the sliding can break any already placed bonds. We therefore carefully tune the height of the loop motion and applied force of the machine. We first secure the chip in place due by bonding around the chip. The launchpads are bonded last.

After bonding, we remove any particles that fell on the surface by blowing carefully from the side with nitrogen and inspect under the microscope. Now that the fabrication of the microwave chip is complete it is ready for the membrane chip to be flipped on top.

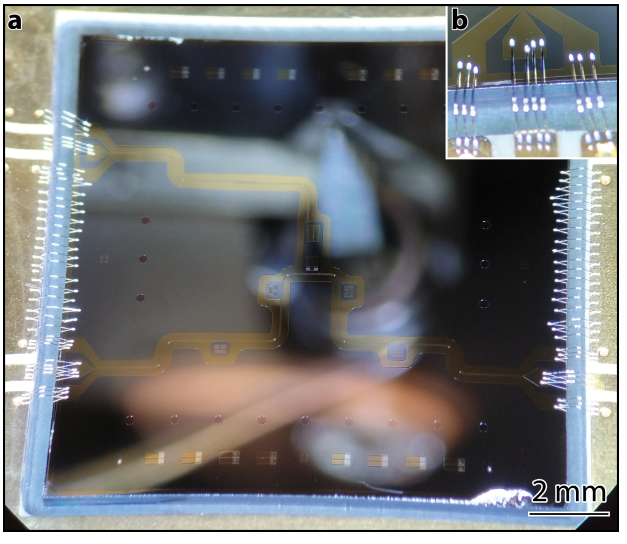


Figure 3.11: The wirebonded microwave chip. Optical micrographs of the microwave chip wirebonded to the PCB. Panel **a** shows the entire chip with bonds on two sides. **b** Wirebonds on a launchpad and ground plane.

3.2. Membrane Chip

To optomechanically couple a low-loss mechanical resonator to the microwave cavity there are several conceptual and technical considerations to be taken into account. The membrane is metallized for it to capacitively couple to the microwave cavity, and is situated within a phononic crystal. Based on the work performed in Ref. [71] for the device in Chapters 4 and 5, here, we discuss the continued development of our mechanical resonator. The design and fabrication discussed in this section has lead to the device used in Chapter 6.

3.2.1. Phononic Shield Design

The high-stress stoichiometric silicon nitride (Si_3N_4) membranes used in this thesis are optimized to have a high mechanical quality factor. The membranes are located in the center of a lattice structure etched in the silicon substrate. This phononic shield minimizes energy dissipation of the membrane's motion by reducing clamping losses due to a mechanical impedance mismatch [149]. The wave vectors of the allowed excitations in the lattice can be calculated with band theory, allowing to design the frequency response of the acoustic crystal.

The designs of our phononic shield are based on that developed in the Regal Lab [149], where a membrane surrounded by an acoustic crystal was shielded from mechanical noise. The shields in the two devices described in this work were designed using finite-element simulations in *COMSOL Multiphysics* [113]. Eigenfrequency analyses were performed using a linear elastic material in the *Structural Mechanics* module.

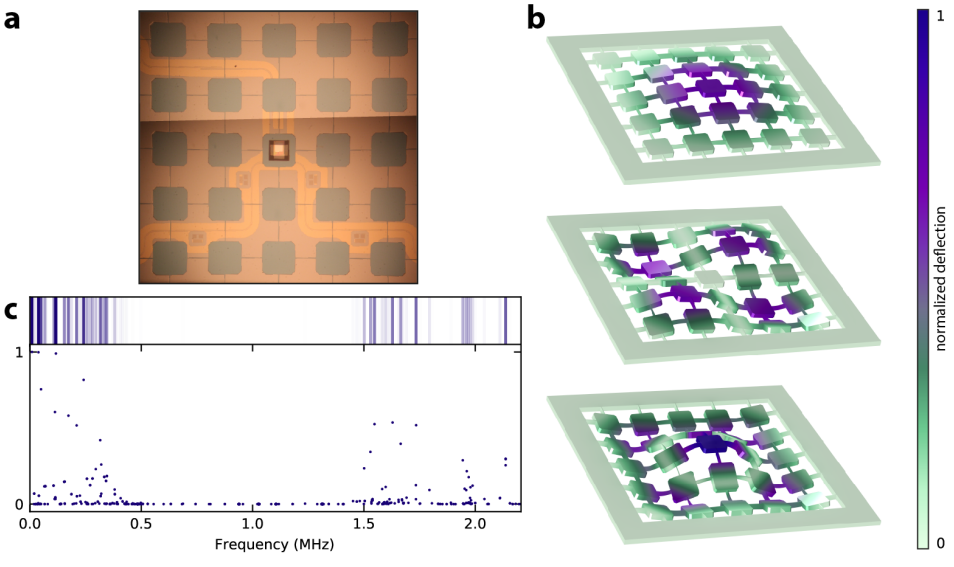


Figure 3.12: Design and simulated eigenmodes of the phononic shield. **a** Photograph of the membrane chip with the patterned phononic shield. **b** Three of the simulated mode shapes of the membrane chip, normalized to unity. **c** Simulated mode spectrum. The transparency of the lines indicate the amplitude of the membrane in the orthogonal direction of the chip. Darker lines correspond to modes that would couple to the microwave cavity, e.g., the top and bottom modes in **b**.

The chip is 10×10 mm in size with a $300 \times 300\,\mu$m square membrane located in the middle. From Equation 2.22 we find a fundamental frequency of 1 MHz with a density $\rho_r = 3180\ \frac{\text{kg}}{\text{m}^3}$ and tensile stress of $\sigma = 0.95$ GPa. The two-dimensional square lattice is build up from square parts with snipped corners, each connected by four narrow tethers, as shown in Figure 3.12**a**. We leave an outer rim of 1 mm, where the chip will be supported on the spacers of the microwave chip. This circumference is also where the flip-chip holder will clamp, as will be discussed in Section 3.3.2.

From measurements of the cavity frequency we find that we are suffering from vibrational noise, changing the distance between the two chips. Since the crystal structure is a band-stop filter, the lattice will have modes that can be excited in the frequency range of vibrations (< 10 kHz). Some of these modes might have an amplitude in the orthogonal direction of the chip. This could cause the central pad, in which the membrane is located, to move. Thereby, the size of the gap and the capacitive coupling to our microwave cavity will be changed. We perform a parameter sweep on the geometric dimensions in the unit cell and perform a *COMSOL* eigenmode simulation with the boundary conditions stated above. Here, we focus on the amplitude of the membrane for the found excitations, in the direction perpendicular to the chip's surface. Three simulated spatial profiles are shown in Figure 3.12**b**. It can be seen that for the $(1:1)$ and $(2:2)$ modes (top

and bottom) the membrane moves significantly, where for the (3 : 1) mode (middle) the membrane stands still. Figure 3.12**c** shows the simulated mode spectrum. A bandwidth of 1.4 MHz is present, centered around 1 MHz without mechanical modes of the phononic shield in the orthogonal direction. Darker lines correspond to modes that would couple more to the microwave cavity in the flip-chip geometry, lighter lines to modes that do not. Most excitations below the band-stop region are located within the motion of individual unit cells of the lattice, and most excitations above are located in the edge, or substrate, of the chip.

We find an optimal configuration with 5 unit cells in both directions. The pads are 950 µm square, connected via 600 µm long and 20 µm wide tethers. The outer tethers connecting to the frame have a length of 425 µm. Further analysis of geometric and material parameters could improve the width and depth of the band-stop filter [216].

3.2.2. Membrane Chip Fabrication

In previous devices, the fabrication of the membrane chip was the most work, where the phononic shield was fabricated in-house. This is described in detail in Ref. [71]. In this work, we make use of membrane chips purchased with pre-made phononic shields by our design from Norcada [217]. These chips have been used in the development that lead to the device of Chapter 6.

A schematic overview of the fabrication process of the membrane chip and its assembly onto the microwave chip is shown in Figure 3.5**X-XII**. To couple the silicon nitride membrane capacitively to the microwave cavity we metallize the membrane. The deposited metal should not contain any significant stress, as this will change the stress profile of the membrane and thereby change the vibrational mode we couple to. However, since the chip already contains the phononic shield,

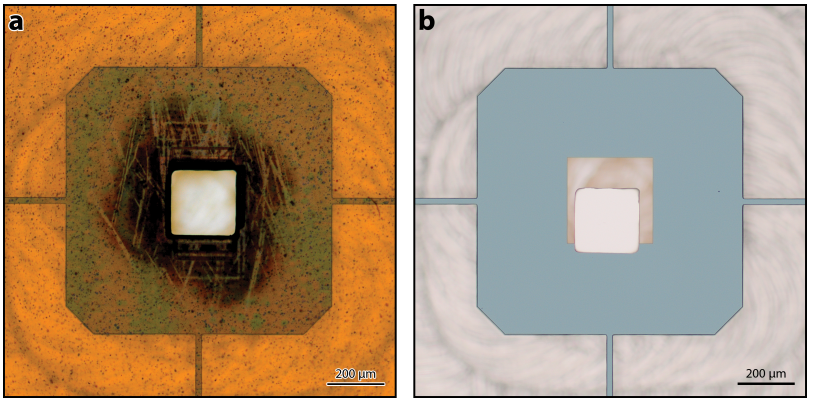


Figure 3.13: Shadow mask evaporation of aluminum on the membrane. **a** shows a micrograph of the kapton stencil mask aligned on top of the membrane before evaporation. **b** Micrograph of the metallized membrane after evaporation.

we cannot perform any lithography processes. Instead, we perform shadow mask evaporation to deposit aluminum on the membrane [218]. We use a lasercut kapton hard mask with one $250 \times 250\,\mu m$ square hole on top of the membrane and four square alignment holes on the phononic shield, as shown in Figure 3.13**a**. We align and secure the mask on top of the membrane in a holder designed to be attached to the cassette of the *Plassys MEB550 S2* evaporator. We typically achieve a misalignment smaller than $30\,\mu m$. A similar evaporation process recipe was used as for the junction deposition. Here, we evaporated once 50 nm of aluminum and performed an 11 minute oxidation step.

We inspect the membrane under the microscope before and after removing the kapton mask. Here, we pay special attention to the alignment and the cleanliness of the aluminum, the membrane and the entire chip. Figure 3.13**b** shows the metallized membrane after removing the mask. The small misalignment of the metal is caused by a shift of the mask during vacuum pumping. This could be improved by securing the mask using leaf springs. If there are particles on the chip we perform an extra cleaning step, where we place the chip in a specially designed holder to stand upright in a beaker of IPA in the *Leica EM CPD300* critical point dryer. When the chip is completely clean it is ready to be flipped in the device assembly.

3.3. Optomechanical Flip-Chip Device

Creating the optomechanical assembly has been one of the biggest challenges in this thesis. Based on the work in Ref. [71, 219], we continue the development of our flip-chip geometry and fabrication. Our aim is to reduce the distance between the two chips, in order to increase the coupling between the microwave cavity and the mechanical resonator. Additionally, we want to make our fabrication process more robust and reliable. These goals are often contradictory, however, in this section we describe the design and assembly techniques to achieve both simultaneously.

3.3.1. Design of the Flip-Chip Holder

The flip-chip technique is a method to couple a system based on one chip, to a system located on another. Within this technique there are several approaches. A widely used approach is wafer bumping for devices in which the gap between the two chips can be on de order of $10 - 100\,\mu m$ [220]. For optomechanical systems, however, this is typically too large, as the parametric coupling is weak. Flip-chip techniques have been developed coupling a membrane to an optical or (semi-) 3D microwave cavity [48, 51, 57, 64–68, 72–74, 128, 144, 221–226]. Membranes have also been coupled to 2D microwave cavities using a flip-chip technique [48, 51, 64, 68–73, 75]. In most of these systems the two chips are bonded by epoxy, which can cause additional challenges. First, epoxy has a different thermal expansion rate than silicon, which will therefore create stress on the sample when cooled down. This could cause either of the chips to buckle, which creates unreliable gap sizes. Second, it is hard to control the amount of epoxy applied. The viscosity can also cause the epoxy to creep over the surface of the chip [186]. This can

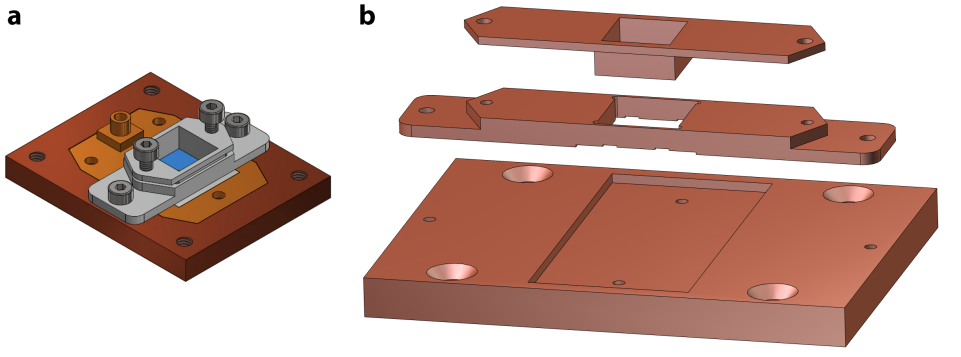


Figure 3.14: Rendered schematics of the two flip-chip holders. **a** Assembled design of the flip-chip device used in Chapters 4 and 5, adapted from [71]. **b** The copper base, xy-aligner and pusher of the flip-chip holder used in Chapter 6.

result in inconsistencies in thickness or tilt the chip. Reducing the amount of glue and placing the droplets in strategic places improved this. Peiter has developed a mechanically clamped flip-chip holder, presenting a new assembly platform [71]. Carrying on this progress, we identified several challenges, which will be discussed here.

The flip-chip holder is comprised of three parts: a copper base in which the PCB with the microwave chip is mounted that can be installed and thermalized to the cryostat; an xy-aligner to move the flipped membrane chip; and a spring-loaded pusher to clamp the two chips to each other and to the holder. A schematic image of Peiter's device is shown in Figure 3.14**a**. Our next goal was to reduce the distance between the two chips. The first naive attempt was to apply more pressure by rotating the screws tighter. This often caused the membrane to break, either instantaneously, or during a thermal cycle. Second, we reasoned that any particle larger than 1 µm on either chip would prevent the chips from getting close and increase the risk of breakage [227]. Hence the meticulous fabrication procedure described above.

Figure 3.14**b** shows the design of the newly adjusted flip-chip holder. Placing the pusher screws further apart has two advantages. First, top pusher is pressed down by slowly iteratively rotating the two spring-loaded screws. Lowering a single screw at a time will induce a smaller tilt of the top chip. Second, it allows for placing the entire device underneath the microscope objective, making the assembly process much more manageable. In many iterations we observed the two chip to have some degree of divergence from a perfectly parallel orientation. This was attributed to the varnish used to secure the microwave chip to the PCB. Therefore, we created an an epoxy-free, fully mechanically clamped device. In Section 3.1.2 we discussed how the chip was held in place with wirebonds. Notches were made in the xy-aligner to prevent shorting the center feedline on the chip to ground. As an important detail, the aligner was also milled in order to only touch the copper

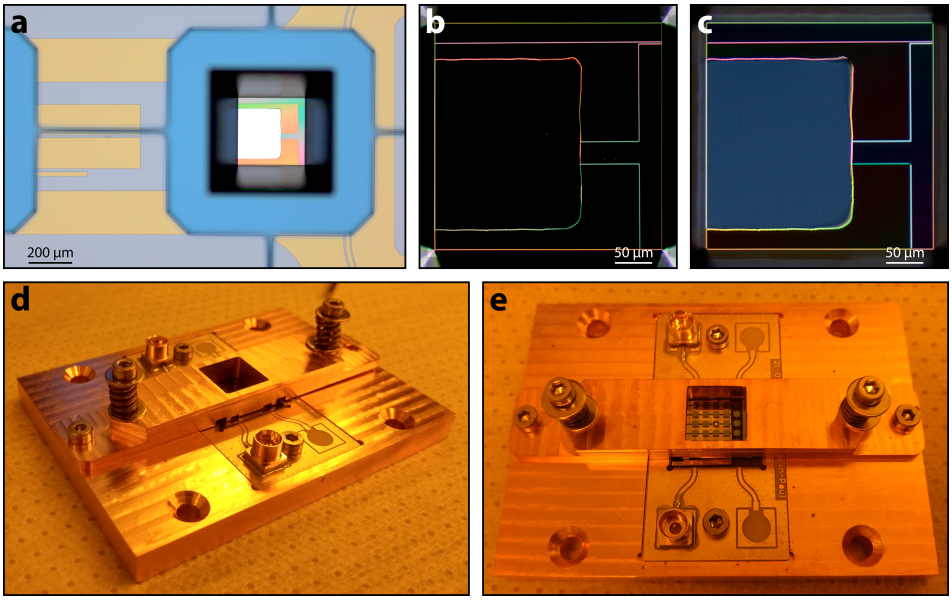


Figure 3.15: The assembled flip-chip device. **a** A brightfield micrograph of the membrane flipped onto the microwave chip after assembly. White light interference can be seen through the membrane. Panels **b** and **c** respectively show a darkfield and DIC micrograph, confirming both chips are clean and not touching. **d** and **e** Photographs of the full flip-chip holder with spring-loaded screws. The membrane can be seen as a white square in the blue phononic shield. The microwave circuit is visible through the crystal.

base and the sides of the membrane chip. Thereby it does not apply a force on the bottom chip, which was previously causing it to bow [215]. Furthermore, all elements were manufactured out of copper to ensure the same thermal expansion during a cooldown.

3.3.2. Flip-Chip Assembly

In this final fabrication stage we combine the two chips into a single device. The procedure is performed underneath a microscope in the cleanroom to ensure no particles contaminate the sample. First, the PCB is screwed into the copper base. The xy-aligner is gently placed on top of the base with tweezers, ascertaining that it does not touch any of the circuit, or that it shifts and breaks the wirebonds. The part can be moved for course alignment when the inserted screws are just lightly tightened. Then, the membrane is flipped upside down into the square chamber of the aligner and placed onto the spacers on microwave chip. Typically, we immediately see bright colors through the membrane caused by white light interference. Constructive interference occurs when the distance between the chips is an odd integer multiple of half the wavelength. Therefore, the color can be used as an indication of the gap size [228].

Underneath the microscope, the xy-aligner is gently pushed sideways with tweezers until the aluminum on the membrane is satisfactory aligned with the cavity. This generally changes the color profile seen through the membrane, indicating that the distance is not yet stable. Then, its screws can be tightened, securing the membrane chip in the xy-direction. Last, the pusher is carefully placed onto the outer frame of the membrane chip and spring-loaded screws are gradually and alternately tightened. Pressing the chips together causes the color profile to become more uniform (chips become parallel) and more intense (chips get closer). The final configuration is shown in Figure 3.15**a**. The bright-field micrograph shows intense green and pink colors, indicating a submicron gap. The aluminum and membrane are aligned with the cavity's capacitor pads. The dark-field micrograph in **b** indicates there no particles between the two chips, as these would appear as bright spots. In the differential interference contrast (DIC) micrograph in **c** it can be seen that there is no deformation of the membrane causing a different stress profile. We can thus conclude the membrane is not touching the microwave chip. **d** shows assembled device, which is now ready to be transported to the cryostat.

It is worthwhile to note that with every fabrication process described above, and every process in the development of this recipe, can fail, and usually has failed. To give an impression of some of the possible unsuccessful processes, we show a collection of failed attempts in Figure 3.16, each of which we have learned a lot from.

3.4. Cryogenic Setup

The devices in this research have been measured in two different dilution refrigerators. Moreover, for test and calibration devices we worked in two more cryogenic systems. The experiment in Chapter 4 is performed in a *Oxford Instruments Triton 200*. Here, the device was mounted in a gold-plated puck, which was screwed into the bottom of the mixing-chamber plate with the help of a bottom-loading mechanism. Following, the measurements in Chapters 5 and 6 took place in a *BlueFors LD250* system mounted in a passive vibration damping frame. The devices were mounted on a thermalized copper mass attached with springs to the mixing-chamber plate, which provided additional vibration isolation.

3.4.1. Vibration Isolation

In each chapter we discuss the vibrational effects we see on our optomechanical devices, as these can also partially couple to our cavity. The effect we see is cavity resonance frequency fluctuations, resulting in an increased time-average linewidth. For the device in Chapter 6 we expected to reduce the interchip distance, which would make us quadratically more susceptible for vibrations. Therefore, in order to reduce the frequency noise further we designed a mass-spring system to hang underneath the mixing chamber plate inside the cryostat.

A mass-spring system is a mechanical low-pass filter and is typically designed with a cutoff frequency well below the noise to be damped. However, we have

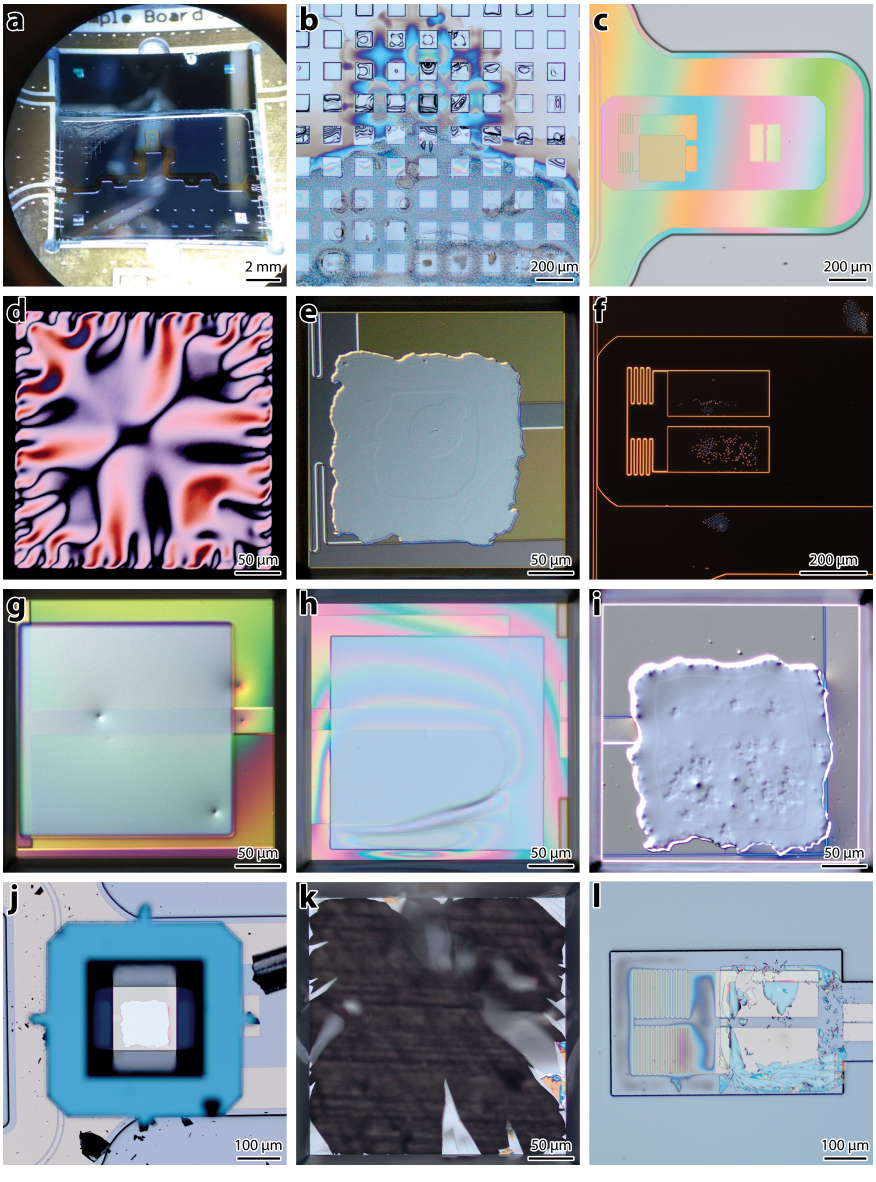


Figure 3.16: A collection of unsuccessful fabrication attempts at various stages in the recipe. All images are brightfield optical micrographs, unless mentioned otherwise. **a** A microwave chip broken in two pieces. **b** Residue of thermalization oil that mixed with the plasma of a Bosch etch. **c** A misaligned flipped sapphire chip showing a large tilt by the color gradient. **d** DIC image of sputtered Al + 1% Si inducing stress on a membrane. **e** DIC image showing ballooning caused by water underneath an evaporated aluminum film. **f** Darkfield image showing condensation formed between the chips during warmup. **g** DIC image showing particles touching and deforming the membrane. **h** and **i** brightfield and DIC image of a membrane crashed into and stuck to the bottom chip. **j** A broken phononic shield. **k** and **l** Shattered membranes.

Table 3.1: Table of analogous mechanical and electrical quantities. Adapted from [229].

Mechanical			Electrical		
Force	F	(N)	Current	I	(A)
Velocity	v	(m/s)	Voltage	U	(V)
Admittance	1/Z	(s/kg)	Impedance	Z	(Ω)
Mass	m	(kg)	Capacitance	C	(F)
Elasticity	1/k	(m/N)	Inductance	L	(H)

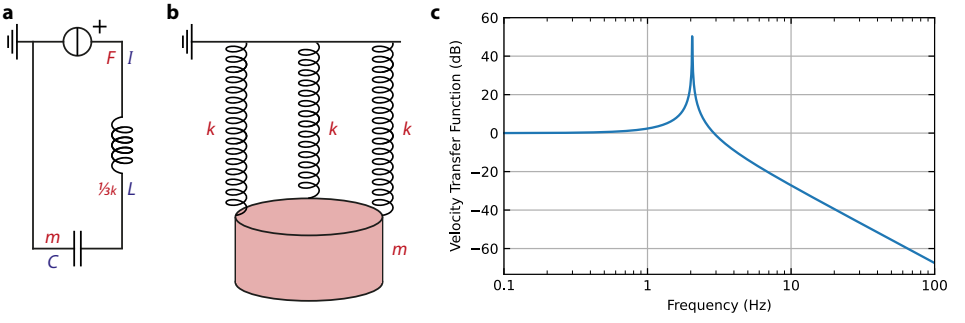


Figure 3.17: Filter response function of the mass-spring mechanical damper. Panel **a** shows the analogous electric and mechanical circuit diagram of the mechanical filter schematically depicted in **b**. Its calculated response function is shown in **c**.

to keep in mind that it is also a harmonic oscillator itself and therefore has a resonance frequency. When designing a mass-spring system for a cryogen-free dilution refrigerator one thus has to take into account the frequency of the pulse-tube, which is typically 1.42 Hz. A simple mass-spring system is a second order low-pass filter, which above its corner frequency attenuates vibrations by 40 dB per decade. Another practical limitation is that the springs should be the stiffest connection between the mixing chamber plate and the mass in order to prevent a mechanical leak. We thus have to use flexible cables to connect the device and flexible thermal links to thermalize the mass. One contradictory requirement is that the thermal conduction scales with the area of the link, which typically leads to a stiffer connection. Note that the wavelength of sound in metals lies above 50 kHz, which can travel through the springs. To reduce this to some extent we place teflon tape between all metal-to-metal connections.

For cryogenic systems vibrations have to be damped by reflection rather than dissipation, as the latter will induce a heat load. One method to design such a mechanical filter is to first design an electrical filter [229]. We use the current-force analogy found in Table 3.1 to convert to the equivalent mechanical filter [230], as shown in Figure 3.17**ab**. One advantage of this method is the possibility to use analytical calculations rather than complex finite-element simulations. The second order low-pass filter response function is calculated using *Qucs* [231]. Our designed

filter has a mass of 2 kg and three springs with a spring constant of 110 $\frac{\mathrm{N}}{\mathrm{m}}$. We find a resonance frequency of 2.05 Hz. The calculated response function is shown in Figure 3.17**c**.

Improving the filter response might be done by adding more mass. Practically, however, the springs should be able to carry the weight of the mass. Asides, adding more mass will only decrease the corner frequency, which in our case will not improve the filter response much as it is already on the order of a few Hz. However, adding a second stage of springs and mass will create a fourth order low-pass filter. This can be designed using the Campbell method [229, 230].

The optomechanical device is mounted vertically on top of the mass and is connected, through thermalized circulators and isolators, with flexible microwave cables. On the mass, a ruthenium oxide *Lake Shore RX-102B-RS* temperature sensor is installed that we can read out with a *Lake Shore 372* AC resistance bridge. The structure is thermalized to the mixing chamber plate with a flexible copper thermal braid. The lower part of the cryostat and device mounted on the mass-spring system are shown in Figure 3.18**ab**. A schematic diagram of the entire measurement setup is presented in Chapter 6.

3.4.2. Wiring and Measurement Setup

When performing experiments in dilution refrigerators there are certain points to take into consideration. Since our devices consist of electromagnetic resonators we will send currents into the cryostat. However, the power supplied can cause a heat load, warming up the system, and is therefore limited. The cooling power of the *Bluefors* system is 12 µW at the 20 mK mixing chamber plate. The specific setup used in each experiment will be discussed in detail in the corresponding chapters. Here, we provide a brief overview of the configurations used.

The optomechanical device is connected to the outside of the cryostat through coaxial cables. The materials used should have a high electric conductivity and low thermal conductivity. For the warmer stages we use stainless steel and for the lower stages superconducting NbTi cables. In order to reduce the power delivered to the device successive attenuators are added to the input line. The output line has a high electron mobility transistor (HEMT) amplifier on the 3 K stage to increase the signal strength. Typically, we install two microwave isolators between the device and the HEMT to ensure no significant Johnson-Nyquist noise can return through the cable and heat our device. Additional microwave components added to the measurement setup are described in the following chapters.

The device used in Chapter 6 includes a flux-tunable qubit, as described in Section 3.1.1. To thread a magnetic field through the SQUID loop, a coil magnet is added to the back side of the flip-chip holder, as shown in Figure 3.18**c**. The coil consists of 650 windings of a copper nickel wire, designed for superconducting switch applications, with a diameter of 140 µm [232]. A DC current can be supplied through a twisted wire pair using a low noise *SRS CS80* voltage controlled current source.

Given the coil radius (8 mm) and length (10 mm) and the distance to the SQUID (13 mm), we estimate to thread 1 Φ_0 though the SQUID with a current of 1.8 mA. This is well below the limit where we would see heating in the cryostat.

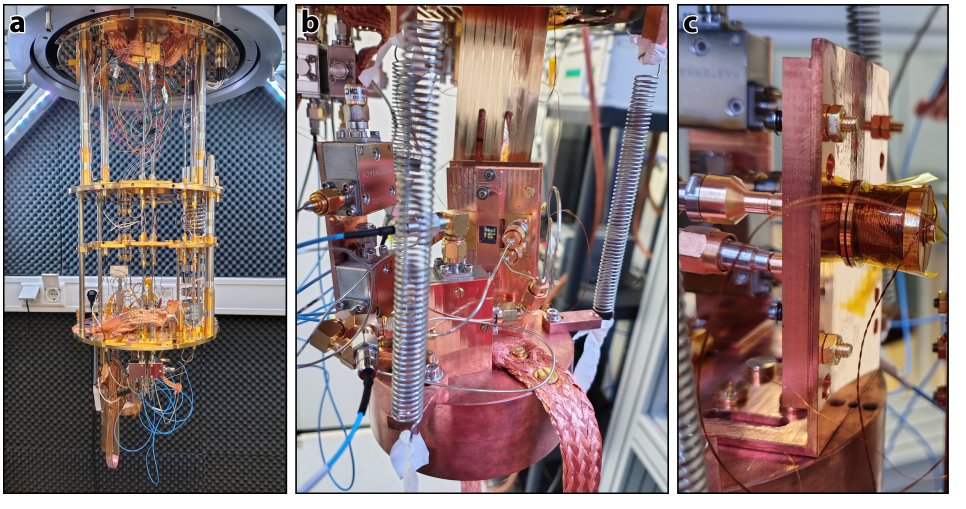


Figure 3.18: Cryogenic hardware for the optomechanical experiment. a Photograph of the bottom half of the *BlueFors* dilution refrigerator without its vacuum and shielding cans. **b** The flip-chip device mounted on the mass-spring system and connected with flexible cables, together with the circulator, isolators, temperature sensor and thermal braid. **c** The superconducting coil magnet mounted at the back of the flip-chip holder.

4

Multitone Microwave Frequency Locking to a Noisy Cavity via Real-Time Feedback

Microwave cavities are commonly used in many experiments, including optomechanics, magnetic field sensing, magnomechanics, and circuit quantum electrodynamics. Noise, such as variations in the magnetic field or mechanical vibrations, can cause fluctuations of the natural frequency of the cavity, creating challenges in operating them in experiments. To overcome these challenges, we demonstrate a dynamic feedback system implemented by the locking of a microwave drive to the noisy cavity. A homodyne-interferometer scheme monitors the cavity resonance fluctuations due to low-frequency noise, which is mitigated by frequency modulating the microwave generator. The feedback has a bandwidth of 400 *Hz, with a reduction of cavity fluctuations by* 85% *integrating up to a bandwidth of* 2 *kHz. Moreover, the cavity resonance frequency fluctuations are reduced by* 73%*. This scheme can be scaled to enable multitone experiments locked to the same feedback signal. As a demonstration, we apply the feedback to an optomechanical experiment and implement a cavity-locked multitone mechanical measurement. As low-frequency cavity frequency noise can be a limiting factor in many experiments, the multitone microwave locking technique presented here is expected to be relevant for a wide range of microwave-cavity experiments.*

This chapter has been published as *Multitone Microwave Frequency Locking to a Noisy Cavity via Real-Time Feedback*, **J.P. van Soest**, C.A. Potts, S. Peiter, A. Sanz Mora, and G.A. Steele, *Phys. Rev. Appl.* **20**, 034007 (2023)

4.1. Introduction

Low-frequency noise is often the limiting factor in mechanical and magnetic experiments [40, 81, 233–239], arising from, e.g., variations in the magnetic field or vibrations in cryogenic experiments. These sources of noise can cause fluctuations in the resonance of a microwave cavity. There are two common ways to counteract this noise: the first is to dampen the noise before it reaches the device under test. While a mass-on-a-spring low-pass filter can suppress high-frequency vibrations for mechanical experiments [229, 240], the lowest frequencies can often introduce considerable noise. In this sense, the mechanical filter is not optimal: it is effective at blocking high frequencies but not low frequencies. The second method actively counters noise by applying dynamic feedback to the system [241, 242]. As a feedback system is limited by its feedback bandwidth and response time, it acts as a high-pass filter: it cannot react at high frequencies but is very effective at low frequencies. Combining these two complementary techniques, therefore, gives an opportunity for noise reduction over the entire spectrum.

In this work, we present an active feedback system based on the cavity-stabilization method introduced by Pound in Ref. [243]. Here, the inverse of the Pound-Drever-Hall technique [244–247] is applied using active feedback to adjust a microwave generator frequency, locking it to a cavity the resonance frequency of which fluctuates in time. This scheme not only locks a single microwave signal to the cavity but also enables the active locking of multiple tones using the same feedback signal, demonstrated in Section 4.5.

Since any source of low-frequency cavity noise can be mitigated, this technique has applications in various fields. It can be used to modulate magnetic flux to stabilize superconducting quantum interference device (SQUID) cavities [80, 242], and magnomechanical experiments [83–86], which are also known to suffer from magnetic field noise. As we demonstrate in Section 4.6, our technique can be directly applied to an optomechanical system experiencing mechanical noise [38]. As identified in previous work, cavity frequency noise from vibrations can be a limiting factor in the ground-state cooling of mechanical resonators [71].

4.2. Experimental Setup

To demonstrate the feedback system, we apply it to a radio frequency (RF) circuit in an optomechanical flip-chip setup, similar to Ref. [67, 72]. The microwave cavity consists of a meander inductor L and a pair of capacitor plates C_0 etched into a NbTiN film, approximately 1 µm above which a mechanically compliant capacitor C_m is positioned. A circuit schematic of the device and optical images are shown in Figure 4.1**a-c**. The top capacitor plate consists of aluminum deposited on a thin silicon nitride membrane, embedded within a patterned silicon substrate etched to form a phononic shield (see, e.g., Ref. [72, 73]). The primary purpose of the phononic crystal structure is to reduce unwanted mechanical noise at 1 MHz and to suppress the radiative loss of mechanical energy through the substrate, as shown in Ref. [71]. However, the phononic crystal has the unwanted side effect of

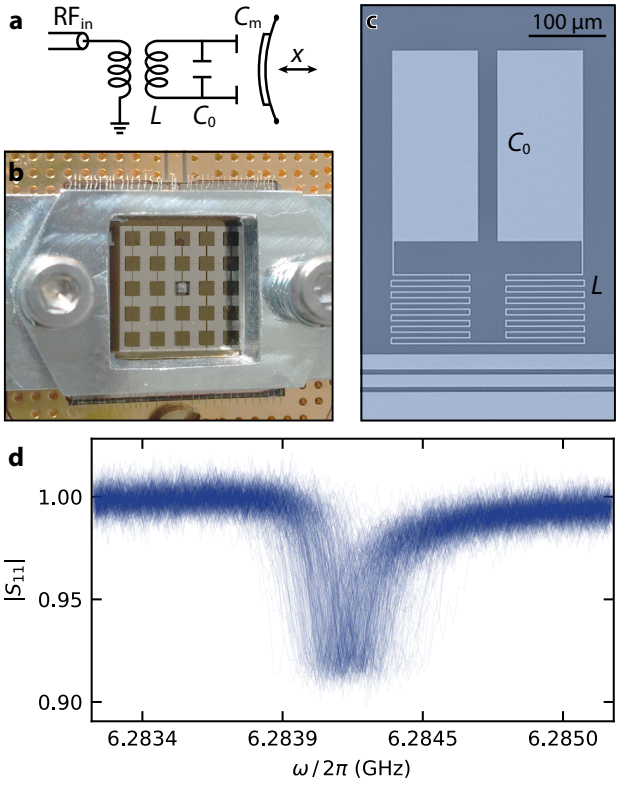


Figure 4.1: A microwave cavity with resonance frequency fluctuations. a A lumped element circuit schematic of the device under test. **b** An optical image of the flip-chip device. The metallized membrane can be seen as a white square in the phononic shield. **c** Optical micrograph of the RF circuit. The meander inductor L and capacitor C_0 form the microwave cavity. **d** 500 individual normalized 240 µs vector network analyzer (VNA) traces show a distribution of the cavity resonance frequency ω_c.

increasing the mechanical susceptibility of the top chip to low-frequency (∼kHz) vibrations in the setup [248].

The resonance frequency of the flip-chip cavity is given by $\omega_c(t) = [L(C_0 + C_m(t))]^{-1/2} \approx 2\pi \times 6.28$ GHz. Vibrations drive low-frequency modes of the top chip, resulting in a time-dependent capacitance $C_m(t)$. Therefore, these low-frequency mechanical vibrations of the top chip modulate the cavity resonance frequency ω_c. The fluctuations in the cavity resonance frequency can be seen in Figure 4.1**d**, where many repeated vector network analyzer (VNA) sweeps demonstrate the noise imparted on the microwave resonator. These measurements have been performed on the base plate of a dilution refrigerator held at approximately ∼20 mK. The pulse-tube cooler is the primary source of vibrations within a dry dilution refrigerator; therefore, the pulse tube was switched off

during measurements to reduce vibrations within the experimental setup. However, we have still observed that the resonance-frequency fluctuations are on the order of the linewidth of the cavity. To compensate for these fluctuations, we have implemented an active feedback system to track the resonance frequency of the cavity.

4.3. Feedback System

To compensate for the fluctuating cavity frequency, we have developed a feedback system similar to the Pound-Drever-Hall technique [244–247]. While the Pound-Drever-Hall technique is usually used to stabilize a noisy laser by locking it to a stable optical cavity, here we apply its inverse role: we lock a stable generator to the resonance frequency of a noisy cavity. In our system, the microwave frequency of the drive tone is locked to the fluctuating resonance frequency of the cavity. Locking the drive tone is accomplished by producing an error signal depending on the time-dependent resonance frequency of the cavity. The error signal is then used in an active feedback loop to frequency modulate the output of the microwave generator, producing a drive tone that tracks the shifting cavity resonance frequency. A schematic diagram of the feedback system is shown in Figure 4.2**a**.

The scheme starts by splitting the local oscillator signal into two paths. One of them goes directly to the microwave cavity and is then directed into the RF port of a mixer. The other path goes through a path-length-matched reference arm to the local-oscillator (LO) port of the same mixer, making the system a balanced homodyne microwave interferometer. Small fluctuations in the resonance frequency of the microwave cavity result in a linear response at the output of the mixer, as seen in Figure 4.2**b**. This downconverted homodyne signal, which we call the homodyne voltage V_h, depends on the detuning of the cavity resonance frequency relative to the current microwave drive frequency. When the system is unlocked, the homodyne voltage fluctuations follow the fluctuations in the resonance frequency of the cavity. In this experiment, the cavity fluctuations are larger than the linear region of the homodyne downconverted signal. Thus, the local oscillator frequency is updated in real time by modulation using a control voltage V_c to track the cavity resonance frequency.

Sweeping the frequency ω_LO of the local oscillator, a linear dependency between the control voltage V_c and the measured homodyne voltage V_h was observed around the cavity resonance, as seen in Figure 4.2**b**. Note that if an unbalanced homodyne detection scheme was used, the pathlength difference would result in phase-winding fringes in the homodyne voltage signal, which could result in a loss of cavity lock. Thus, the use of a balanced homodyne scheme ensures a frequency-independent homodyne voltage signal regardless of the instantaneous local oscillator frequency, see Section 4.8.1.

To maintain constant power arriving at the LO port of the mixer while having dynamic control over the power incident on the microwave resonator under test,

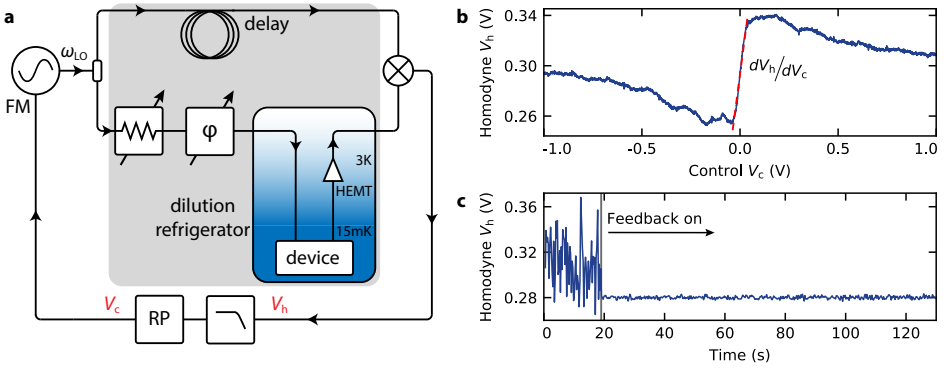


Figure 4.2: The feedback system is used to reduce the cavity resonance frequency fluctuations. a A schematic of the feedback circuit, consisting of a balanced microwave homodyne interferometer, one path of which goes to the device under test. The reference arm is path-length matched, downconverting the signal at a mixer. The resulting voltage V_h is led to a Red Pitaya (RP), which creates a control voltage V_c to frequency modulate (FM) the local oscillator ω_{LO}. **b** The homodyne response as the control voltage V_c sweeps the local oscillator frequency over the cavity resonance. Within the linewidth of the cavity, the response is linear. Low-frequency noise can be seen outside the linear regime. **c** Time trace of the homodyne voltage V_h. The feedback is turned on at $t = 19$ seconds.

a variable attenuator was added to the device arm. Moreover, the phase difference between the local oscillator and device arm was set to 90° out of phase, so that the quadrature signal was measured. The homodyne voltage is then low-pass filtered and led to a proportional-integral (PI) controller programmed in the field-programmable gate array (FPGA) of a Red Pitaya [249]. The output control voltage of the PI controller V_c continuously modulates the frequency ω_{LO} of the local oscillator to remain resonant with the cavity frequency ω_c. Ideally, the homodyne voltage is zero at resonance; however, a slight DC offset was present in the experiment, which determined the set point in the PI controller. To optimize our feedback system, the proportional and integral gain of the PI controller needed to be tuned for optimal noise suppression. As the gain is increased, low-frequency noise is suppressed; however, a too-aggressive PI setting results in added noise at higher frequencies. The optimal value for all experimental implementations of our feedback system depends on the specific configuration; therefore, each system must be calibrated to find the optimal PI gains. Turning on the feedback system stabilizes the homodyne voltage, as can be seen in Figure 4.2**c**. It should be noted that the feedback did not lose the lock during the measurements over a time of approximately 7 minutes (the period that the pulse tube could be turned off).

4.4. Noise Reduction

We can quantitatively analyze the suppressed frequency noise in the reference frame of the cavity by considering the power spectral density of frequency fluc-

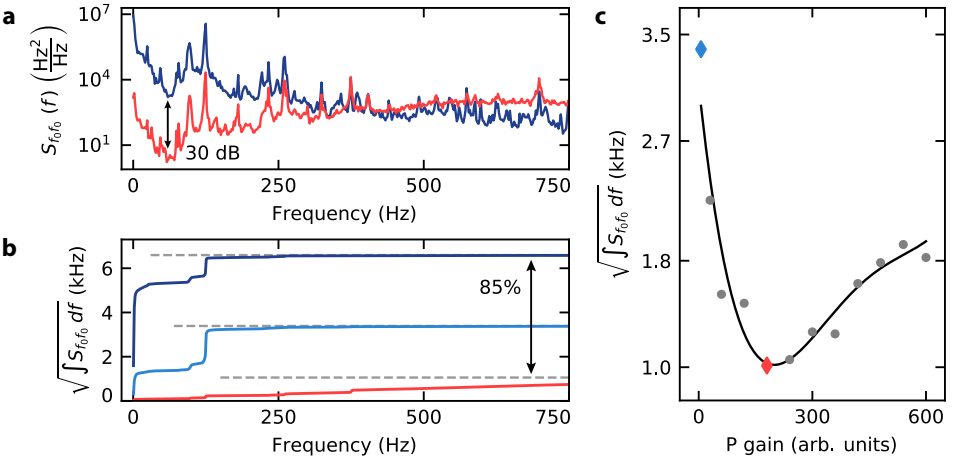


Figure 4.3: Noise reduction of the homodyne voltage V_h depending on the feedback gain. a The power spectral density $S_{f_0 f_0}$ of the homodyne voltage V_h with the feedback off (dark blue) and on (red). The unlocked data has been calibrated as described in Section 4.8.2. Noise is reduced up to 30 dB over a bandwidth of 400 Hz. **b** The integrated power spectral density for an unlocked (dark blue) and a locked cavity for two proportional and integral (PI) gains of the feedback loop (light blue and red). Asymptotes up to 2 kHz (dashed gray) show a noise reduction of 85%. **c** The integrated power spectral density up to 2 kHz for different PI gains of the feedback loop, using the same color coding. The solid black line is a polynomial fit to guide the eye.

tuations $S_{f_0 f_0}(f)$ ($\mathrm{Hz}^2/\mathrm{Hz}$) [248]. The power spectral density can be calculated by taking the Fourier transform of the measured homodyne voltage V_h and is shown in Figure 4.3**a**. The power spectral density of the locked homodyne voltage $S_{V_\mathrm{h} V_\mathrm{h}}(f)$ (V^2/Hz) was calibrated using the slope of the homodyne voltage versus the control voltage, shown in Figure 4.2**b**. However, the power spectral density of the unlocked homodyne signal cannot be calibrated in this way, since the region of linear response is narrower than the fluctuations of the cavity resonance frequency. Therefore, the detected homodyne signal does not contain information about large frequency fluctuations. An extra calibration has been applied to the unlocked spectra, as discussed in Section 4.8.2.

We find that when we turn the feedback on, even with a small gain, the large frequency shifts of the cavity are compensated for and the cavity fluctuations remain within the linear regime of the homodyne signal. This indicates that low-frequency fluctuations dominate the cavity noise. We have identified that for our system, the optimal proportional and integral gain ratio is $\mathrm{P} : \mathrm{I} = 6 : 10$. Figure 4.3**a** shows the power spectral density of the cavity unlocked and locked with the optimal feedback loop gain. It can be seen that for low frequencies, the noise is suppressed up to 30 dB. The spectra cross around 400 Hz, indicating the feedback bandwidth. Above this frequency, the system adds noise to the measurement, due to feedback of the added noise by the amplification chain used. At 2 kHz

and above, the two spectra overlap, suggesting that no additional high-frequency noise is being added by our feedback system. Taking the square root of the integrated power spectral densities, $S_{f_0 f_0}(f)$, we obtain the root-mean-square (rms) value for the noise power, in units of hertz. Even though there is added noise at intermediate frequencies, in Figure 4.3**b** it can be seen that the total frequency noise is reduced. The integrated spectra show a noise reduction of 85% at 2 kHz, as indicated by the asymptotes shown in Figure 4.3**b**. Again, this suggests that low-frequency fluctuations were most detrimental in our system. Since the feedback loop acts as a high-pass filter, these low frequencies are compensated most efficiently.

Finally, the total gain of the feedback loop was varied by increasing the PI gain while keeping their ratio the same. Increasing the gain initially results in additional noise suppression until the feedback increases the total noise power, as shown in Figure 4.3**c**. This provides an optimal feedback loop gain for this system.

4.5. Multitone Locking

Thus far, all measurements have been done using a single tone on cavity resonance. However, many experiments require multiple tones or, in fact, frequency sweeps. Since the local oscillator follows the resonance frequency of the cavity, the feedback circuit can easily be scaled up by adding additional generators to the same feedback setup. For example, an extra stage of up- and down-conversion was added to the circuit, as shown in Figure 4.4**a**. The gray box corresponds with that shown in Figure 4.2**a**. The local oscillator signal is now split into three paths: two paths in parallel are upconverted, to a lock signal $\omega_{\text{lock}} = \omega_{\text{c}} - \omega_{\text{LO}}$ and a probe signal ω_{probe} generated by a VNA; the third path goes to the reference arm as before. The signal coming from the cavity is first downconverted using ω_{LO}, producing two tones at ω_{lock} and ω_{probe}. The signal at ω_{probe} can be measured by the VNA as long as ω_{lock} is not within the intermediate-frequency bandwidth (IFBW) of the measurement. The other path (at ω_{lock}) is downconverted a second time to DC, resulting, as before, in a voltage containing the frequencies of the cavity resonance fluctuations. This signal will also contain fluctuations at the frequency $\delta = \omega_{\text{probe}} - \omega_{\text{lock}}$. If δ is within the feedback bandwidth of the cavity lock, it will need to be filtered out so as not to modulate the local oscillator with this frequency. Again, the downconverted signal is then led to the Red Pitaya to generate an error signal to frequency modulate the local oscillator.

Figure 4.4**b** shows VNA measurements with the feedback off and on, where the same number of traces have been used. Note that these measurements were performed with an IFBW of 600 and 1 kHz, respectively, and with feedback gains P = 480, I = 800. The locked measurement has been performed on the left and right sides of the cavity separately to avoid the lock tone entering the VNA measurement, as discussed above. However, if a measurement requires a VNA sweep on cavity resonance, it is also possible to lock off resonance, see Section 4.8.1.

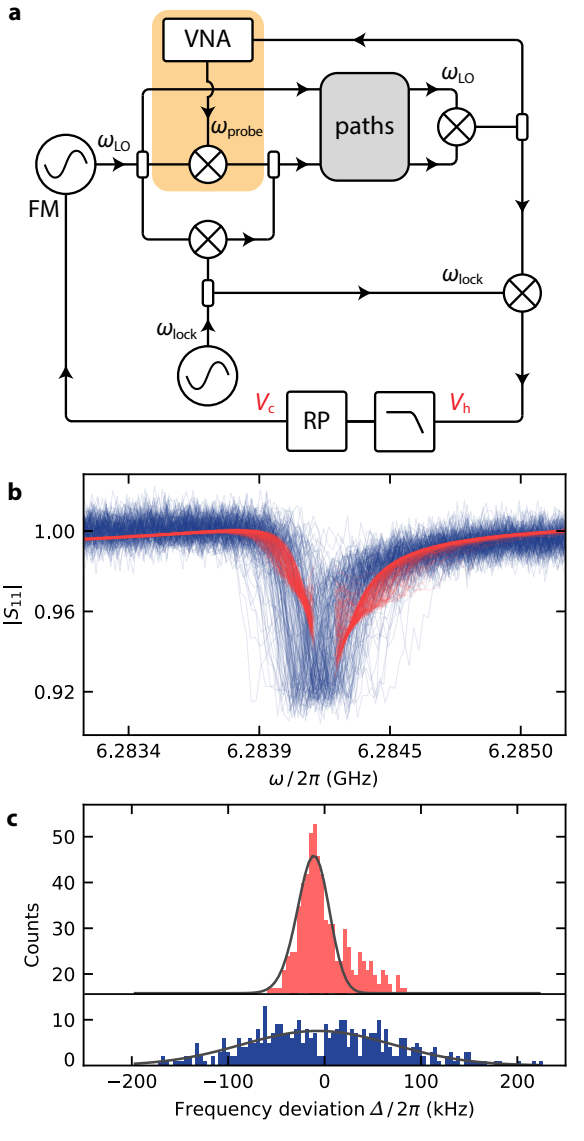


Figure 4.4: Characterization of the locked cavity response measured with the extended feedback circuit. **a** Schematic of the extended feedback circuit to lock multiple signals to the same feedback. The gray box corresponds with that in Figure 4.2. The local oscillator is now up- and downconverted with a lock tone. The components in the orange box are included to add a probe tone to the input of the device. **b** Normalized VNA traces with the cavity unlocked (blue) and locked (red). Two separate measurements are performed for the locked cavity. **c** A histogram of the fit resonance frequency of 376 traces unlocked and locked, using the same color coding. The locked histogram has been shifted for clarity. The standard deviation of the locked cavity resonance frequency is $\sigma_{\text{locked}} = 21$ kHz, which is a factor 4 smaller than the unlocked $\sigma_{\text{unlocked}} = 77$ kHz.

The individual traces have been fit using a Lorentzian function to determine the resonance frequency for each trace. The extracted resonance frequencies of the unlocked and locked traces are compared in Figure 4.4**c**. The left and right data sets are fit separately, using a fixed asymmetry due to the Fano effect [250] extracted from the unlocked measurement. Here Δ is the deviation from the average value of the fit resonance frequency. The fits give skewed Gaussian distributions with a standard deviation $\sigma_{\text{unlocked}} = 77$ kHz and $\sigma_{\text{locked}} = 21$ kHz, which is a decrease of 73% for the locked measurement.

4.6. Optomechanical Experimental Validation

As a demonstration of the applicability of the feedback system, it is used in an optomechanical experiment [38]. The metal film of the capacitor C_{m} is located on a high-tensile stress silicon nitride membrane, parametrically coupling the membrane to the cavity [67]. The membrane is isolated from its surroundings, as it is located in a phononic shield [71]. However, implementing this lattice structure also poses difficulties, as low-frequency modes are excited by vibrations in the dilution refrigerator. Although the energy of these lattice vibrations will mostly not be transferred to the vibrational mode of the membrane, it does mean that the

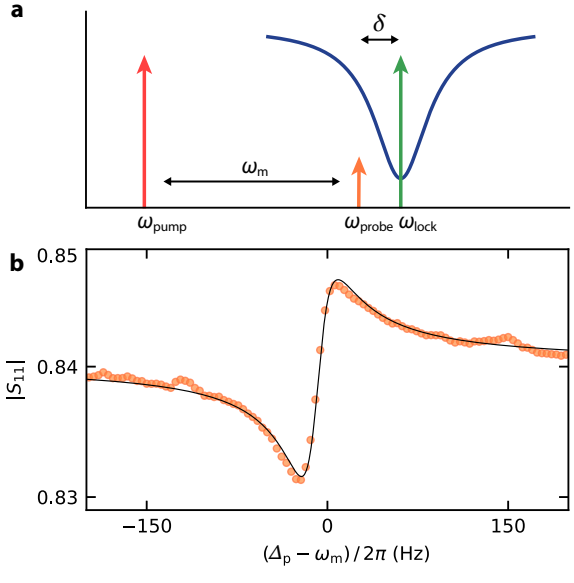


Figure 4.5: Demonstration of a cavity-locked multitone optomechanical measurement. a Illustration of the driving scheme. The upconverted lock tone is set on the cavity resonance. The pump tone is applied ω_{m} away from the center of the probe tone of the VNA, which in turn is detuned by δ from resonance. **b** The mechanical resonance is visible as an optomechanically induced transparency (OMIT) peak, centered around $\Delta_{\text{p}} = \omega_{\text{probe}} - \omega_{\text{pump}}$, when the local oscillator is locked to the cavity, with $\delta \approx 150$ kHz. Normalized data is shown in orange with a fit in black.

membrane is located on a moving structure. As these modes alter the distance between the two chips by an amount larger than the amplitude of the vibrational mode of the membrane, this noise will change C_{m}, and thus also ω_{c}, significantly.

As introduced in Section 4.5, multiple microwave tones can be sent to the device while locked to the same local oscillator. Simply by multiplexing generators and mixers after the local oscillator, more drive frequencies can be added. Repeating the elements inside the orange box in Figure 4.4**a** offers continual scaling.

Figure 4.5**a** shows the scheme for a multitone measurement. By applying a drive tone detuned from the red sideband of the cavity, $\omega_{\mathrm{pump}} = \omega_{\mathrm{c}} - \omega_{\mathrm{m}} - \delta$, and probing close to resonance, $\omega_{\mathrm{probe}} = \omega_{\mathrm{c}} - \delta$, the mechanical resonance appears from optomechanically induced transparency (OMIT) [44, 251, 252]. While having the local oscillator locked, a measurement of the mechanical resonance is presented in Figure 4.5**b**. Note that the asymmetry of the OMIT peak is due to the detuning $\delta \approx 150$ kHz of the pump and probe with respect to the lock tone. However, it is equally possible to instead apply the detuning to the lock tone by adjusting the set point of the feedback circuit, see Section 4.8.1.

4.7. Conclusions

In conclusion, we have presented a dynamic feedback system locking multiple microwave tones to an unstable microwave cavity. The frequency of a local oscillator has been modulated to follow the cavity resonance frequency by calibrating the homodyne signal to a control voltage. The power spectral density of the homodyne voltage has been analyzed, revealing a noise reduction of 85% at 2 kHz. Optimization of the feedback loop and the PI controller has resulted in an optimal response for our system, with a feedback bandwidth of 400 Hz. Furthermore, we have extended the feedback system to enable multitone experiments. Additional microwave tones have been implemented by up-conversion with the same locked tone of the local oscillator. Moreover, VNA measurements probing the cavity have shown that fluctuations in the cavity resonance frequency when locked have a standard deviation of $\sigma_{\mathrm{locked}} = 21$ kHz, as opposed to an unlocked measurement with $\sigma_{\mathrm{unlocked}} = 77$ kHz, which is an improvement of 73%.

Finally, we have demonstrated the applicability of the feedback system by performing an optomechanical experiment. We have observed OMIT using another locked tone from a third generator without losing the cavity lock. Our feedback system provides continual scaling for adding tones to the same lock by multiplexing generators and mixers after the local oscillator. Besides optomechanics [76, 77], the feedback system presented here has applications in various fields, as any source of low-frequency cavity noise can be reduced. For example, other potential applications include reducing two-level system (TLS) noise [78] and locking to coplanar waveguide resonators [79], SQUID cavities [80], gravitational-wave detectors [81], axion dark-matter detectors [82], and magnomechanical experiments [83–86].

4.8. Supplementary Information

4.8.1. Homodyne Phase Matching

It is worth discussing the effect of the balanced interferometer. As mentioned in Section 4.3, the path length of the reference arm of the interferometer is matched to that of the signal arm. In contrast to the most common use of an interferometer, where the absolute phase difference of the two signals is not important, here we need to match the phases exactly. Because the noise in the system causes the resonance frequency of the cavity to fluctuate, our feedback system continually changes the frequency of the drive tone and, thereby, its wavelength. Therefore, the signals arriving at the mixer will have a frequency-dependent phase difference unless the two path lengths are identical.

Figure 4.6 shows the calculated homodyne voltage V_h for a balanced and a $\Delta L = 10$ m unbalanced interferometer. In both cases, the incoming signals are set to be 90° out of phase, to measure the quadrature signal. It is clearly visible that in the unbalanced case, there is a sinusoidal profile superimposing the frequency response of the cavity, known as phase-winding fringes. The linear regime has decreased significantly, increasing the chance for the lock to fringe hop to the next slope. This would result in an unstable feedback signal.

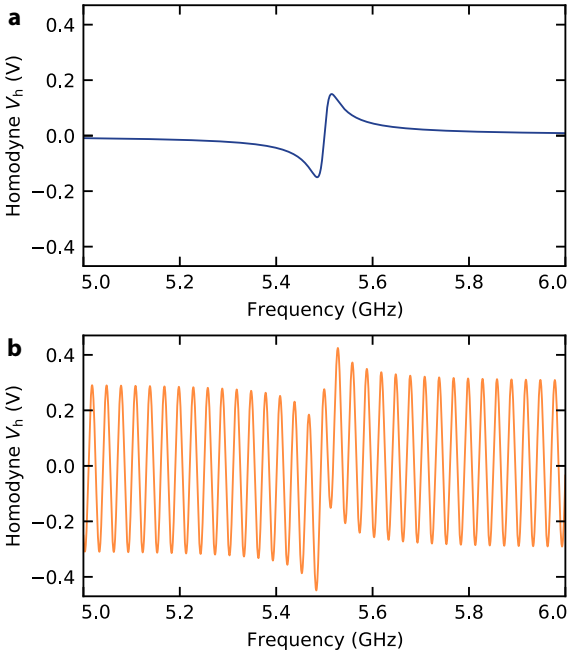


Figure 4.6: The homodyne response for different interferometer path lengths. **a** Calculations for a balanced interferometer. **b** Calculations for an interferometer unbalanced by $\Delta L = 10$ m.

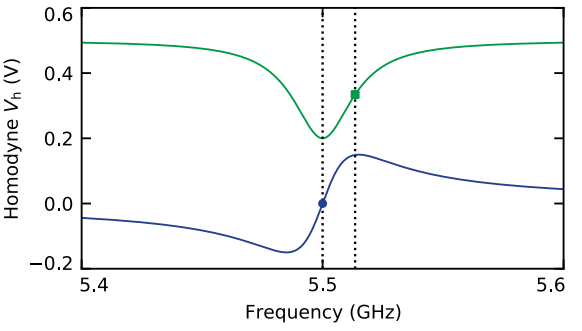


Figure 4.7: The calculated homodyne response for two quadratures, as defined by the phase difference of the two signals coming into the mixer. Locking on resonance can be achieved using the "phase" quadrature (blue), with a tone resonant with the nominal cavity frequency and a feedback setpoint indicated by the blue circle. Locking off resonance can be achieved by choosing the orthogonal "amplitude" quadrature (green) and a setpoint indicated by the green square.

Moreover, it is possible to send the lock tone off resonance from the cavity by adjusting the set point as long as the tone is within the linear regime of the homodyne response. However, one advantage of the homodyne voltage locking, in contrast to the conventional Pound-Drever-Hall technique [244–247], is that one can also choose to lock at other points in the cavity. Doing so will sacrifice some stability, which will reduce the quality of the lock, but choosing the right phase difference at the mixer allows one lock on the other quadrature, as demonstrated in Figure 4.7. The dashed lines show examples of set points that allow locking on and off resonance, while still remaining on an unidirectional slope, using the other quadrature. Note that moving the set point further from resonance can decrease the stability of the lock.

4.8.2. Spectral Density Calibration

The fluctuations of the unlocked-cavity resonance frequency were greater than the region of linear response of the homodyne voltage, as shown in Figure 4.2**b**. As a result, the measured homodyne voltage did contain information about large frequency fluctuations. To compare the unlocked and locked noise spectra, separate calibration measurements had to be performed. With the Red Pitaya, an additional modulation was applied to the local oscillator at different frequencies f_{cal} for both the unlocked and locked cavity. The amplitude of this tone caused a frequency fluctuation of the drive tone that was well within the linear regime of the locked homodyne response and resulted in a sharp peak in the measured power spectral density at the modulation frequency. For the locked cavity, when the frequency of this tone was within the feedback bandwidth, the feedback would create a control voltage to compensate for this artificially added noise. However, for frequencies greater than the feedback bandwidth, the feedback could not compensate this. Therefore, for the tones that were well outside the feedback bandwidth, the integrated area of the calibration tone is equal for the locked and unlocked spec-

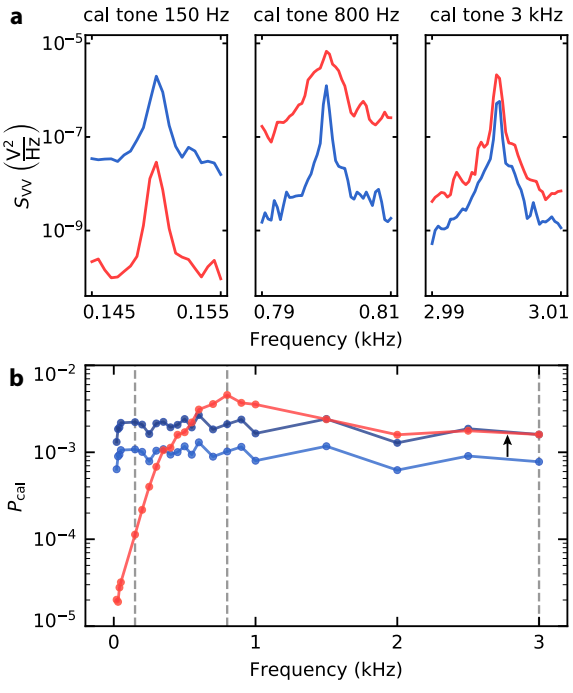


Figure 4.8: Calibration of the unlocked power spectral density. **a** Three measured homodyne power spectral density peaks, produced by an additional modulation tone applied to the local oscillator, for the unlocked (light blue) and locked (red) cavity. The calibration tones have been provided at different frequencies f_{cal} inside and outside the feedback bandwidth. **b** The integrated power P_{cal} of the measured calibration tones, using the same color coding. The dashed lines show the frequencies of the peaks in **a**. The unlocked trace is corrected (dark blue) with an offset of the calibration factor.

tra. By comparing the integrated areas of these measured peaks, we have found that the correction factor scales the unlocked power spectral density accurately. Figure 4.8**a** shows three added modulation peaks of the measured homodyne voltage, both for the unlocked and locked cavity: one within, one just outside, and one well outside the feedback bandwidth. Figure 4.8**b** shows the total measured power P_{cal} of the calibration tones applied. It can be seen that the feedback produces a high-pass filter behavior as expected. For the locked cavity, the powers of the calibration tones well outside the feedback bandwidth show a flat relation, indicating that the feedback did not reduce their noise power. The correction factor was then determined by the difference of the powers at the highest frequency and the corrected unlocked trace was shown. Amending the unlocked data with this calibration has enabled us to compare the unlocked and locked measurements fairly.

5

Subtleties in Optomechanical Sideband Cooling and Calibration of a Mechanical Resonator

We present a large high-stress membrane optomechanically coupled to a two-dimensional superconducting microwave cavity in a flip-chip geometry. The membrane, located in an in-substrate phononic shield, is measured to have a quality factor of $Q_m = 2.62 \cdot 10^7$*. Spectroscopy of the motional sideband is performed to measure the thermal noise of the mechanical mode. We introduce a multi-tone sideband cooling scheme to enhance the signal of the mechanical noise. The mechanical mode is cooled, with the voltage power spectral density signal reduced to* 1.4% *of its thermalized value. We highlight the subtleties and assumptions necessary for the calibration of the mechanical mode temperature and discuss a general calibration procedure.*

J.P. van Soest, C.A. Potts, S. Peiter, A. Sanz Mora, and G.A. Steele, *Subtleties in Optomechanical Sideband Cooling and Calibration of a Mechanical Resonator*, *in preparation* (2025)

5.1. Introduction

Over the last two decades optomechanical systems have emerged as a leading platform for detecting and controlling mechanical motion. Specifically, inside a cavity the light field can be focused to optimize its radiation pressure on a mechanical resonator. At the core of these systems lies this parametric interaction between the phonons and photons. A huge variety in system size exists, with mechanical resonators with a mass from zg to kg, and cavities ranging from nm to km in size [18–20]. Utilizing each system's advantages has allowed for major scientific breakthroughs over the years. Some examples of accomplishments in optomechanical systems are displacement detection below the standard quantum limit [43, 253], sideband cooling a mechanical mode to the ground state [36, 37, 67, 72, 254, 255], generation of non-classical states of motion by squeezing [45, 46], microwave to optical photon transduction [51, 256], entanglement in mechanical oscillators [47], and gravitational wave detection [20, 35].

Moreover, these kind of systems are a promising platform that could answer the fundamental open question of what would happen in a massive quantum system. Concretely, the optomechanical interaction could be used to prepare Schrödinger cat or Fock states of motion to test quantum collapse and quantum gravity models. For this, one needs to be able to bring an experiment into a regime where both quantum and gravitational effects take place to a significant extent [52–54]. There are generally two approaches aimed at reaching this goal. One could start with a gravitational experiment and reduce the size to create quantum mechanical states in the masses [55–58]. Or one could start with a quantum experiment and enlarge the system size by increasing the mass [59–63, 88].

An example for the latter method is the application of the flip-chip technique [48, 51, 57, 64–75, 128, 144, 221–226]. Here, a high-stress membrane is flipped on top of an optical or microwave cavity. The mechanical motion is parametrically coupled to the cavity, which is dependent on the distance between the two chips $g_0 \propto d^{-3/2}$, as treated in Chapter 2. Other benefits of this technique lie in the properties of the membrane. The mechanical resonance mode can have a large effective mass while retaining a considerable zero-point fluctuation. Heavy resonators tend to have lower eigenfrequencies. However, those of ~ 100 µm-size silicon nitride membranes can be larger than the linewidth of microwave cavities, resulting in optomechanical systems in the sideband-resolved regime.

All these experiments rely on careful calibrations [118, 257–260]. For example, a mechanical mode's occupation can be detected by measuring its noise spectrum via an optomechanical experiment. Whether an optical or microwave light field is used, the measured quantity is usually a voltage. It is therefore important to reliably convert the voltage power spectral density to a displacement [40, 261–263]. This, however, is not a trivial task, as both the power arriving in the cavity and the ultimately measured voltage could be influenced by unknown temperature dependencies in the measurement setup. Furthermore, signals sent to the device can generate heating, creating an elevated effective bath temperature.

Here, we present an electromechanical flip-chip device using mechanical clamping. This method alleviates most of the technical challenges, such as the feasibility of assembly and potential breaking of the membrane during a cooldown to cryogenic temperatures. A large high-tensile stress silicon nitride membrane is coupled to a superconducting lumped element microwave cavity. Installed on a vibration isolation system, we bring the system into the good-cavity limit. Using optomechanically induced transparency (OMIT), we characterize the fundamental mode of the membrane. A detailed discussion is presented on the thermal calibration techniques commonly applied in noise measurements. We emphasize certain necessary subtleties and assumptions for quantitative detection of the mechanical displacement. Finally, we introduce a multitone sideband cooling scheme to enhance the signal of the mechanical noise while cooling the mechanical mode.

5.2. Experimental Setup

We use the same optomechanical device as was used for the demonstration of the frequency locking in the previous chapter and will now focus on optomechanical experiments possible with this device. The sample is built up from two chips clamped in a flip-chip holder. The top chip contains a $350\,\mu m \times 350\,\mu m \times 50\,nm$ high-tensile stress (0.95 GPa) silicon nitride membrane, fabricated by Norcada [217]. The membrane is metallized with a sputtered aluminum +1% silicon $300\,\mu m \times 300\,\mu m \times 25\,nm$ square. A substantial additional fabrication step was the etching of the phononic shield. The phononic shield is designed to have a phononic bandgap around the frequency of the fundamental mode of the membrane. The membrane is located within the middle pad of the phononic shield, which has two functionalities. First, it isolates the membrane mode from its surroundings, making it less susceptible for vibrations of the dilution refrigerator. Second, as the membrane is soft clamped, the energy of the mode will be dissipated less efficiently into its surroundings. These two processes can increase the quality factor of the membrane by a factor 100 [71]. The bottom chip contains a lumped element microwave cavity side-coupled to a coplanar waveguide reflection line, etched into 100 nm thick NbTiN. The cavity design is shown in Section 5.7.2.

The flip-chip assembly is performed as follows. One strategically placed droplet of glue is used to secure the bottom chip into the PCB. Then, the top chip is flipped on top of the bottom chip and, using an aluminum xy-holder, aligned with the cavity. The z-pusher is placed on top of the outer frame of the top chip and pressed down hard with spring-loaded screws. This reduces the gap and brings the chips together as close as possible with this equipment. Photographs of the assembled device and the flipped membrane are shown in 5.1**ab**. Reducing the gap between the metallized membrane and the capacitor pads of the cavity creates an additional capacitance, and thus reduces the cavity frequency to 6.5658 GHz. The movement of the membrane changes the capacitance to the cavity, which creates the parametric coupling between the mechanical and microwave modes. A circuit diagram of the circuit is shown in Figure 5.1**c**.

In this work, we have mounted the device in a dilution refrigerator designed to have less vibrations, as the pulse tube cooler has been mounted detached from the vacuum can. Additionally, the device is installed on a mass-spring system, designed to act as a mechanical low-pass filter, as described in Chapter 3. The system is thermally linked to the mixing chamber plate of the cryostat and cooled down to $T \approx 20$ mK. More detailed information on the measurement setup is given in Section 5.7.1. This device mounting promises lower vibrational noise, and thus less frequency fluctuations in our microwave cavity.

Figure 5.1**d** shows the trace-averaged S_{11} magnitude (blue) and phase (orange) response when applying single-tone spectroscopy on the cavity. Individual fast measurements show the cavity frequency fluctuation on the order of a linewidth, as shown in Section 5.7.2. Here, we present the average response of 500 traces. A Lorentzian fit gives a linewidth of $\kappa_{tot} = 2\pi \cdot 243\,\text{kHz}$ and quality factor $Q_c = 2.7 \cdot 10^4$.

5.3. Dynamical Backaction

As a first characterization of the mechanical resonator we employ a technique known as optomechanically induced transparency [251, 252, 264]. A strong coherent microwave tone is sent to the cavity with a detuning equal to the mechanical resonance frequency $\omega_d = \omega_c - \Omega_m$. A second weak probe tone is swept over the cavity resonance. The two tones interfere with each other, creating an amplitude beating at the difference frequency. When the beating frequency is equal to the mechanical resonance frequency it exercises a radiation pressure force on the membrane that is resonant with the mechanical mode. This drives the membrane and, in turn, modulates the cavity resonance. Sidebands of the mechanical mode are generated, of which the upper sideband lies inside the cavity resonance. There, it destructively interferes with the probe field and creates a transparency window inside the cavity resonance. The drive tone at the red sideband creates dynamical backaction, which increases the mechanical damping rate $\Gamma_{eff} = \Gamma_m + \Gamma_{OM}$, where Γ_m is the intrinsic mechanical damping rate and Γ_{OM} the optomechanically induced damping rate. Γ_{eff} is the width of the transparency window. The height of the window inside the cavity is given by $|S_{11}(\omega_c)| = \left|1 - \frac{2\eta}{1+\mathcal{C}}\right|$, where $\eta = \frac{\kappa_{ex}}{\kappa_{tot}}$ and the cooperativity $\mathcal{C} = \frac{4g^2}{\Gamma_m \kappa_{tot}}$. The multiphoton coupling rate $g = g_0\sqrt{n_c}$ is dependent on the intracavity photon number n_c. The optomechanical coupling corresponds to changing the intrinsic cavity damping rate as $\kappa_{int} \to \kappa_{int} + \frac{4g^2}{\Gamma_m}$ [265].

In Figure 5.2**ab** we show the OMIT response for two drive powers at the red sideband. A probe tone of 0 dBm at the generator output is used and the pump is varied from −12 to 24.5 dBm. The drive tone was set $2\pi \cdot -0.958241$ MHz detuned from the cavity resonance. From the OMIT peak we calculate the mechanical resonance frequency of $\Omega_m = 2\pi \cdot 0.978665$ MHz. We conclude that the vibrational noise has been sufficiently suppressed for the optomechanical cavity to be sideband-

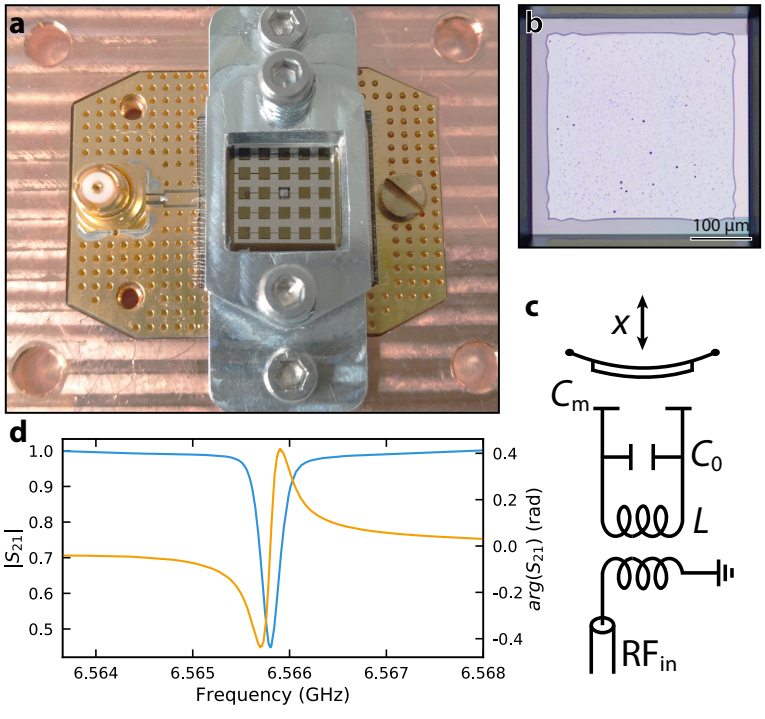


Figure 5.1: A cryogenic optomechanical flip-chip device. **a** Photograph of the assembled flip-chip device clamped with spring-loaded screws. The metallized membrane can be seen as a white square. The phononic shield is the brown lattice structure. **b** Optical micrograph through the membrane. The sputtered metal square is visible as a gray square aligned above the white cavity seen on the right-hand side. **c** Schematic representation of the optomechanical circuit. Panel **d** shows the magnitude normalized to unity (blue) and phase (orange) S_{11} of the cavity response in a spectroscopy measurement, averaged over 500 traces.

resolved $\Omega_m \gg \kappa$. At the lowest power used we can still resolve the OMIT peak. Performing Lorentzian fits gives us the effective linewidth of the mechanics. Figure 5.2**c** shows the power dependence of the OMIT peak. However, the frequency resolution of the VNA measurement limits the minimum linewidth for which we are able to resolve the OMIT peak. A linear fit is performed over the data points up to 63 mW (18 dBm). We extrapolate to a drive power of 0 mW to find an upper bound for the intrinsic mechanical damping rate $\Gamma_m \leq 2\pi \cdot 122$ mHz. From this, we calculate an underestimation of the mechanical quality factor of $Q_m \geq 8.00 \cdot 10^6$. At higher drive powers the linewidth increases at a slightly lower rate, deviating from the linear trend. This could be due to the cavity noise present. The largest linewidth we obtain is $2\pi \cdot 37.3$ Hz, which corresponds to the lower bounds for the cooperativity $\mathcal{C} \geq 304$ and multiphoton coupling rate of $g \geq 2\pi \cdot 1.5$ kHz. See Section 5.7.3 for detailed information on the data analysis.

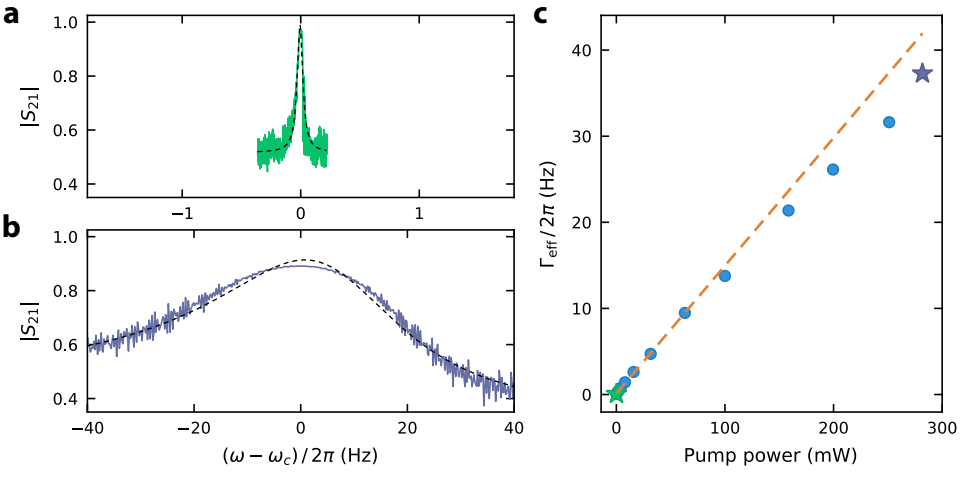


Figure 5.2: Observation of OMIT power dependence. Panel **a** shows the magnitude $|S_{11}|$ of the narrowest OMIT peak that could be resolved. As the red sideband drive power increases the peak broadens, resulting in a linewidth of $\Gamma_{\text{eff}} = 2\pi \cdot 37.3$ Hz, as shown in panel **b**. Lorentzian fits are shown as black dashed lines. **c** OMIT power dependence with the narrowest and widest peaks color coded as the other panels. A linear fit (orange dashed line) is performed for data points up to a drive power of 63 mW. Extrapolation of the fit gives us the overestimation of $\Gamma_m \leq 2\pi \cdot 122$ mHz.

5.4. Thermal Calibration of the Mechanical Mode

In order to learn more about the mechanical motion we can perform noise measurements and analyze the coupling of the mode to bath temperature. For optomechanical systems, to quantify the energy or displacement of the mechanical resonator, it is necessary to calibrate the measured signal. One way to do this is with a thermal calibration. Here, we will take a careful look at the requirements and necessary assumptions for this technique.

We send a microwave signal to the cavity resonance and measure a time-domain voltage signal with a spectrum analyzer. The photons in the cavity will undergo Stokes and anti-Stokes scattering, which in the ideal symmetric case will not cause heating or cooling of the mechanical mode. However, the device suffers from cavity resonance frequency fluctuations, as discussed in Section 5.7.2, and as a result, on short time scales the system is not symmetric with respect to the drive. With the risk that the tone becomes slightly blue-detuned, it could heat the mechanical mode or even drive the system into instability. To avoid this, we set the microwave tone $2\pi \cdot -85.7$ kHz red-detuned from the average cavity resonance frequency $(\omega_c - \delta)$, while still within the cavity linewidth. Due to its small detuning, this tone provides only a small additional cooling factor that reduces the initial occupation by 6.4%, based on an additional optical damping of $\Gamma_{OM}^{\delta} = 2\pi \cdot 2.54$ mHz, see Section 5.10.

We first perform a heterodyne downconversion of the signal returning from the cryostat with a frequency close to the red sideband minus the detuning $(\omega_c - \Omega_m - \delta)$ and measure with a bandwidth and total time sufficient to both resolve the narrow peak and enclose more than its FWHM: $\delta f \ll \Gamma_{eff} \ll f_{span}$. This way we can record the two quadratures of the signal at the frequency of the mechanical mode. Here we have to note that, in order to get sufficient signal to noise and frequency resolution for all noise measurements in this chapter, the measurements were taken over an extended period of time with a duty cycle. The incoherent property of thermal noise allows for concatenating the individual time traces. This also ensures the low temperature of the device, as for the measurements discussed in Section 5.5 high pump powers were used, which can dissipate small amounts of energy over time. Performing a complex fast Fourier transform (FFT) on the IQ time trace results in the voltage power spectral density (PSD) consisting of two additional parts $S_{VV} = S^m_{VV} + S^{imp}_{VV}$. The small IFWB helps to exclude other noise sources, such as technical measurement noise [258]. The Lorentzian-shaped peak S^m_{VV} is the noise contribution for the thermal motion of the mechanical resonator, and the flat noise floor is the voltage imprecision S^{imp}_{vv}. We perform a Lorentzian fit op top of a flat background on the total PSD and integrate the Lorentzian contribution of the noise spectrum. To ensure we are not underestimating the noise power originating from the mechanical resonator, we ascertain the noise floor does not increase [262]. The fitting routine and analysis is described in more detail in Section 5.10.

To calibrate the noise measurements, we want to relate the measured voltage PSD $S_{VV}\left(\frac{V^2}{Hz}\right)$ to a position PSD $S_{xx}\left(\frac{m^2}{Hz}\right)$. For this we cannot look at our cavity at these temperatures, since due to its high frequency, its thermal population is below one, as $\hbar\omega_c = k_B T$. Therefore, our microwave cavity is in its ground state. The mechanical resonator has a much lower frequency and thus has a thermal population. In practice, its mode temperature is always greater than the bath temperature. One method to calibrate our measurement is to perform a thermal calibration of the mechanical motion. For this, we stabilize the bath temperature by raising the temperature of the refrigerator, such that the mechanical mode becomes thermalized.

Figure 5.3 shows the integrated voltage power spectral density of the mechanical motion for ten different cryostat temperatures, as measured by the sensor on the mixing chamber plate. After changing the cryostat temperature we perform repeated noise measurements until we observe that the temperature of the copper mass and the device has stabilized. We first raise the mixing chamber plate to the highest temperature of 400 mK with a PID-loop controlled heater. Importantly, here we assume that the mechanical mode is thermalized to the bath and invoke the equipartition theorem $k_B T_m = \hbar\Omega_m$. Now, the integrated area under the peak is proportional to the temperature of this mode [38, 259].

$$\int S_{VV}(\omega)\, d\omega \propto \frac{k_B T_m}{\Omega_m^2 m_{eff}} = n_m \tag{5.1}$$

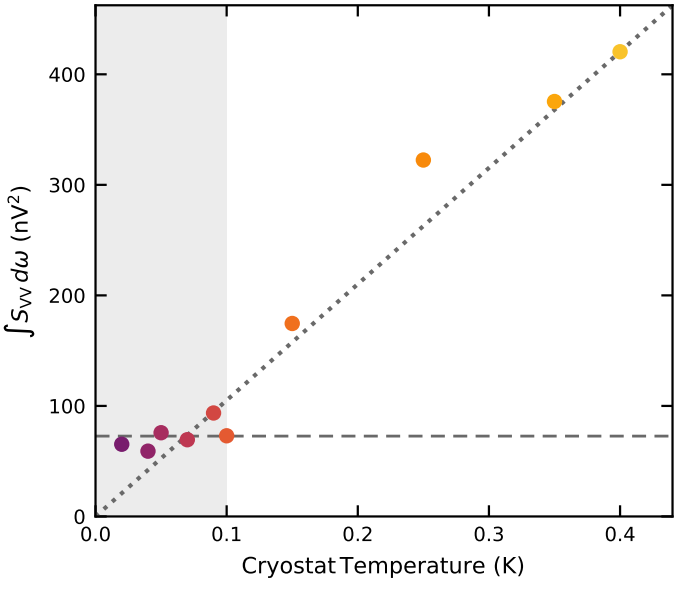


Figure 5.3: Thermal calibration of the mechanical mode. Integrated voltage power spectral density of the mechanical noise for different temperatures of the dilution refrigerator. With decreasing temperature a linear trend towards 0 can be seen, indicated by the gray dotted guide to the eye. Below a cryostat temperature of 100 mK, indicated by the gray shaded region, the integrated PSD settles to 73 nV^2 (gray dashed line).

As we decrease the cryostat temperature, the integral of the PSD decreases linearly towards 0, as indicated by the dotted line. This implies that the mechanical mode is thermalized for these temperatures and that our initial assumption is correct. The corresponding measured spectra are shown in Section 5.7.4. When we reach a temperature of 100 mK we see the integral leveling off to a value of 73 nV^2, indicated by the gray dashed line. As the bath temperature decreases, the mechanical resonator excitation does not change any more. Therefore, we could assume that our mechanical mode thermalizes to 100 mK, which would correspond to an occupation of $n_i = \frac{k_B T_m}{\hbar \Omega_m} \approx 2174$ phonons. However, it is important to note that in order to be able to make this claim more assumptions have to be made, which we will now outline.

One of these assumptions is that the Stokes scattering of photons from the cavity resonance to the red sideband is constant with temperature. This is the case when the intracavity photon number is constant. However, we see a change in decay rates of the cavity κ_{in} and κ_{ex}. This could be caused by a change in cavity frequency fluctuations over time and does not show a clear relation with temperature. This results in a small change in height of the measured noise peak, creating uncertainty in the integrated area. The measured cavity lineshapes and

the quantitative implications are further discussed in Section 5.7.4. To improve the stability of the cavity, and thereby the consistency of the observed mechanical noise, one could mechanically isolate the device more, or apply a feedback scheme as described in Chapter 4.

There is also the implicit assumption that the power arriving at the device is independent of temperature. For this, we have performed a set of spectroscopy measurements at every temperature. However, we observe that the background of the VNA measurements around the cavity changes by 2 dB. A careful investigation showed that the transmission of our flexible cable (both the attenuation and the impedance) changes with the temperature of the cryostat. This effect will also result in a change in the measured voltage power spectral density noise peak, as the intracavity photon number and Stokes scattering rate get modified. In Section 5.7.4 we discuss the influence of this discrepancy in more detail. It is interesting to note that we have performed four thermal cycles with different flexible microwave cables, in all of which we observed a temperature dependence of the transmission at mK temperatures. To prevent the uncertainty in power arriving at the device one could carefully calibrate the setup, including the cables and microwave components, for the temperatures used.

5.5. Cooling the Mechanical Mode

Next, the mechanical resonator was cooled with an optomechanical sideband drive. We performed PSD measurements to see how the noise power of the mechanical mode scales when we increase the red sideband drive power. This will tell us two things. First, it is an independent measurement of the cooling of the mechanical mode, as the area under the peak decreases with the membrane displacement and thereby its phonon occupation. Second, we use these measurement to check that the noise floor does not increase, indicating that we are not reaching the limit where phase noise of the microwave generator will cause heating of the membrane [36]. To ensure we can compare and interpret the results of different sideband cooling noise measurements fairly, the microwave power arriving in the cavity needs to be constant over time. As in the previous section, we will test this assumption. Over the duration of all sideband cooling measurements we performed single-tone spectroscopy measurements around the cavity to confirm the stability of the cavity decay rates κ_{in}, κ_{ex} and the background level. Additionally, we performed a single-tone power sweep over the cavity to ensure the stability of these parameters with intracavity photon number. We will now first look at the results of the sideband cooling experiments, after which we will discuss these results in relation to the dynamical backaction observed in Section 5.3 and the calibration in Section 5.4.

Just as for the dynamical backaction measurements, we apply a drive tone on the red sideband of the cavity to cool the mechanical mode. As with OMIT, this generates photons at the cavity resonance, which could be measured with the spectrum analyzer [23, 24, 36, 266, 267]. However, due to the narrow mechanical linewidth and the optomechanical coupling in our system, the signal to

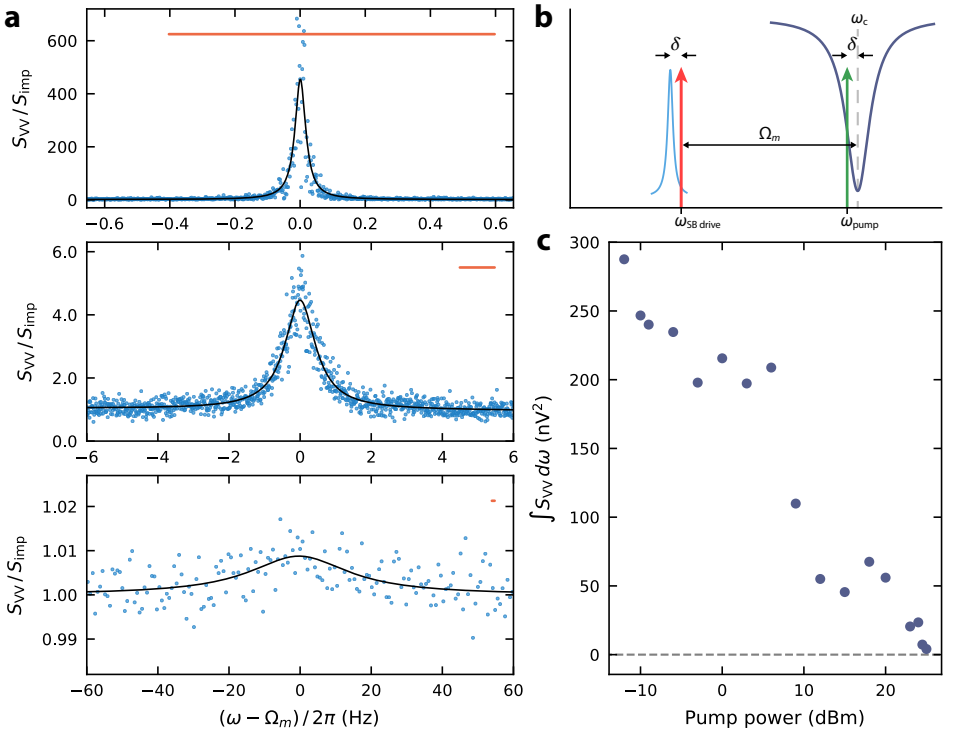


Figure 5.4: Cooling the mechanical mode. Panel **a** shows the downconverted voltage power spectral density of mechanical noise, normalized to the noise floor. Top to bottom are for a red sideband drive power of −12, 9 and 25 dBm. Blue circles are bin-averaged data, black lines are fits. As the pump power increases, the mechanical noise peak lowers and widens, and the SNR decreases. The red scale bars represent a span of 1 Hz. **b** Schematic multitone measurement scheme. Applying the δ-detuned pump tone enhances the mechanical noise signal at an equal detuning from the red sideband drive. Panel **c** shows the integrated voltage power spectral density of the thermal Lorentzian contribution. As the pump power increases, the integrated motion decreases to 1.4% of its original value.

noise ratio (SNR) for this measurement is too small to observe the noise peak. Since sending a tone at $\omega_c - \delta$ gives us a peak with good SNR at the detuned sideband at $\omega_c - \Omega_m - \delta$ that is related to the mechanical occupation, we use a two-tone scheme, as depicted in Figure 5.4**b**. We ensure that the detuning δ does not cause the first tone to overlap with the red sideband drive. As the drive power at the sideband increases, the mechanical noise peak will lower and widen. In order to capture more than the FWHM of the peak the IFBW, which here is the measurement bandwidth, is varied from 80 to 500 Hz for different drive powers.

Figure 5.4**a** shows the voltage power spectral density of mechanical noise, normalized to the noise floor. The peak is shown for three different red sideband

drive powers of −12, 9 and 25 dBm, as set by the generator. In order to be able to resolve the peak over the imprecision noise, the traces are taken for different durations. For the lowest drive power the measurement took place over 30 minutes and the data is bin-averaged 3 times. For the highest power we measured for 24 hours. Here, the data is bin-averaged 60,000 times. For these measurements the SNR of the mechanical noise got reduced from 454 to 1.00877. From the fits we extract an average noise floor of $S_{VV}^{imp} = 21.8\,\frac{\mathrm{nV}^2}{\mathrm{Hz}}$ and verify it does not increase with drive power. Therefore, we can treat the Lorentzian noise contribution as solely coming from the motion of the membrane. Figure 5.4**c** shows the integrated voltage power spectral density of the mechanical motion. As the pump power increases, the integral diminishes to 1.4% of its original value where the mechanical mode is thermalized. All datasets and their analysis are shown in Section 5.10.

Correcting for the additional cooling rate from the first drive tone, we find a mechanical damping rate of $\Gamma_m = 2\pi \cdot 37.3$ mHz. This corresponds to a mechanical quality factor of $Q_m = 2.62 \cdot 10^7$. The largest linewidth we obtain is $\Gamma_{eff} = 2\pi \cdot 49.3$ Hz. From this, we obtain a cooperativity $\mathcal{C} = 1322$ and optomechanical coupling rate $g = 2\pi \cdot 1.73$ kHz. These results rely on the aforementioned assumptions. As discussed in the previous section, we cannot reliably convert S_{VV} to S_{xx} and derive the mechanical mode temperature. However, since we are permitted to compare the cooling data, the relative cooling of the mechanics we can extract. With the thermal calibration the integrated voltage PSD was observed to level off, indicating an initial mode temperature and occupation of 100 mK and $n_i \approx 2174$ phonons. Using this temperature and the found cooperativity we obtain a coarse estimate of the final mechanical occupation of $n_f \approx 1.64$ phonons. A full calibration of the measurement setup and a reduction of the cavity noise would allow for an exact measurement of the final phonon occupation.

5.6. Conclusion & Discussion

We presented a flip-chip platform used for the implementation of cavity optomechanical coupling to a high-Q mechanical mode in a silicon nitride membrane. Microwave cavity frequency fluctuations caused by vibrations in the measurement setup, which were previously detrimental for sensitive measurements, have been mitigated. Sending a strong microwave tone to the red sideband of the cavity OMIT was observed. Noise measurements where performed on the thermal occupation of the membrane mode. A multitone driving scheme was introduced to enhance the signal to noise ratio. The intrinsic mechanical linewidth was found to be $\Gamma_m = 2\pi \cdot 37.3$ mHz, yielding a quality factor of $Q_m = 2.62 \cdot 10^7$. Furthermore, many subtleties and necessary assumptions were discussed on the calibration of the mechanical occupation and the conversion of the measured voltage power spectral density to a displacement of the resonator. This sheds light on a general calibration procedure, as many of these details are often not fully discussed in literature. Finally, we performed sideband cooling of the membrane mode close to the ground state, reducing the measured signal to 1.4% of its thermalized value. With these

measurements a cooperativity of $\mathcal{C} = 1322$ and optomechanical coupling rate of $g = 2\pi \cdot 1.73$ kHz were obtained.

One limiting factor in these experiments was the temperature dependence of the attenuation and impedance of our flexible microwave cable. Improving or carefully calibrating these properties would allow for an exact calibration of the mechanical occupancy. A second limitation was the cavity noise our system suffered from. One method to reduce this is by improving the vibration isolation. This can be done by adding stages to the mass-spring system, mounting the device on an elastic pendulum, or possibly by orienting the device vertically, orthogonal to the majority of the vibrations in the cryostat [229, 240, 268]. This method can be combined with the dynamic frequency locking via a frequency modulation technique to reduce the residual low frequency noise, as discussed in Chapter 4. With these modifications we expect to be able to prepare and detect the ground state of motion of the membrane, as we did not yet reach the backaction limit. This would be a milestone in the path of creating of a platform to investigate massive superpositions to investigate gravitational effects on quantum systems [61–63, 88, 269].

Another approach would be by taking advantage of the nonlinearity of the microwave cavity. For example, frequency locking of a microwave cavity has been achieved using a red-detuned tone. The cavity was observed to transition to signal and idler modes with narrow linewidths, which were used to interact with the mechanics [95, 97, 270, 271]. Various parameter regimes exist, defined by the magnitude of the nonlinearity and application of microwave drives. Some of these can lead to amplification, resulting in a net gain of the converted signal from the mechanics, increasing signal to noise. Recently, the Kerr nonlinearity has also been used to enhance cooling of a mechanical mode in a non sideband-resolved magnetomechanical system [98–102]. Moreover, an improved cooling performance was observed in an electromechanical device in the good-cavity limit [97, 100]. Despite these impressive results, in the field of nonlinear optomechanical systems there is still significant potential for new experiments.

5.6.1. Contributions

S.P. designed and fabricated the device. S.P. and A.S.M. performed the initial characterization of device. J.P.S. conducted the measurements. J.P.S. and C.A.P. performed the data analysis. J.P.S. wrote the chapter with input from C.A.P. and G.A.S. G.A.S. supervised the project.

5.7. Supplementary Information

5.7.1. Measurement Setup

All experiments in this chapter were performed in a dilution refrigerator at base temperature ($T_{base} \approx 20$ mK). The flip-chip device, whose fabrication is described in Ref. [71], is mounted on a mass-spring system hanging below the mixing chamber plate. A schematic of the measurement setup is shown in Figure 5.5. The copper cylindrical mass is thermalized to the base plate through a flexible copper braid. Two coaxial microwave lines are used for the in- and output connection of the device. At room temperature, DC blocks are placed on both lines to isolate the system from DC currents and to prevent ground loops. The input line is attenuated at each stage, to block thermal radiation of the line from reaching the device. A total of 43 dB of attenuation was used, on top of the attenuation from the coaxial cables themselves. Because we measure the cavity in a side-coupled reflection geometry, we use a circulator to direct the in- and output signal from the device. From the circulator mounted below the base plate a flexible coaxial cable is connected to the PCB. Multiple cooldowns were performed with various flexible cables to improve the line's dependency on temperature and the vibration isolation simultaneously. A high-electron-mobility transistor (HEMT) amplifier with a gain of 44 dB and bandwidth of $4 - 8$ GHz was placed on the output line at the 3 K stage. Two isolators where installed between the circulator and the HEMT to block the thermal radiation of the amplifier from reaching the device.

Outside the cryostat a single measurement setup is used for all experiments. The probe signal is sent to the device from a vector network analyzer (VNA), attached through the -10 dB port of a directional coupler. Two microwave generators are connected to the input as well, one through a -10 dB port of a second directional coupler and one directly. These are used to send the coherent pump signals for the optomechanical interaction. On the output line, the signal first goes through a room temperature amplifier, after which it is split by a -20 dB directional coupler to the VNA, and to a spectrum analyzer. For all experiments the employed instruments used a single reference clock.

5.7.2. The Optomechanical Cavity

Cavity Frequency

The lumped element microwave cavity consists of a meander inductor and two pads, which are capacitively coupled to the metallized membrane. The cavity is inductively coupled to a shorted reflection feedline. The bare cavity design without a flipped membrane is shown in Figure 5.6. The resonance frequency of the optomechanical cavity is given by

$$\omega_c = \frac{1}{\sqrt{L\left(C_0 + C_m\left(x\right)\right)}} \tag{5.2}$$

where L is the inductance consisting of two parts: geometric and kinetic, as described in Chapter 3. C_0 is the capacitance between the pads of the bare cavity and $C_m\left(x\right)$ the capacitance between the two pads and the metallized membrane.

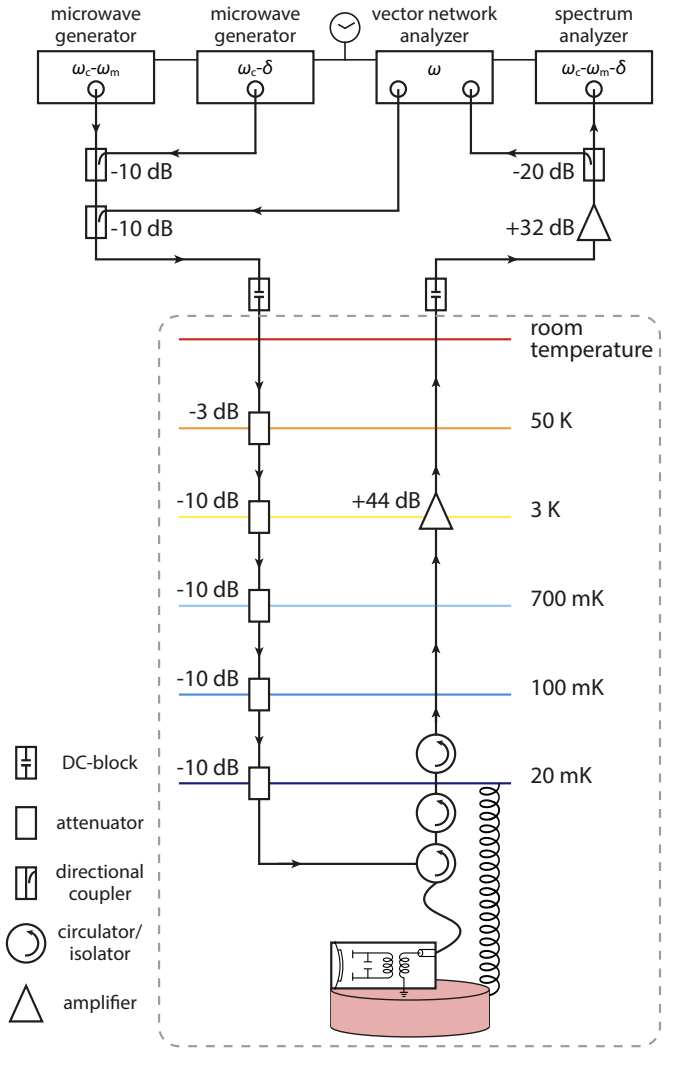


Figure 5.5: Schematic measurement setup. Detailed information is provided in main text.

$C_m(x)$ varies periodically due to the motion of the mechanical oscillator, and is the source of the optomechanical coupling between the microwave cavity and the membrane mode. The frequency of the optomechanical cavity is dependent on the distance d between the two chips obtained during the flip-chip assembly.

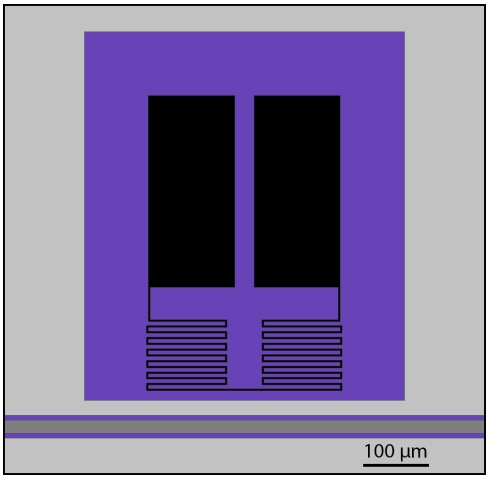


Figure 5.6: Geometry of the bare cavity and feedline. The silicon bottom chip (purple) with a superconducting ground plane (light gray) contain the bare cavity (black) inductively coupled to the shorted reflection feedline below (dark gray).

Microwave Response Function and Fitting Routine

For a series RLC-resonator side-coupled to a shorted reflection feedline the ideal response function is

$$S_{11}^{ideal} = 1 - \frac{2\kappa_{ex}}{\kappa_{tot} + 2i\Delta} \tag{5.3}$$

where $\Delta = \omega - \omega_c$ is the detuning of a probe tone. Here, the internal losses can come from many origins, as described in Chapter 2. However, in any experimental setup one will always encounter imperfections in the measurement setup. Cable resonances and impedance mismatches due to the components in the microwave line (attenuators, circulators, amplifiers, wirebonds etc.) affect the spectrum. This creates a frequency-dependent background and a modification of the cavity response to a Fano-like resonance [272, 273]. The reflection coefficient is altered to

$$S_{11} = A\left(1 - \frac{Be^{i\theta}}{\kappa_{tot} + 2i\Delta}\right) \cdot e^{i\phi} \tag{5.4}$$

where A, B, θ and ϕ are frequency-dependent factors. The measured cavity response is shown in Figure 5.7**ab**, where the asymmetric lineshape of the magnitude $|S_{11}|$ is visible. The phase response has a linear slope due to the build-up phase over the path length of the microwave lines. To analyze the cavity response correctly, we follow a fitting routine. First, we perform a Lorentzian fit on the cavity where we consider an exponential polynomial background

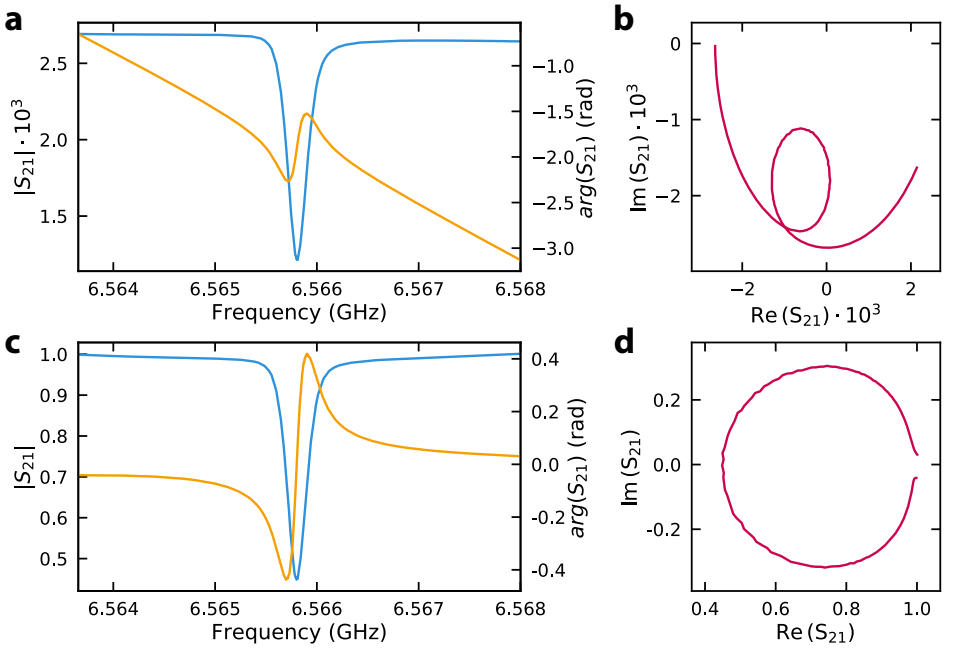


Figure 5.7: Full cavity response and background correction. Panels **a** and **b** show raw data of S_{11} of the cavity response, averaged over 500 traces. The magnitude (phase) is shown in blue (orange), together with the response in the complex plane in red. Panels **c** and **d** show the corresponding data after background correction and phase rotation.

$$S_{11} = S_{11}^{ideal} \cdot S_{11}^{bg} \tag{5.5}$$

$$S_{11}^{bg} = \left(a_b + b_b\omega + c_b\omega^2\right) \cdot e^{i\left(d_b + e_b\omega + f_b\omega^2\right)} \tag{5.6}$$

Second, we correct the measured data by removing the found background and apply a rotation in the complex plane by the phase factor $e^{-i\theta}$ with a phase θ. The modified response function is shown in Figure 5.7**cd** and is given by

$$S_{11}^{corrected} = \left(\frac{S_{11}}{S_{11}^{bg}} - 1\right) \cdot e^{-i\theta} + 1 \tag{5.7}$$

Frequency Fluctuations

When the measurement time of a single VNA trace is sufficiently short, we observe the cavity resonance frequency changing over time. Vibrations in the setup, dominated by the movement of the pulse tube cooler of the dilution refrigerator, cause the interchip distance to change. The phononic shield isolates the ground mode of the membrane from these vibrations with its designed band-stop filter, see

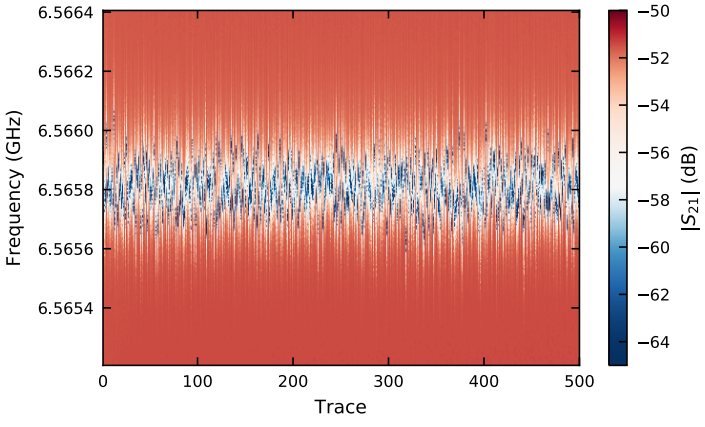


Figure 5.8: Cavity frequency fluctuations. Colormap of the measured S_{11} magnitude of fast VNA traces show a shifting cavity resonance. The time per trace is 100 msec (IFBW = 10 kHz). For time- or trace-averaged measurements the cavity's narrow linewidth broadens as the resonance is washed out over time.

Chapter 3. However, the low-frequency modes of the lattice structure can actually be excited by these vibrations. In practice, this means that the mechanical mode is isolated, but the membrane is located on a moving structure. Changing the distance between the membrane and the bottom chip changes the capacitance of the cavity, which, in turn, changes its resonance frequency ω_c. This is the main source of the frequency jittering we observe. We can separate the parametric coupling of the ground mode of the membrane from the vibrations as

$$C_m = C_{mode}(\omega_m) + C_{vib} \tag{5.8}$$

Figure 5.8 shows a VNA measurement of the cavity, the average of which is discussed in Figure 5.1**c**. Taken with an IFBW of 10 kHz, each of the 500 traces had a measurement time of 100 msec, consisting of 1001 points. We see the cavity frequency fluctuating on the order of the linewidth, effectively increasing its average internal decay rate. This leads to an underestimate of the cavity's quality factor.

5.7.3. OMIT Fitting Routine

The optomechanical transparency peaks were measured with a red sideband drive. Where necessary, multiple traces where averaged to increase signal to noise. Background correction and a rotation in the complex plane were performed according to the parameters found in the cavity response above. Each dataset was fit with a Lorentzian function. Since we work in the sideband-resolved regime, we are able to calculate the cooperativity from the extracted linewidths.

$$\mathcal{C} = \frac{\Gamma_{eff}}{\Gamma_m} - 1 \tag{5.9}$$

which is a measure for the cooling induced by the sideband drive. The cavity field enhanced photon-phonon coupling rate can be calculated with

$$g = \frac{1}{2}\sqrt{\Gamma_m \kappa_{tot} \mathcal{C}} \tag{5.10}$$

Finally, the estimated phonon occupation is calculated with

$$n_f = \frac{n_i}{\mathcal{C}+1} \tag{5.11}$$

where an initial thermalized occupation is n_i assumed, based on the thermal calibration noise measurements.

5.7.4. Further Discussion on Thermal Calibration

As discussed in Section 5.4, we have performed a set of measurements to test certain assumptions that were made for the thermal calibration of the membrane mode. In Figure 5.9**a** we show the single-tone spectroscopy response of the cavity for the different cryostat temperatures. Each measured response is offset by 1 MHz for clarity. The cavity lineshape clearly changes considerably as both κ_{in} and κ_{ex} do not show a clear dependency on temperature. The second observation we make is the change in background level. Wide span measurements displayed an overall changing background level, as well as shifting cable resonances. This indicates both a change in attenuation and impedances in the microwave setup. After a thorough investigation we were able to narrow this effect down to the flexible cable going down to the mass-spring system. Four different kinds of flexible cables were tried, each exhibiting these effects in different amounts.

A rough estimation based on the varying background level leads to a factor ~ 2 difference in power reaching the device for these measurements. The internal and external decay rates extracted from fits of the cavity also show an additional factor ~ 2 difference for the intracavity photon number, and thereby the Stokes scattering rate, at these temperatures.

Figure 5.9**b** shows how this changing spectrum poses a challenge. The noise power of the mechanical mode is recorded with an IQ time trace on a spectrum analyzer. For decreasing temperatures we see the voltage PSD peaks decrease, as one would expect for a thermalized mode. Each peak is offset by 1 Hz along the x-axis for clarity. The color coding corresponds to that in Figure 5.3. For the lowest cryostat temperatures ($\leq 100\,\mathrm{mK}$) one would expect the peak height and area to level off, as the mode temperature stabilizes. However, we still see fluctuations in the peak that correspond to the changes of the cavity linewidth and background. For low refrigerator temperatures the integrated area of the peak varies around an average value of $72\,\mathrm{nV}^2$, as shown in Figure 5.3.

5.7.5. Mechanical Noise Fitting Routine

The signal returning from the dilution refrigerator is first amplified and then split to the two measurement instruments. The signal lead to the spectrum analyzer

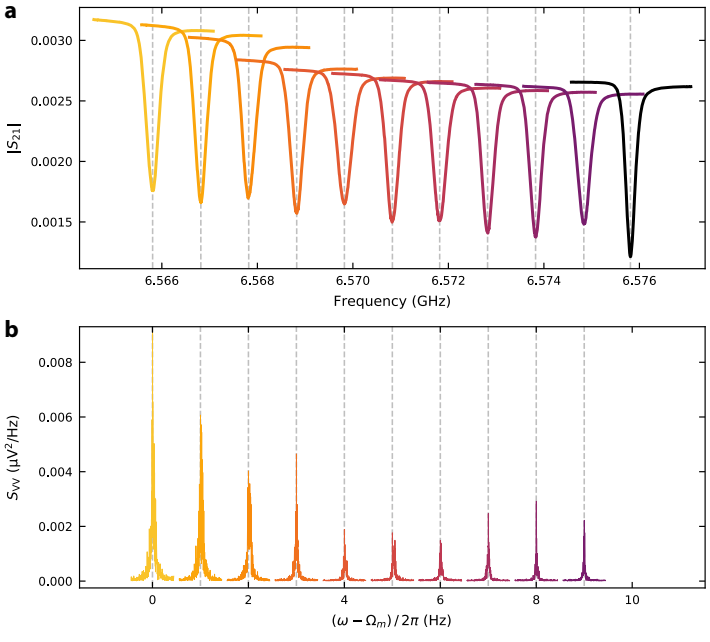


Figure 5.9: Temperature dependence of the cavity and sideband noise spectra. **a** Magnitude $|S_{11}|$ response of the cavity for cryostat temperatures ranging from 400 mK (yellow) to base temperature $\sim$20 mK (purple), and during the sideband cooling measurements (black). Subsequent traces are each an average of 500 traces and offset by 1 MHz. Each measurement shows a different background level and cavity lineshape $(\kappa_{in}, \kappa_{ex})$. **b** Noise measurements of the mechanical motion for cryostat temperatures ranging from 400 mK to base temperature $\sim$ 20 mK with corresponding color coding. Each dataset is bin-averaged 4 times offset by 1 Hz for clarity.

goes through the through-port of the directional coupler, to maximize the signal strength. The two quadratures of the signal are recorded with a duty cycle, after which the time segments are stitched together. A complex Fourier transform is applied in Python to the total time trace to calculate the voltage power spectral density. The resulting data is bin-averaged where necessary to resolve the peak over the noise floor. This was especially required for the datasets of the cooling measurements with a high pump power.

We perform a Lorentzian fit op top of a flat background on the averaged PSD in multiple steps. First, we find fit parameters for a Lorentzian function over the entire span within the used IFBW. These parameters are used as the input for a Lorentzian plus linear fit. The data is then sliced around the peak to maximize its participation over the flat noise floor. We repeat this two-step fitting routine with the found parameters as starting values. The bin-averaged data and final fits of all sideband cooling measurements are shown in Figure 5.10.

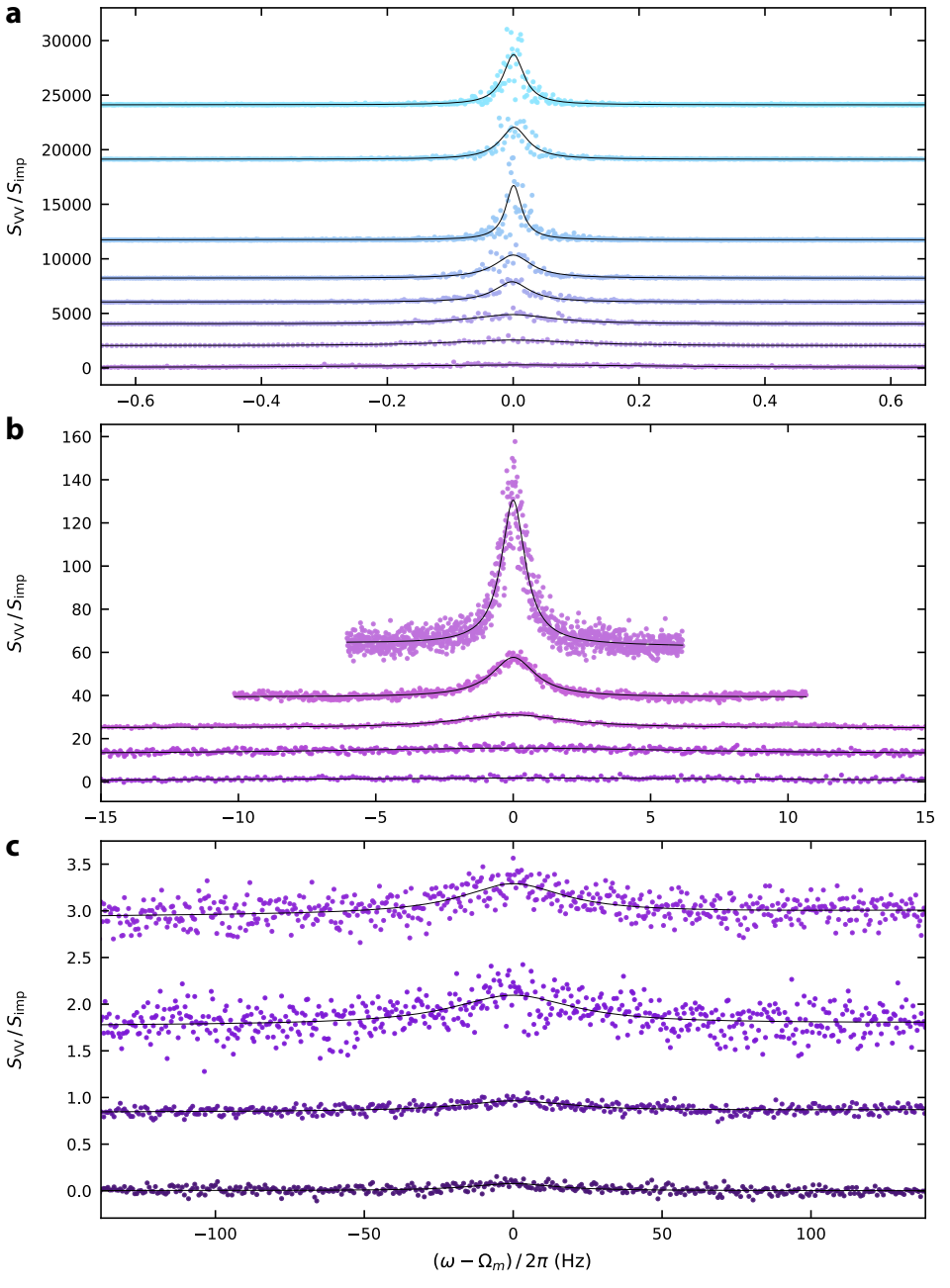


Figure 5.10: Mechanical noise during sideband cooling. Noise measurements of the mechanical motion for a red sideband drive power between −12 dBm (light blue) and 25 dBm (purple). Circles are bin-averaged data, black lines are Lorentzian plus flat background fits. Each dataset and fit is vertically offset for clarity. As the pump power increases, the peak height decreases and its width increases, indicating cooling of the mechanical mode.

The Lorentzian contribution of the fit is then integrated over a span of 1 kHz, much wider than the FWHM of the widest measured noise peak. This integrated voltage power spectral density is discussed in detail in Sections 5.4 and 5.5. For each cryostat temperature and each sideband drive power the noise floor was calculated from the flat contribution of the fit and is presented in Figure 5.11. The noise floor does not rise consistently with temperature or pump power. Therefore, we can conclude the measurements are not limited by phase noise of the microwave generator, causing energy dissipation heating up the mechanical resonator [36].

From the Lorentzian fit the mechanical linewidth Γ_{eff} was extracted, which can be seen to grow up to a drive power of 24 dBm (251 mW) at the generator output in Figure 5.12**a**. Higher drive powers show a decreasing FWHM, which could be caused by the cavity noise the system suffers from. In the multitone measurement scheme, the measured linewidth is composed of three parts: the mechanical linewidth and the optomechanical damping rates induced by the two drives $\Gamma_{eff} = \Gamma_m + \Gamma_{OM}^{sb} + \Gamma_{OM}^{\delta}$. The optomechanical damping rate produced by the drive tone sent within the cavity linewidth is found by

$$\Gamma_{OM}^{\delta} = g^2 \left(\frac{\kappa_{tot}}{\kappa_{tot}^2/4 + (\Delta + \Omega_m)} - \frac{\kappa_{tot}}{\kappa_{tot}^2/4 + (\Delta - \Omega_m)} \right) \tag{5.12}$$

where $\Delta = \omega_c - \delta$ [38]. At a detuning of $\delta = 2\pi \cdot -85.7$ kHz we calculate an additional cooling rate of $\Gamma_{OM}^{\delta} = 2\pi \cdot 2.54$ mHz. Correcting for this widening we find a mechanical linewidth of $\Gamma_m = 2\pi \cdot 37.3$ mHz. From this we calculate a mechanical quality factor of $Q_m = 2.62 \cdot 10^7$. Furthermore, we observe an upwards frequency shift as the sideband drive power is increased, as shown in Figure 5.12**b**.

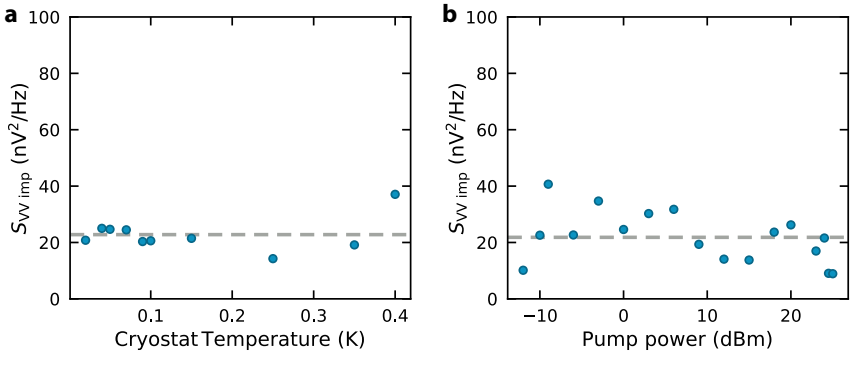


Figure 5.11: Voltage imprecision noise during the measurement sets. The voltage imprecision noise level at **a** different cryostat temperatures, and **b** different red sideband drive powers. The averages are shown with gray dashed lines. The imprecision noise does not significantly change with increasing pump power or temperature.

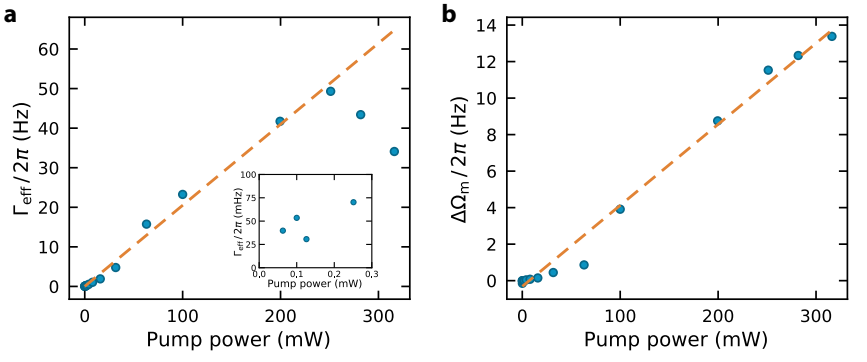


Figure 5.12: Mechanical linewidth and frequency shift during sideband cooling. Panel **a** shows the FWMH of the mechanical noise peak extracted from the Lorentzian fit as circles. A linear fit (dashed line) is performed up to a pump power of 251 mW. The inset shows a zoom-in close to 0 drive power. Panel **b** shows the frequency shift of the mechanical mode as extracted from the Lorentzian fit (circles), and a linear fit (dashed line) with a slope of 44 $\frac{\mathrm{Hz}}{\mathrm{W}}$.

6

Suppressing Cavity Frequency Noise Using a Kerr Nonlinearity

The introduction of a Duffing nonlinearity has applications in many fields of research. In this work, we present a microwave cavity in a flip-chip geometry that employs this nonlinear behavior. A superconducting qubit is coupled via its dipole moment to the microwave cavity, inducing a self-Kerr nonlinearity in the resonator. We characterize the dispersive coupling using single-tone spectroscopy. Applying a red-detuned microwave tone, we observe a transition of the cavity into a bistable regime where signal and idler resonances appear. The Kerr nonlinearity creates an internal feedback loop that suppresses cavity frequency noise, resulting in a reduced linewidth from $2\pi \cdot 15$ *MHz to* $2\pi \cdot 7.6$ *MHz. These results present a novel approach for stabilizing microwave resonators.*

J.P. van Soest, G.L. Bhai, S. Meilof, M. Villiers, C.A. Potts, and G.A. Steele, *Suppressing Cavity Frequency Noise Using a Kerr Nonlinearity*, *in preparation* (2025)

6.1. Introduction

Nonlinear oscillators are ubiquitous in nature, appearing across mechanical, optical, and condensed matter systems [274]. Often, in describing a system's response, nonlinear effects can be neglected, and the remaining harmonic oscillator model is one of the most useful approximations for describing almost any physical system. However, when nonlinear terms become prominent, often more fascinating physics emerges. Driven and dissipative Duffing nonlinear oscillators have been studied in a wide range of fields of research. In the field of circuit quantum electrodynamics (cQED) this type of nonlinearity is typically introduced via the Josephson junction [275]. The size of the Kerr nonlinearity in relation to the dissipation rate of the oscillator gives rise to various parameter regimes and applications, ranging from bistability and parametric amplification [276, 277]. The Josephson junction is highly engineerable and can be used to access these regimes [278, 279].

For circuits with a Kerr nonlinearity much smaller than the resonator linewidth ($\mathcal{K} < \kappa$), the system can be described as a driven classical Duffing oscillator [280]. This regime is typically encountered in the application of parametric amplifiers, for example, the Josephson parametric amplifier (JPA) and the Josephson bifurcation amplifier (JBA) [281–284]. These devices are widely used in cQED experiments and approach quantum limited amplification.

Circuits can also be designed to operate in the single-photon Kerr regime, where the Kerr nonlinearity greatly surpasses the resonator's decay rate ($\mathcal{K} \gg \kappa$). The nonlinearity-induced frequency shift of the resonator limits its occupation due to the photon blockade [285]. Such a resonator can be approximated as a two-level system or an artificial atom, with a well-known example being the transmon qubit [185].

Furthermore, there has been an increased interest in integrating nonlinear circuits in optomechanical systems. This can be used to create a flux-mediated optomechanical interaction [92–95, 286], or to increase the optomechanical coupling and enhance the performance of the device [97–99, 101, 102, 105, 106].

In this work, we present a nonlinear microwave cavity in a flip-chip geometry. A dipole coupling between a transmon qubit and the cavity is created, inducing a self-Kerr nonlinearity in the cavity. The AC Stark shift is observed in both a readout resonator coupled to the qubit and the flip-chip cavity with single-tone spectroscopy. Tuning the magnetic flux through the superconducting quantum interference device (SQUID) of the transmon results in a frequency shift of the resonator. Finally, we stabilize the noisy cavity via Kerr locking with a strong second tone. When driving the cavity beyond its bifurcation point, signal and idler resonances emerge. This locking mechanism mitigates and removes low-frequency cavity fluctuations.

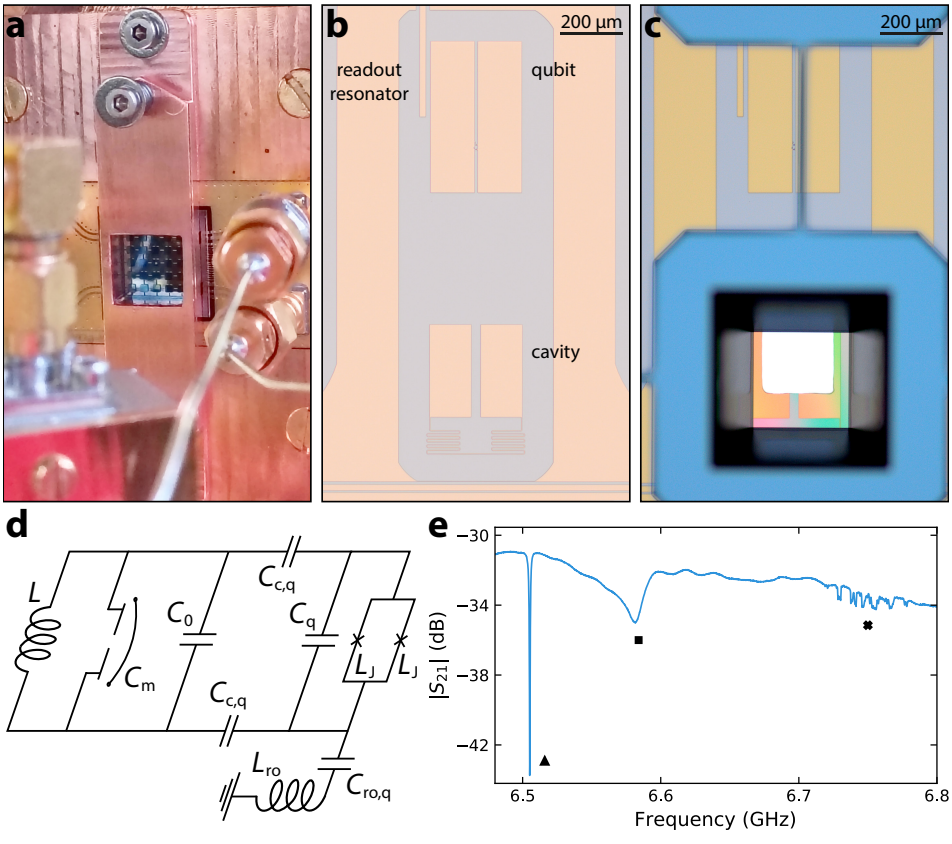


Figure 6.1: A cQED flip-chip device. Panel **a** shows a photograph of the flip-chip device. The membrane (white square) is visible in the phononic shield (blue lattice). **b** Optical micrograph of the center of the microwave chip, where the cavity, qubit and readout resonator are annotated. Panel **c** shows the device after assembly of the flip-chip. Part of the phononic shield can be seen as the blue lattice structure. A color gradient from white-light interference is visible through the membrane, indicating a sub-micron gap. The white square of evaporated aluminum on the membrane is aligned with the microwave cavity underneath. **d** Schematic representation of the circuit. Panel **e** shows the magnitude $|S_{21}|$ transmitted spectrum of the device. Three resonances are shown: the reference resonator (▲), the qubit readout resonator (■), and the flip-chip cavity (✖).

6.2. Experimental Setup

Our device consists of two chips in a flip-chip geometry, shown in Figure 6.1**a**. The top chip contains a high-tensile stress silicon nitride membrane located within an in-substrate phononic shield, and is brought close to the bottom chip, which contains a superconducting microwave circuit. The membrane is 300 µm × 300 µm wide and 100 nm thick, and metallized with 250 µm × 250 µm × 50 nm evaporated aluminum, as described in Chapter 3. At the core of the device is a lumped element

microwave cavity coupled to a transmission line. It consists of a meander inductor and two capacitor plates etched into a 100 nm thick film of NbTiN. This bare cavity is designed to have a resonance frequency of $\omega_{c,bare} = 2\pi \cdot 19.65$ GHz. The capacitively coupled membrane brings the cavity's frequency down to $2\pi \cdot 6.76$ GHz. Eigenmode simulations varying the gap between the two chips predict a separation of 280 nm, as described in Section 6.6.3. Optical micrographs taken before and after assembly of the flip-chip are shown in Figure 6.1**bc**.

Capacitively coupled to the cavity is a floating double-island transmon qubit. The total inductance of the qubit can be controlled with an external magnetic coil, which threads a magnetic flux through the 125 μm^2 asymmetric SQUID loop, see Chapter 3 for detailed information. Through its simulated dipole coupling $g_{cq} = 2\pi \cdot 1$ MHz, the qubit induces a self-Kerr nonlinearity in the cavity by

$$\mathcal{K}_c = \mathcal{K}_q \cdot \left(\frac{g_{cq}}{\Delta_{cq}}\right)^4 \tag{6.1}$$

where $\mathcal{K}_q = -\frac{E_c}{\hbar}$ is the self-Kerr nonlinearity of the qubit, dependent on its charging energy E_c. The qubit's detuning with respect to the cavity is given by Δ_{cq}. Furthermore, the qubit is coupled to a coplanar waveguide readout resonator. The circuit equivalence of the device is shown in Figure 6.1**d**.

Additionally, multiple reference resonators are coupled to the transmission line for characterization of the internal and external decay rates. Applying single-tone spectroscopy, without any applied magnetic field, Figure 6.1**e** shows the measured $|S_{21}|$ magnitude spectrum. One of these reference resonators is visible as a sharp dip with internal and external decay rates of $\kappa_{in} = 2\pi \cdot 123$ kHz and $\kappa_{ex} = 2\pi \cdot 593$ kHz, as extracted from fits. The readout resonator is visible at $\omega_{ro} = 2\pi \cdot 6.58$ GHz with a linewidth of $\kappa_{tot} = 2\pi \cdot 16.6$ MHz. Lastly, a noisy resonance is visible, indicating the flip-chip cavity at $\omega_c = 2\pi \cdot 6.76$ GHz.

The flip-chip device is clamped with spring-loaded screws and vertically mounted on a mass-spring system, hanging below the base plate of a dilution refrigerator ($T \approx 20$ mK). More details on the flip-chip device and on the measurement setup are given in Chapter 3 and Section 6.6.1.

6.3. Dispersive Cavity-Qubit Coupling

We present the response of three resonators when we probe the system with a microwave tone through the transmission line, each displaying their unique characteristics. Figure 6.2**a** shows a colormap of the $|\Delta S_{21}|$ magnitude against probe frequency and power at the room temperature end of the measurement chain. As we increase the probe power, the resonator at $\omega_{ref} = 2\pi \cdot 6.505$ GHz is unaffected, as its circuit elements are linear with intraresonator photon number. The qubit readout resonator at $\omega_{ro} = 2\pi \cdot 6.58$ GHz, however, shows a downward frequency shift with increasing probe power, as it inherits a Kerr nonlinearity due to its dispersive coupling to the qubit $\omega = \omega_{dressed} + n\mathcal{K}$. The shift is dependent of the

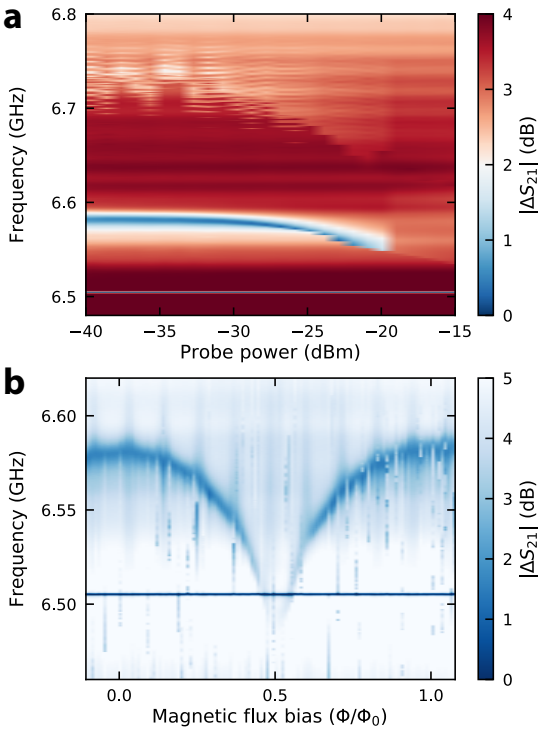


Figure 6.2: Nonlinear cavity response due to dispersive coupling to a transmon qubit. a Colormap of the magnitude of the $|\Delta S_{21}|$ single-tone spectroscopy response of the system, normalized to zero. The linear resonator at $2\pi \cdot 6.505$ GHz shows no dependence on the probe power. The readout resonator at $2\pi \cdot 6.58$ GHz undergoes an AC Stark shift as the probe tone increases in power. The flip-chip cavity exhibits frequency fluctuations around its average resonance frequency of $2\pi \cdot 6.76$ GHz. Its frequency shifts with increased intracavity photon number. Panel **b** shows the normalized response of the system dependent on the external magnetic flux Φ in units of flux quanta Φ_0, obtained by sweeping the current in the external magnetic coil. The linear resonator shows no dependence on the magnetic field. The readout resonator undergoes a significant frequency shift as the qubit detuning decreases.

photon number n in the resonator. For large n the resonator reaches a regime of strongly asymmetric response, as is expected from the equations of motion of a Duffing resonator [287]. The third resonator in this frequency span is observed as a noisy resonance suffering from frequency fluctuations around $\omega_c = 2\pi \cdot 6.76$ GHz, which we identify as the flip-chip cavity. The induced self-Kerr nonlinearity causes a frequency shift downward as the number of intracavity photons increases. As the probe power increases the average cavity lineshape reaches a regime of strongly asymmetric response.

In Figure 6.2**b** the response of the system to an applied external magnetic flux

is shown, obtained by sweeping the current in the external magnetic coil. As the nonlinear inductance of the Josephson junctions increases, the qubit frequency decreases. This lowers the detuning Δ of the qubit with respect to the coupled resonators, which increases their Kerr nonlinearity. The readout resonator displays a significant periodic frequency shift [39, 185].

As we aim to decrease the gap between the two chips of the device, the cavity becomes more susceptible to vibrational noise. A small change in the interchip distance results in a larger frequency shift, see Section 6.6.3. Moreover, the flip-chip cavity's frequency can shift due to the qubit's sensitivity to magnetic field fluctuations. This cavity noise causes a significant increase in the time-averaged cavity linewidth. Measuring the resonance at a timescale shorter than the frequency fluctuations allows us to see the cavity's unperturbed linewidth of $\kappa_{tot} \approx 2\pi \cdot 15$ MHz, as discussed in Section 6.6.2. Furthermore, we observe a fast changing periodic frequency shift of the cavity, caused by a flux dependent force, the origin of which is still under investigation [288–293]. Therefore, to minimize the frequency fluctuations, for the following experiments we operate the flip-chip cavity at its highest frequency point, corresponding to the flux sweet spot of the readout resonator.

6.4. Kerr Locking the Nonlinear Cavity

Given that our flip-chip cavity suffers from such large frequency fluctuations, its average linewidth is increased and the cavity washes out in the background. In addition to reducing its quality factor, this is especially detrimental in the application of optomechanical experiments, as this complicates any detection of or control over the mechanical mode. However, we can take advantage of the cavity's coupling to the qubit. Specifically, we will use the induced Kerr nonlinearity of the cavity to our benefit. In Figure 6.3**a** we show a two-tone spectroscopy measurement, where a probe tone is swept over the resonance. A second pump tone with a fixed detuning $\Delta_d = 2\pi \cdot -68$ MHz below the average cavity frequency, as indicated by the black dashed line, is increased in power. The probe power is sufficiently low to not influence the cavity's frequency and lineshape. As pump power increases, the cavity frequency shifts towards the pump frequency due to the Kerr effect, further increasing the intracavity photon number of the drive tone. For low powers (or large detunings) the cavity exhibits its wide and fluctuating response. However, when the pump power is increased above -20.0 dBm at the generator output, the single-mode resonance is suddenly transformed into a two-mode response. These signal and idler modes are located symmetrically around the pump. The signal mode on the opposite side of the drive can be seen as the dressed cavity. These two intracavity fields originate from a four-wave mixing process with the photons from the pump tone. The frequencies of these modes are given by the real-valued function

$$\omega_{i/s} = \omega_d \pm \sqrt{(\Delta_d - \mathcal{K}_c n_c)(\Delta_d - 3\mathcal{K}_c n_c)} \tag{6.2}$$

with $\Delta_d = \langle \omega_c \rangle - \omega_d$ and n_c the intracavity photon number due to the drive [271]. The observed signal and idler resonances appear after the exceptional point

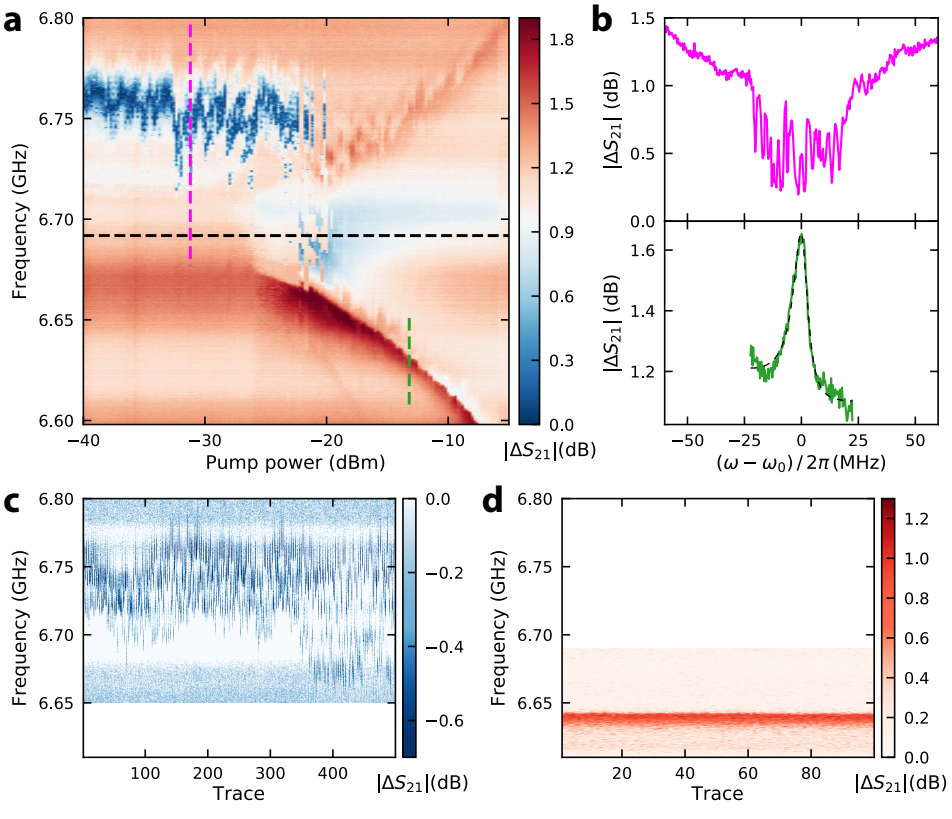


Figure 6.3: Kerr locking the nonlinear cavity. Panel **a** shows a normalized colormap of the magnitude $|\Delta S_{21}|$ response during a two-tone spectroscopy measurement. The pump tone is red-detuned from the average cavity frequency $\omega_d = \langle\omega_c\rangle - 2\pi\cdot 68$ MHz, as indicated by the black dashed line. The pump power is increased, while a weak, non-intrusive probe tone is swept over the resonance. At low drive powers we observe the frequency fluctuations of the cavity around an average of $2\pi \cdot 6.76$ GHz. When the pump power is increased above -20.0 dBm the system jumps to a double-peak region. These signal and idler modes are stabilized in frequency, as the noise is removed by the feedback mechanism due to the Kerr nonlinearity. Traces before and after Kerr locking are shown in panel **b** centered around each resonance respectively, and are indicated by the pink and green lines. A Lorentzian fit (black dashed line) shows a narrow linewidth of the signal mode of $\kappa_s = 2\pi \cdot 7.6$ MHz. **c** Fast VNA traces display frequency fluctuations and linewidth broadening for the unlocked cavity. The stabilized signal mode is shown in **d**.

reached at $n_c = \Delta_d/3\mathcal{K}$. As the pump power increases, the separation of the quasi-modes enlarges.

An interesting feature is that both the signal and idler modes appear as peaks, indicating a net gain due to constructive interference of the four-wave mixing process. Therefore, the parametric amplification surmounts the internal losses of the

cavity [270, 271]. For different detunings Δ_d the signal mode gradually transforms from a peak to a dip as the pump power is increased. These measurements, as well as the data analysis, are discussed further in Section 6.6.4. For all two-tone experiments presented in this work the cavity remained in the high-amplitude branch.

The appearance of these modes comes with a particularly interesting feature. In addition to the amplification of the intracavity field, the resonances are stabilized and their linewidths decreased. This phenomenon has been called Kerr locking and works with a feedback process [97]. The feedback loop stabilizes the cavity as follows: when the frequency of the unlocked cavity fluctuates, the detuning to the pump Δ_d changes. Either more or less photons from the drive will enter the cavity, which causes a countering frequency shift. Thereby, the frequencies of the signal and idler modes $\omega_{i/s}$ will in turn only vary minimally, as given by Equation 6.2. As a result, cavity noise is removed by the nonlinear feedback mechanism. This process greatly narrows the linewidths of the signal and idler modes compared to the unlocked cavity linewidth of $2\pi \cdot 15$ MHz. From the Lorentzian fit in Figure 6.3**b** we extract $\kappa_s = 2\pi \cdot 7.6$ MHz for the signal mode. All cavity frequency fluctuations are mitigated, as the signal mode is completely stabilized, as shown in Figure 6.3**cd**. We observe a maximum output gain of approximately 1 dB.

6.5. Discussion & Outlook

We presented suppression in frequency fluctuations by Kerr locking a noisy cavity to a strong drive tone. A floating transmon qubit was coupled to a readout resonator and a flip-chip microwave cavity. Using single-tone spectroscopy, the AC Stark shift of the readout resonator was observed. Furthermore, by sweeping the current in an external magnetic coil we were able to tune the qubit closer to the resonators, thereby shifting the resonator periodically. When a red-detuned second microwave tone was applied with sufficient power, the flip-chip cavity, highly fluctuating in frequency due to an increased sensitivity to mechanical vibrations and magnetic field noise, reached its bifurcation point. At this threshold, a sudden transition of the cavity mode to signal and idler resonances occurred. The two modes eliminate the cavity noise due to the nonlinear feedback mechanism intrinsic to the four-wave mixing process activated by the drive tone. The stabilized signal mode shows a reduced linewidth of $\kappa_s = 2\pi \cdot 7.6$ MHz, compared to the unlocked cavity linewidth of $\kappa_{tot} = 2\pi \cdot 15$ MHz.

The implementation of Kerr locking microwave systems has a variety of applications, ranging from parametric amplifiers to the stabilization of nonlinear optomechanics. This work is a first step towards tunable nonlinear optomechanical experiments using a flip-chip device. Recently, nonlinearities were used for creating Kerr-enhanced backaction [101, 102] and enhancing flux-mediated optomechanical interactions [95, 97, 104, 292, 294, 295]. Moreover, Kerr optomechanics could be used for intracavity squeezing [100, 296, 297] and quantum transduction [298, 299]. In other systems involving these quasi-modes, level attraction was observed,

creating exceptional points [271, 300–303]. Finally, coupling an optomechanical cavity to a qubit has been discussed as a platform in which one could prepare mechanical quantum states [75, 87–91, 107].

6.5.1. Contributions

All authors were engaged in conceiving the concepts around tunable nonlinear optomechanics. J.P.S. and M.V. designed the microwave device and performed the simulations. J.P.S. fabricated the device based on the flip-chip technique developed by J.P.S. and S.M. J.P.S. and G.L.B. conducted the measurements. J.P.S. wrote the chapter with input from everyone. G.A.S. supervised the project.

6.5.2. Acknowledgments

We thank Matteo Arfini, Robin Dekker and Sercan Deve for help with the device fabrication, and Ronald Bode for the fabrication of the flip-chip holder.

6.6. Supplementary Information

6.6.1. Measurement Setup

The experiments in this work were performed in a dilution refrigerator at a base temperature of $T_{base} \approx 20$ mK. The flip-chip device, whose design and fabrication is described in Chapter 3, is mounted on a mass-spring system hanging below the mixing chamber plate. A schematic diagram of the experimental setup is shown in Figure 6.4. The copper mass is thermalized to the base plate through a flexible copper braid. On the mass a temperature sensor is installed, which is monitored with an AC resistance bridge. Coaxial microwave lines connect the device to the outside of the cryostat. All lines contain DC blocks at room temperature to isolate the system from DC currents and to prevent ground loops. The input line to the device is strongly attenuated. A total of 49 dB of attenuation was used, on top of the attenuation from the coaxial cables themselves, to block thermal radiation of the line from reaching the device. The final attenuation stage is created by a directional coupler, where most power is lead back up, through identical attenuators, to be dissipated at the 3 K stage. This power dump was installed to enable large drive powers without heating the base plate of the refrigerator. Two flexible microwave cables are guided to two isolators, thermalized to and mounted on the mass as close to the flip-chip device as possible. These isolators are installed to reduce the cable resonances we observe over the entire bandwidth. A high-electron-mobility transistor (HEMT) amplifier with a gain of 44 dB and bandwidth of $4 - 8$ GHz was placed on the output line at the 3 K stage. Two additional isolators where installed between the HEMT and the copper mass to block the thermal radiation of the amplifier from reaching the device.

An external magnetic coil is mounted on the back side of the flip-chip holder, at a distance of 13 mm from the chip. The coil contains 600 turns of superconducting wire and is aligned to flux-bias the SQUID loop of the qubit. A DC current can be sent with a low noise current source, connected with a twisted wire pair. A mu-metal shield is installed inside the vacuum can to shield the entire volume below the 3 K stage from magnetic flux noise. The device, microwave components mounted on the mass, and magnet are presented in Chapter 3.

Outside the refrigerator we use a a single measurement setup for the experiments presented. A vector network analyzer (VNA) is used to send the probe signal to the device. Before reaching the cryostat, the signal goes through a power combiner, together with the pump tone from a microwave generator. The signal in the output line of the cryostat first goes through a room temperature amplifier before returning to the VNA. For all experiments the employed instruments used a single reference clock.

6.6.2. The Microwave Resonances

In Figure 6.5**ab** we show the measured response of one of the reference resonators. The resonator has an identical meander inductor as the flip-chip cavity and is side-coupled to the transmission line. The resonator is completed with an interdigital

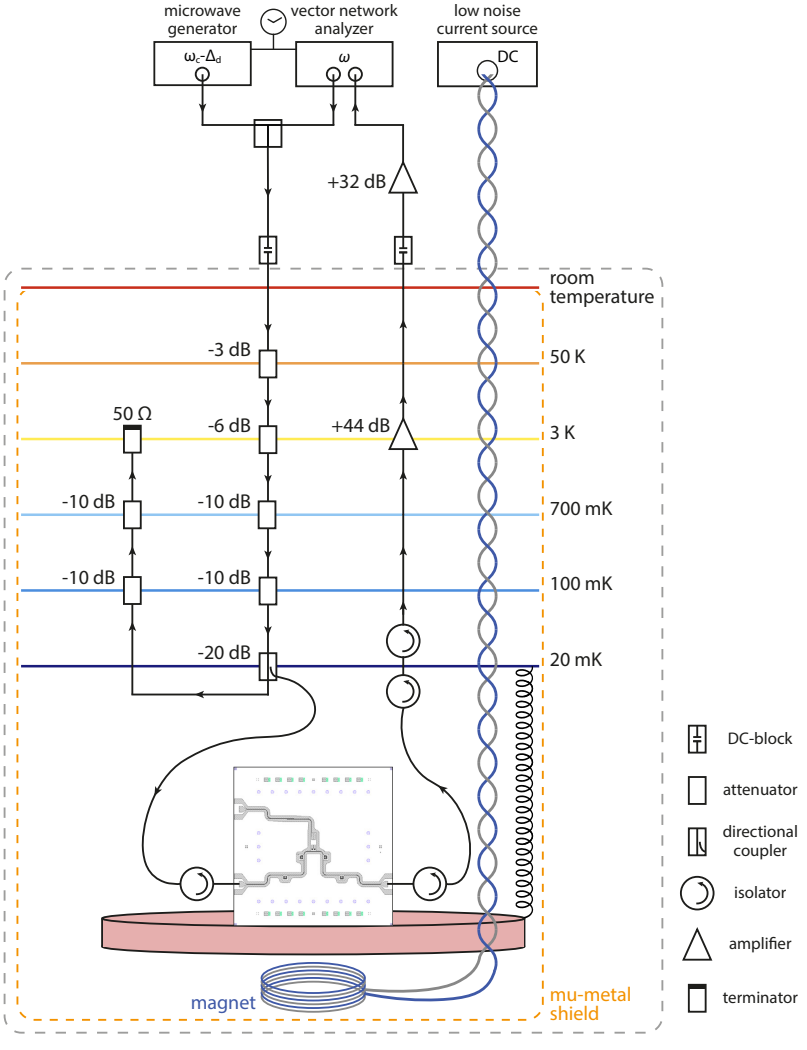


Figure 6.4: Schematic measurement setup and microwave chip design. Detailed information is provided in main text.

capacitor (IDC), as a substitute of the capacitance created by the metallized membrane. The 11 fingers are each 248 µm long, and the width of and gap between the fingers are both 5 µm. Using the analytical expressions provided in Ref. [188, 189] and a relative permittivity of $\epsilon_r = 11.68$ for the silicon substrate, we calculate a capacitance of $C = 146$ fF for the resonator designed at $2\pi \cdot 6.0$ GHz. The resonator is located underneath a hole of the phononic shield, such that we can neglect the permittivity of the silicon top chip, as calibrated by finite element simulations.

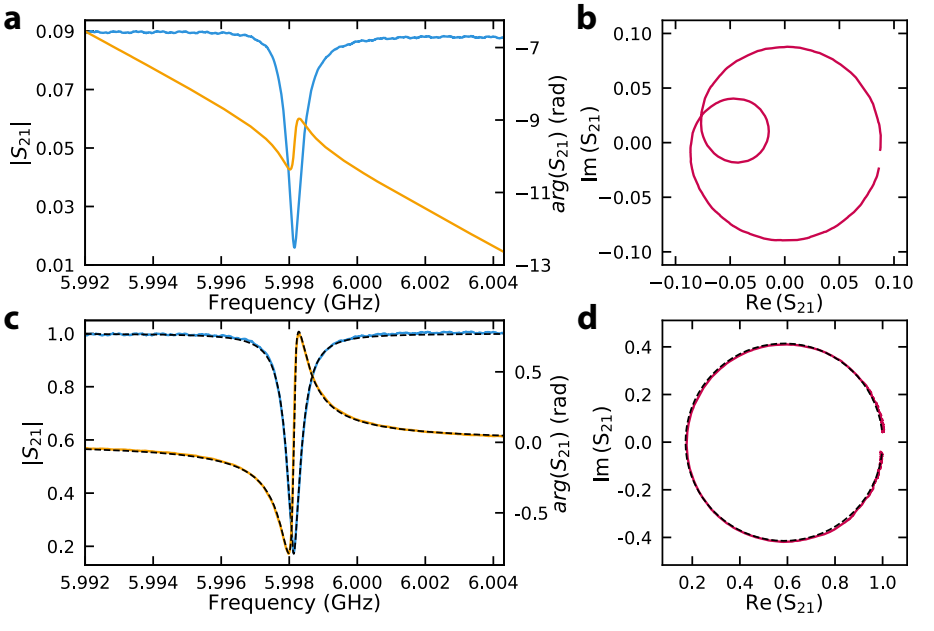


Figure 6.5: Full reference resonator response and background correction. Panels **a** and **b** show the raw data of S_{21} transmission of one of the reference resonator's response. The magnitude (phase) is shown in blue (orange), together with the response in the complex plane in red. Panels **c** and **d** show the corresponding data after background correction and phase rotation. The Lorentzian fit is shown as black dashed lines.

An LC-resonator side-coupled to a transmission feedline can be described by the ideal response function

$$S_{21}^{ideal}(\omega) = 1 - \frac{\kappa_{ex}}{\kappa_{tot} + 2i\Delta} \tag{6.3}$$

where $\Delta = \omega - \omega_c$. No experimental setup, however, is ideal. Therefore, we consider a frequency-dependent complex background to the resonance, caused by amplitude and phase modulation due to the microwave components in the measurement setup. Moreover, we take into account a modification of the cavity response to a Fano-like resonance [272, 273]. The modified response function is given by

$$S_{21}^{corrected}(\omega) = \left[S_{21}^{ideal}(\omega) \cdot \left(\left(a_b + b_b\omega + c_b\omega^2 \right) \cdot e^{i\left(d_b + e_b\omega + f_b\omega^2\right)} \right)^{-1} - 1 \right] \cdot e^{-i\theta} + 1 \tag{6.4}$$

where we consider an exponential polynomial background function. Additionally, a rotation in the complex plane is applied by the phase factor $e^{-i\theta}$ with a phase θ. The corrected data, together with a Lorentzian fit, is shown in Figure 6.5**cd**. We

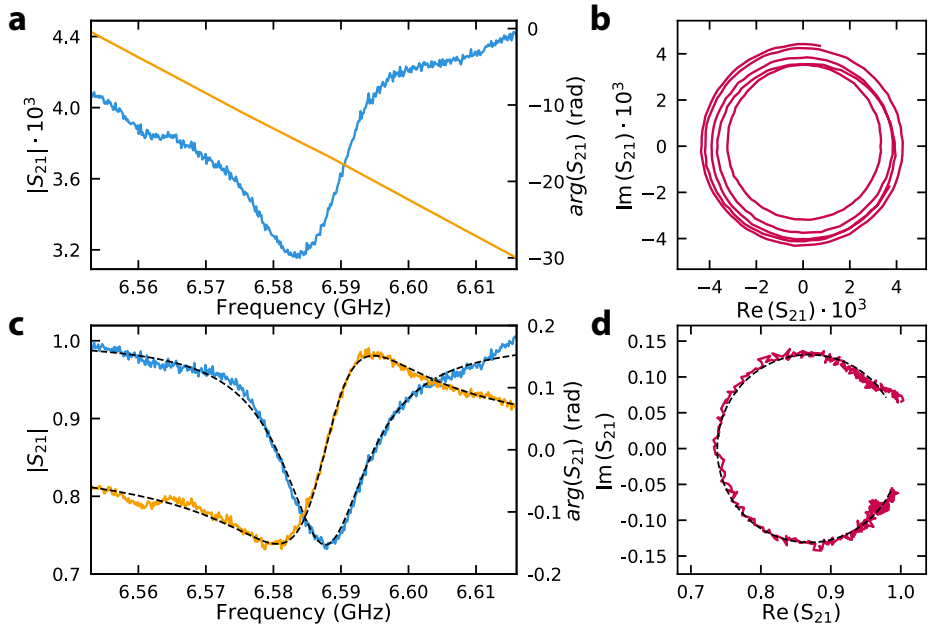


Figure 6.6: Readout resonator response and background correction. Panels **a** and **b** show the raw data of S_{21} transmission of the qubit readout resonator response. The magnitude (phase) is shown in blue (orange), together with the response in the complex plane in red. Panels **c** and **d** show the corresponding data after background correction and phase rotation. The Lorentzian fit is shown as black dashed lines.

extract a resonance frequency of $\omega_{ref} = 2\pi \cdot 5.998$ GHz. Using $\omega = \frac{1}{\sqrt{LC}}$, we calculate the total inductance of $L_{tot} = 4.82$ nH. The internal and external resonator decay rate obtained from the fit are $\kappa_{in} = 2\pi \cdot 123$ kHz and $\kappa_{ex} = 2\pi \cdot 593$ kHz.

We will also consider the readout resonator, as measured through the transmission line. To ensure the resonance does not exhibit the nonlinear frequency shift or measurable asymmetry, a probe tone is sent to the device with a sufficiently low power. The measured response is shown in Figure 6.6**ab**. We apply a similar background correction and complex rotation as described above, and perform a Lorentzian fit, as shown in **cd**. The resonance frequency and linewidth obtained are $\omega_{ro} = 2\pi \cdot 6.58$ GHz and $\kappa_{tot} = 2\pi \cdot 16.6$ MHz.

As described in the main text, the flip-chip cavity undergoes such large cavity noise that without Kerr locking the frequency fluctuations make the time-averaged cavity very broad. Because the cavity is almost washed out into the background, we cannot perform a reliable fit. However, performing fast VNA measurements at a timescale shorter than the frequency fluctuations, we were able to obtain the cavity's unperturbed linewidth. The IFBW used was 10 kHz, resulting in a mea-

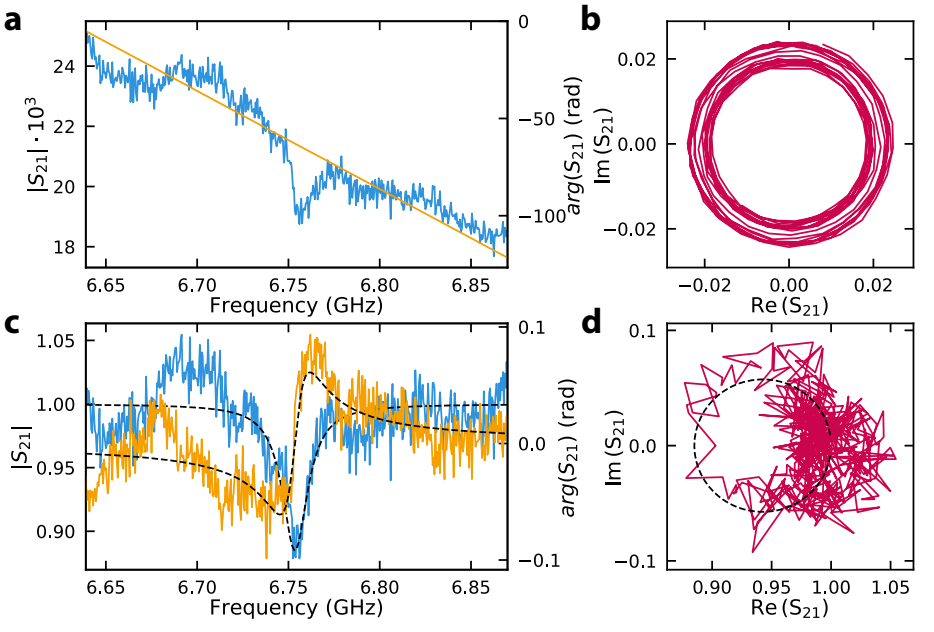


Figure 6.7: Response of the unlocked flip-chip cavity. Panels **a** and **b** present a single measured trace of the S_{21} response of the flip-chip cavity. The magnitude (phase) is shown in blue (orange), together with the response in the complex plane in red. Panels **c** and **d** show the corresponding data after background correction and phase rotation. The Lorentzian fit is shown as black dashed lines.

surement time of 50 msec. Fitting the 500 traces of Figure 6.3**c** individually, we acquire a linewidth of $\kappa_{tot} \approx 2\pi \cdot 15$ MHz. The corrected response of one of these traces, together with a Lorentzian fit is shown in Figure 6.7.

6.6.3. Interchip Distance Estimation

After fabrication of the microwave and membrane chips the flip-chip device was assembled inside a cleanroom, as described in Chapter 3. Due to the small asymmetry is the device, we expect a slight correction in the flip-chip cavity frequency. An adjusted configuration was made in *Ansys HFFS* [170], incorporating the exact misalignment of the metal on the membrane, and with respect to the cavity underneath. As before, the geometry of the phononic shield and the etched membrane were included in the simulation to account for the relative permittivity of the silicon top chip. A top view of the simulation geometry is show in Figure 6.8**a**. The distance between the two chips d was parametrically swept while performing eigenmode simulations. This gives us a corrected model to compare with the measured distance-dependent resonance frequency, as shown in **b**. The misalignments result in a slightly higher cavity frequency for the same distance, as compared to the case of perfect alignment. The simulation data is fit with $\omega_c = \frac{1}{\sqrt{LC_{tot}}}$, where

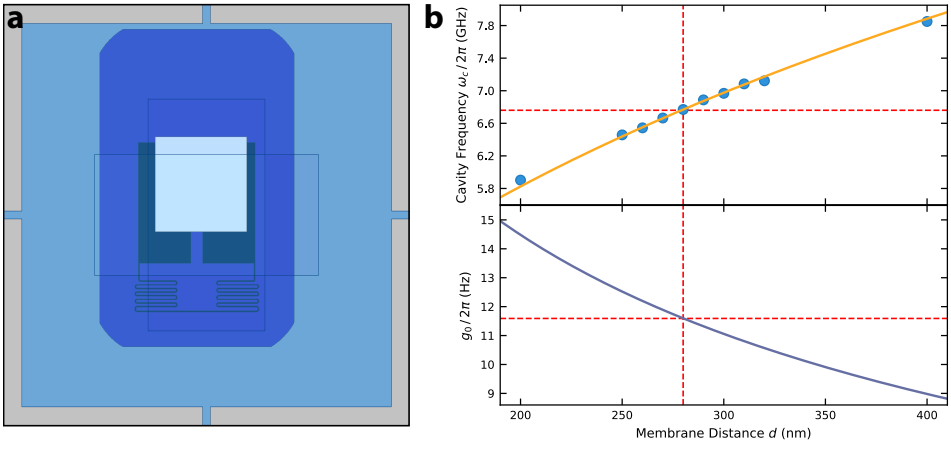


Figure 6.8: Simulated eigenmode and coupling of the flip-chip device for different gap sizes. **a** Top view of the geometry used in the *Ansys HFSS* eigenmode simulation, matching the exact misalignment of the experimental device. The superconducting cavity is shown in black, the ground plane in gray. The superconducting metal on the membrane is visible as the white square, and the silicon phononic shield as the light blue structure. **b** Simulated eigenfrequency of the microwave cavity for a parametric sweep of the distance between the two chips. Simulated frequencies are shown as blue circles, the fit as the orange line. The red dashed lines correspond to the measured frequency and the corresponding gap size of $d \approx 280$ nm. The calculated single photon coupling rate to the membrane is shown in purple. The estimated coupling of the device of $g_0 \approx 2\pi \cdot 11.6$ Hz is shown in red.

C_{tot} includes the misalignment, as described in Chapter 3. The average measured frequency of the flip-chip cavity is $\omega_c = 2\pi \cdot \pm 6.76$ GHz, from which we estimate a distance between the chips of $d \approx 280$ nm, as indicated by the red dashed lines.

Furthermore, we can estimate the optomechanical single photon coupling rate based on the derivative of the found cavity resonance frequency [38].

$$g_0 = G x_{zpf} = \frac{\partial \omega_c}{\partial x} x_{zpf} \tag{6.5}$$

The zero-point fluctuation of the membrane is given by

$$x_{zpf} = \sqrt{\frac{\hbar}{2 m_{eff} \Omega_m}} \tag{6.6}$$

where m_{eff} is the effective mass of the vibrational mode of the membrane [112]. This gives us the dependency on the distance between the two chips $g_0 \propto d^{-3/2}$ and is shown in Figure 6.8**b**. For our device we find an effective mass of $m_{eff} = 7.15$ ng, which implies a zero-point fluctuation of $x_{zpf} = 1.09$ fm. At a distance of $d \approx 280$ nm we estimate a single photon coupling rate of $g_0 \approx 2\pi \cdot 11.6$ Hz.

6.6.4. Signal and Idler Resonances

Applying a drive tone red-detuned from the flip-chip cavity shifts the resonance downwards. The signal and idler resonances appear when the intracavity photon number reaches the bifurcation threshold. The two quasi-modes are located symmetrically around the pump and diverge for increasing occupation. Depending on the detuning and power of the drive tone the signal mode appears as a peak or a dip in the spectrum.

Figure 6.9**a** shows a zoom-in of the dataset discussed in Figure 6.3 with the drive tone $\Delta_d = 2\pi \cdot -68$ MHz detuned. The signal mode appears as a peak after the bifurcation point, indicating sufficient parametric amplification to surpass the internal cavity losses. Lorentzian fits result in a narrowest linewidth of $\kappa_s = 2\pi \cdot 7.6$ MHz and a maximum output gain of 1 dB. Individual line scans at the pump powers indicated by the arrows are shown in **b**, offset for clarity. For lower detunings the signal and idler modes appear at lower drive powers, as more photons from the drive enter the cavity. A measurement with a detuning of $\Delta_d = 2\pi \cdot -25$ MHz and the same probe power is shown in Figure 6.9**cd**. The signal mode emerges as a dip, which transitions to a peak as the drive power is increased. Note that for both measurements the cavity remained in the high-amplitude branch. For both datasets we performed background subtraction with a dataset measured with a minimally tuned magnetic field, such that the flip-chip cavity shifted out of the measurement span without affecting the qubit and readout resonator. Subsequently, the datasets were equally normalized to zero. For the data presented in Figure 6.3**cd** we performed a linear background subtraction. The stabilization of the resonance and the amplification of the intracavity field could be utilized for measurements on the mechanical resonator.

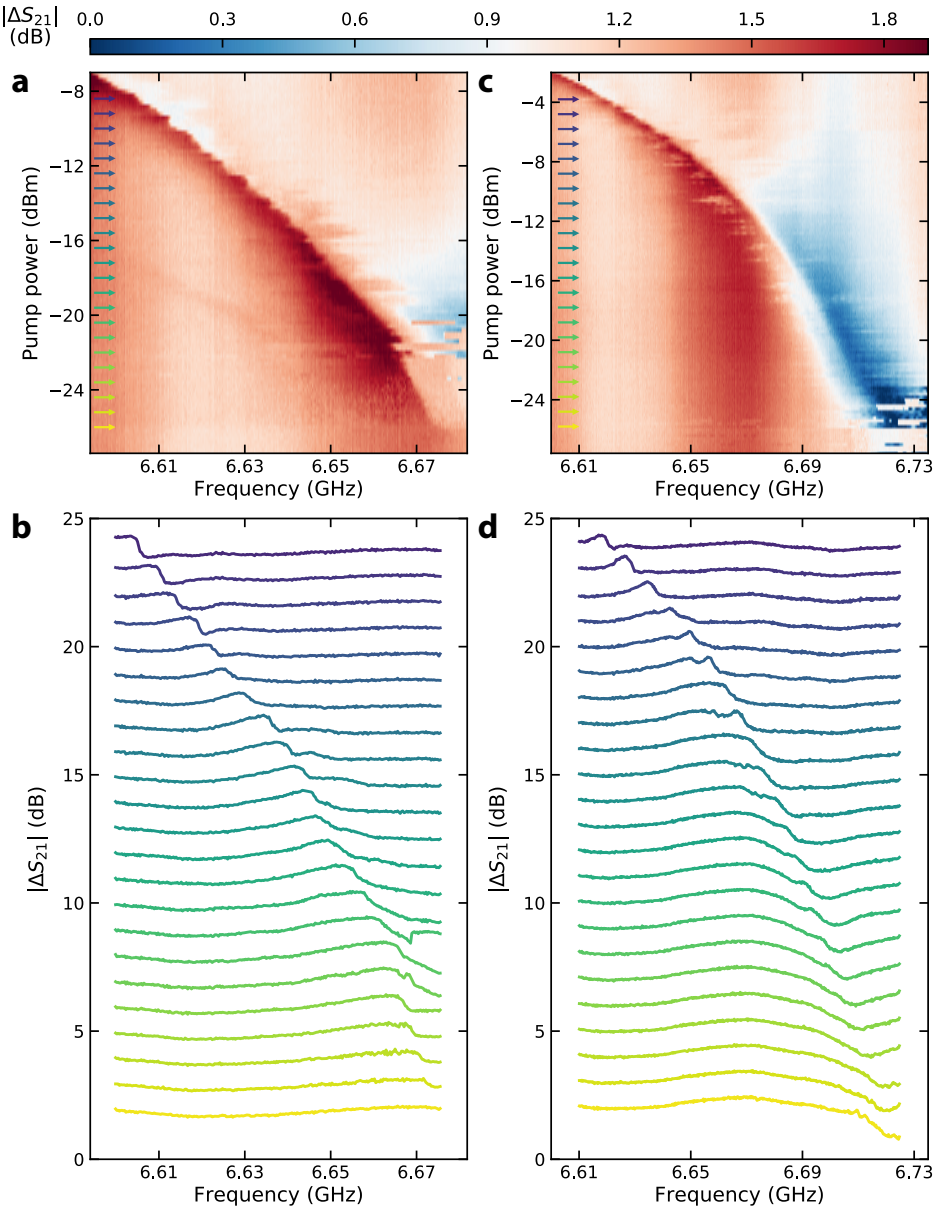


Figure 6.9: Observation of amplification in the signal mode. a Colormap of the magnitude $|\Delta S_{21}|$ response of the signal mode during a two-tone spectroscopy measurement with the a $\Delta_d = 2\pi \cdot -68$ MHz detuning of the drive tone. Pump power is defined at the output of the generator. Line cuts at the arrows are shown in **b** and offset for clarity. The signal mode is visible as a down-shifting peak above the background level, indicating a net output gain of the system. Panels **c** and **d** show the same measurement for a detuning of $\Delta_d = 2\pi \cdot -25$ MHz. A transition of the signal mode from a dip to a peak is observed as the pump power increases.

7

Conclusion & Outlook

In this thesis we presented the development and experimental realization of flip-chip optomechanics, coupling a large high-stress membrane to a superconducting microwave cavity. Several experimental challenges in this field were identified, tackled and discussed in detail, such as decreasing the interchip distance, cavity noise and thermal calibrations. We developed a microwave frequency locking technique by applying real-time feedback, applicable in many fields suffering from cavity noise. Furthermore, we explored linear optomechanical interactions and introduced a first step of the implementation of a qubit in this platform, opening a path towards novel nonlinear optomechanical experiments.

The accomplishments in this work were the results of many iterations in design, simulation, fabrication, cooldowns and measurements of devices. The efforts of targeting the required parameter regime and creation of working devices were extensive, though successful. Crucial improvements were made in the process of flipping the membrane chip, as this is both the core of the device and the most vulnerable process. The result is a reproducible and smooth fabrication and assembly method, as described in **Chapter** 3. Many challenges that occurred during the work in this thesis where of a technical nature, each of them to be solved to reach the experiments presented in **Chapters** 4, 5 and 6.

7.1. Feedback Locking a Noisy Microwave Cavity

In **Chapter** 4 we developed a novel active feedback technique to stabilize a noisy microwave cavity. The dynamic feedback system presented is implemented by the locking of a microwave drive to a fluctuating cavity resonance, based on the inverse of the Pound-Drever-Hall technique. A homodyne interferometer scheme monitored the real-time resonance fluctuations due to low-frequency noise, which was mitigated by frequency-modulating (FM) the microwave generator. This resulted in an effective high-pass filter. We discussed how to optimize the feedback system for a specific setup, and characterize the bandwidth and performance of the filter. This feedback scheme provides continual scaling for adding tones to the same lock by multiplexing generators and mixers after the local oscillator, allowing for locked multitone experiments. With a second tone we quantitatively analyzed the effective narrowing and stabilization of the cavity. Finally, we demonstrated the feedback system's applicability in experiments with a cavity-locked, multitone mechanical measurement. A third locked drive was applied to the red sideband of the optomechanical cavity, after which optomechanically induced transparency (OMIT) was observed.

Initially, the cavity noise occurred as an unexpected detrimental effect for our experiments, before we learned that this is indeed a limiting factor in a wide range of systems. Besides optomechanics [76, 77], the feedback system presented here has applications in various fields, as any source of low-frequency cavity noise can be reduced. For example, other potential applications include reducing two-level system (TLS) noise [78], locking to coplanar waveguide resonators [79], and stabilizing SQUID cavities [80], either by applying the feedback on the generator or

by modulating the magnetic flux. Furthermore, this scheme could be applied in gravitational wave detectors [81], axion dark-matter detectors [82], and magnomechanical experiments [83–86].

7.2. Linear and Nonlinear Flip-Chip Devices

In **Chapter** 5 we presented the optomechanical flip-chip platform used for the measurement and manipulation of a high-Q mechanical mode in a silicon nitride membrane. The metallized membrane, located in an in-substrate phononic shield, is coupled to a superconducting microwave cavity. Installed on a vibration isolation system, we bring the system into the sideband-resolved regime. Applying a strong red sideband drive, the energy transfer from the mechanical resonator to the cavity was enhanced, increasing the multi-photon coupling rate. OMIT was observed with a large cooperativity. Reducing the drive power, we find the high intrinsic quality factor and narrow linewidth of the mechanical resonator. We performed spectroscopy of the motional sideband to measure the thermal noise of the mechanical mode and observed its thermalization to the cryostat. We discussed the subtleties and assumptions necessary for the conversion of the measured voltage power spectral density to a mechanical displacement. Hereby, shedding light on a general quantitative calibration procedure for the mode temperature. We introduced a multitone sideband cooling scheme to enhance the signal of the mechanical noise. Cooling of membrane mode close to the ground state was observed, reducing our measured signal to a fraction of its thermalized value.

In **Chapter** 6 we presented a platform for flux-tunable nonlinear flip-chip optomechanical experiments. A superconducting lumped element microwave cavity was coupled to a high-Q membrane mode. Improvements in the flip-chip holder enabled us to reliably create distances of a few hundred nm between the two chips, which will increase the single photon coupling rate by an order of magnitude. A transmon qubit was coupled via its dipole moment to the flip-chip cavity, inducing a self-Kerr nonlinearity in the cavity. Additionally, a coplanar waveguide readout resonator was coupled to the qubit. We characterized the dispersive couplings using single-tone spectroscopy, where we observed the AC Stark shift. Furthermore, by sweeping the magnetic field threaded through the SQUID of the qubit we were able to tune the qubit closer to the resonators, in which we observed a frequency shift. Consequently, this created a flux-tunable self-Kerr nonlinearity in the cavity. Finally, a second microwave tone was placed red-detuned from the cavity. Increasing its power brought the cavity to its bifurcation point, where a sudden transition took place to form signal and idler resonances, symmetric around the drive. The cavity mode was more susceptible to vibrational noise due to the smaller gap size, causing the resonance the fluctuate. However, due to a four-wave mixing process, these quasi-modes were stabilized by an internal feedback mechanism called Kerr locking. Thereby cavity noise was removed, and amplification of the input field observed. This provides a promising platform for nonlinear optomechanical experiments.

The optomechanical experiments in this thesis have two main limiting factors. Firstly, the temperature dependence of the attenuation and impedance of the flexible microwave cables prevented an exact calibration of the measured signal to a mechanical displacement. Carefully calibrating the drive and return lines in the cryostat would make this possible. Secondly, since smaller interchip distances can be obtained in the flip-chip device, the cavity becomes more prone to vibrational noise. Besides exploiting a designed Kerr nonlinearity in the microwave cavity, the implementation of a multi-stage vibration isolation system, or of the dynamic feedback to lock to the noisy cavity would narrow the resonance linewidth and allow for more accuracy in designing the cavity decay rates [229, 240, 268]. These feedback methods would also help reducing magnetic flux noise picked up by the SQUID of the qubit.

7.3. Future Nonlinear Optomechanical Experiments

The application of a nonlinear cavity in optomechanical experiments is still mostly unexplored. However, the results presented to date show promising directions, both in the good- and the bad-cavity limit. For example, Kerr optomechanics could be used for intracavity squeezing [100, 296, 297, 304, 305] or quantum transduction [298, 299]. Recently, a mechanical resonator was cooled in a magnetomechanical system using Kerr-enhanced backaction [101, 102, 306]. Four-wave mixing processes have been used to ground state cool a mechanical resonator [97]. Furthermore, the signal and idler resonances can be used to better detect and manipulate mechanical motion. In other systems involving these quasi-modes, level attraction was observed, where exceptional points where found [271, 300–303].

Moreover, coupling an optomechanical cavity to a qubit has been proposed as a platform to prepare mechanical quantum states [87–91, 307], as well as coupling a qubit to the mechanics directly [75]. However, these methods require strong sideband drives to first cool the mechanical resonator to or close to its ground state, which is incompatible with the limited critical photon number in Kerr cavities [36]. In recent work a superconducting qubit was longitudinally coupled to a linear resonator analogous to the radiation-pressure interaction in optomechanical systems [107]. Integration of a similar coupling in an existing optomechanical platform, such as the flip-chip device in this work, would allow for a dynamical modulation of the coupling to the qubit. The large critical photon number would enable strong drives in the linear circuit to cool the mechanical resonator. This combined system has been proposed to prepare Schrödinger cat states in the linear resonator, which could be swapped into the mechanical resonator via a beam-splitter interaction pulse [88, 107, 108]. This would provide a platform to generate and control massive, macroscopic superpositions to test gravitational decoherence [61–63].

Acknowledgements

I am only where I am because of the help of others. Over the years of this PhD many things have happened, more than I can tell here. Some moments were amazing, some were harder. But every one of those moments was with the support of these wonderful people.

First and foremost, I would like to thank **Gary**. For all the support over the years. Being in your group for the last five years has been a great experience. I couldn't have asked for a better supervisor, you've thought me many things and have guided me in the right direction when needed. The energy and enthusiasm that you bring, on any physics or non-physics related topic, is simply contagious. I truly loved discussing all these topics with you, and even when we disagree we always manage to keep things respectful and productive. I would also like to stress my appreciation for your support in my personal life. Being able to move to Zürich to start a family while working remotely was not a small thing to ask. Putting effort into keeping the communication lines open, and some helping hands to change a cable in the setup every now and then, really made this work. Our conversations talking about kids and parenting that keep happening between meetings are a lot of fun. Thank you for being the mentor you've been, always available, open for discussion, and also happy to just have a laugh.

Secondly, a big thanks to **Simon** for being my second promotor. The discussions we had from time to time often gave rise to new ideas. Keeping focused on the important goals can be hard when trying to solve an almost infinite number of very detailed problems. Your fresh perspective was very much appreciated.

Inês, you mean the world to me. What started as colleagues grew into friends, and finally a family. You have supported me on this journey in many ways. You were there emotionally whenever I didn't see how to move forward. But it was also tremendously helpful to ask you extremely specific details about measurements or fabrication. Going back and forth between countries was hard, and when we were together we still wanted to do our best in our work. Then I moved in with you in Zürich and it was basically nonstop fun. It's been nothing but wonderful and I would do it all over again. I'd like to end the same way you did in your thesis, with the words you wrote to me: I wish you the best of luck in your future.

Clinton, you were maybe the biggest surprise of all. I remember when you came for your interview and I made quite some free time for discussions, as I could really use the extra hands. But you were more than just extra hands. Your input quickly became invaluable, one of the driving forces behind the project. Plainly, I loved

our time working together. But we also immediately became good friends and had a lot of good times in and out of the department. And I keep laughing about the not even slightly appropriate stuff we send each other every day. And you're even flying over for the role of paranymph on your birthday, thank you so much.

Jasper, my paranymph, from the very first day of my application to the group we clicked. I remember us going for a drink at the Hangout after, me still being nervous not to come across as being stupid. Working both on the optomechanical side of the group made it easy to discuss these topics over all our coffee and lunch breaks. Furthermore, seeing you struggle at times and tackling the challenges head-on, somehow made my own struggles more bearable. Sometimes, when it felt like having to solve all the problems alone, it was great to feel your support. I hope I gave you as much as you gave me. All the times we went for drinks or dinner after work has made my time here amazing. And hearing the details about becoming a dad right after I became one myself has been a lot of fun. See you and Emma soon when I come to hang out again with Emily.

Next is of course my buddy **Jacob**. I don't think I've ever met someone capable of working as hard as you did. Whenever I felt like being stuck, your perseverance often convinced me to not give up. Our research topics only overlapped slightly, but it was great to discuss and complain about things to each other. And although busy, you were always up for going for a drink or two, always leading to very late and fun nights. The funniest maybe being us opening your bike lock with an angle grinder, or the endless Shrek videos. Say hi to **Riko** for me, our favorite babysitter in the world.

Sarwan, following you up in project membranes was a huge advantage. You've patiently thought me all your fabrication knowledge and, even more important, your cleanroom skills. This gave me an incredible head start for making the devices that are so difficult to fabricate. But we also had many laughs. During our chats in the end of the afternoons you often gave your original view on any random topic that came by.

Adrián, when I joined team membranes you were always measuring in the lab. You have an amazing critical eye for all the details involved in a project, and will work hard to understand the entire system. I definitely learned from you to not take anything for granted. I enjoyed working together a lot, although we never managed to sync our lunch schedules.

Robin, you joined the group as the one after me. Over the years I've seen you work on many projects and I'm convinced you're one of the best in fab in the group. You were always available for a quick chat or to lend a helping hand. In short, I found it always super gezellig. Good luck with writing the thesis!

Sercan, I want to say a big thank you to you. No matter how busy you were, you were always happy to help out. Be it in the cleanroom, in the lab, or by dis-

cussing measurements, you were there. I've seen you going from a master student to your PhD and I think you're doing great work. You were also there whenever I burst into the lab for a short break to put my mind off things. Always a lot of fun.

Of course there's also **Matteo**. From the very start of your master's project in the group we were always making fun of each other. I imagine other people hearing these jokes thinking these were pretty harsh. But besides the countless insults you are putting in some serious work. I am still amazed by your persistence in the cleanroom. I'm sure you'll get great results with your drums.

Sarah, the beginning of your master's project was when I was away in Zürich. Your help was very much appreciated, by continuing the work on site when I couldn't. It's great that you stayed for a PhD and it's fantastic that you'll continue project membranes. Although there are many moving parts and choices to make at the moment, the next cool experiment is waiting around the corner.

Gopika and **Chandan**, although we didn't have much time, I did really enjoy working together. When you joined the project things became more efficient and we were able to run things faster. All the best!

Tommy and **Marius**, although we have not yet worked together that much, it's been great since you guys joined the group. It's nice to see the points of view and experience both of you bring and I'm convinced there's gonna be some great results on all the different projects soon.

Niek, you were the student I spent the most time together with. For some time we were the only two on project membranes, when we were desperately trying to improve the flip-chip technique. Your motivation was great addition and I really enjoyed trying to come up with solutions to every problem we ran into together. Good luck in Singapore!.

To all the other students I've supervised **Cees**, **Jonathan**, **Timo**, **Luka**, **Luuk** and **Martin**, I want to thank you too. I think I learned as much as you all did during these times. We had a lot of fun and did managed to do a lot of stuff. Good luck with your next steps!

Ronald, **Nico** and **Tim**, without your help my project would have looked very different. You always did your best to make time for any design or manufacturing of all the iterations of the parts needed. Especially the flip-chip holder we really understand now and we were able to optimize it to the point where I was able to get these great results. Thank you for all the help.

Raymond, I would like to say thanks for answering my electronics questions whenever I was stuck. I definitely have a better understanding now. **Tino**, thanks for keeping the labs running the way they do. Let's hope we don't have to fix any water-related problems any more. **Kees** and **Yannick**, thanks for helping out

with the PCBs, wires and other components, and teaching me some very useful tricks. **Allard**, you were a great help with the interferometer. But even more with the discussions we had on any technical topic as an office mate.

I want to give a special thanks to the KN staff, **Marc**, **Eugene**, **Charles**, **Bas**, **Pauline**, **Brian**, **Marinus**, **Marco**, **Anja**, **Arnold**, **Hozanna**, **Lodi** and **Roald**. For all the training and support in the cleanroom. You guys are the driving force behind countless projects.

Voor mijn **familie**, enorm bedankt dat jullie mij altijd bijstonden. Met jullie hulp kon ik zo makkelijk eerst naar Leiden voor mijn studie en daarna naar Delft. De laatste vijf jaar was er volgens mij geen dag dat ik jullie zag waarop ik niet eindeloos over mijn werk doorpraatte. En toch was het nooit te veel. Op de zwaarste momenten was het jullie steun wat mij erdoorheen hielp. Daar zal ik altijd dankbaar voor zijn.

To my friends, **Noud**, **Evert**, **Arianne**, **Jaimy**, **Sonakshi**, **Victoria**, **Gijs**, **Hans**, **Amber**, **Massi**, **Steven**, **Itziar**, **Parsa**, **Hugo**, **Luigi**, **Rodrigo**, **Dennis**, **Marc**, **Letizia**, **Andries**, **Loek**, **Yu**, **Samer**, **Marijn**, **Álvaro**, **Gesa**, **Uwe**, **Marc**, **Max**, **Tess**, **Marius**, **Onima**, **Martijn**, **Simone**, **Yolanda**, **Jels**, **Maurits**. Every one of you is following their own journey, and I am grateful to be part of it the same way you are part of mine.

Delft
31-10-2025

Curriculum Vitæ

Jean-Paul van Soest

04-11-1996 Born in Zaanstad, the Netherlands.

Education

2009–2015 Secondary School
Zaanlands Lyceum, Zaandam, the Netherlands

2015–2018 BSc in Physics
Leiden University, Leiden, the Netherlands

Thesis: Optical and Electronic Reflectivity of TaS_2
Supervisor: Prof.dr. S.J. van der Molen

2018–2020 MSc in Physics Research: Quantum Matter and Optics,
Leiden University, Leiden, the Netherlands

Thesis: Fabrication and Magnetisation of Electrochemically Etched Nickel Tips for Spin-Polarised STM
Supervisor: Prof.dr. J.M. van Ruitenbeek

Thesis: Meissner Levitated Magnetic Microparticle
Supervisor: Prof.dr.ir. T.H. Oosterkamp

2020-2025 PhD in Physics
Delft University of Technology, Delft, the Netherlands

Thesis: Flip-Chip Optomechanics: Cooling Mechanics and Mitigating Noise with Feedback and Nonlinearity
Promotors: Prof.dr. G. A. Steele & Prof.dr. S. Gröblacher

List of Publications

4. **J.P. van Soest**, G.L. Bhai, S. Meilof, M. Villiers, C.A. Potts, and G.A. Steele, *Suppressing Cavity Frequency Noise Using a Kerr Nonlinearity*, *in preparation* (2025)

3. **J.P. van Soest**, C.A. Potts, S. Peiter, A. Sanz Mora, and G.A. Steele, *Subtleties in Optomechanical Sideband Cooling and Calibration of a Mechanical Resonator*, *in preparation* (2025)

2. T.M. Fuchs, D.G. Uitenbroek, J. Plugge, N. van Halteren, **J.P. van Soest**, A. Vinante, H. Ulbricht, and T.H. Oosterkamp, *Measuring Gravity with Milligram Levitated Masses*, *Sci. Adv.* **10**, eadk2949 (2024)

1. **J.P. van Soest**, C.A. Potts, S. Peiter, A. Sanz Mora, and G.A. Steele, *Multitone Microwave Frequency Locking to a Noisy Cavity via Real-Time Feedback*, *Phys. Rev. Appl.* **20**, 034007 (2023)

The titles and author lists of the above articles in preparation are subject to change prior to publication.

Bibliography

[1] O. Mori *et al.* First Solar Power Sail Demonstration by IKAROS. *Transactions of the Japan Society for Aeronautical and Space Sciences* **8**, 4.25–4.31 (2010). Link

[2] C. L. Degen, F. Reinhard, and P. Cappellaro. Quantum sensing. *Rev. Mod. Phys.* **89**, 035002 (2017). Link

[3] S. Barzanjeh, A. Xuereb, S. Gröblacher, M. Paternostro, C. A. Regal, and E. M. Weig. Optomechanics for quantum technologies. *Nature Physics* **18**, 15–24 (2022). Link

[4] L. Norder *et al.* Pentagonal photonic crystal mirrors: scalable lightsails with enhanced acceleration via neural topology optimization. *Nature Communications* **16**, 2753 (2025). Link

[5] J. Kepler. De cometis libelli tres. (1619). Link

[6] J. Maxwell. On physical lines of force. *Philosophical Magazine* **90**, 11–23 (2010). Link

[7] P. Lebedew. Untersuchungen über die Druckkräfte des Lichtes. *Annalen der Physik* **311**, 433–458 (1901). Link

[8] E. F. Nichols and G. F. Hull. A Preliminary Communication on the Pressure of Heat and Light Radiation. *Phys. Rev. (Series I)* **13**, 307–320 (1901). Link

[9] A. Einstein. On the Present Status of the Radiation Problem. *Physikalische Zeitschrift* (1909). Link

[10] A. Ashkin. Acceleration and Trapping of Particles by Radiation Pressure. *Phys. Rev. Lett.* **24**, 156–159 (1970). Link

[11] A. Ashkin. Trapping of Atoms by Resonance Radiation Pressure. *Phys. Rev. Lett.* **40**, 729–732 (1978). Link

[12] V. Braginskiĭ and A. Manukin. Ponderomotive effects of electromagnetic radiation. *Soviet Journal of Experimental and Theoretical Physics* **25**, 653–655 (1967). Link

[13] V. Braginskiĭ, A. Manukin, and M. Tikhonov. Investigation of dissipative ponderomotive effects of electromagnetic radiation. *Soviet Journal of Experimental and Theoretical Physics* **31**, 829 (1970). Link

[14] V. Braginskiĭ and A. Manukin. Measurement of weak forces in physics experiments. (1977). Link

[15] C. M. Caves. Quantum-Mechanical Radiation-Pressure Fluctuations in an Interferometer. *Phys. Rev. Lett.* **45**, 75–79 (1980). Link

[16] A. F. Pace, M. J. Collett, and D. F. Walls. Quantum limits in interferometric detection of gravitational radiation. *Phys. Rev. A* **47**, 3173–3189 (1993). Link

[17] T. Kippenberg and K. Vahala. Cavity Opto-Mechanics. *Opt. Express* **15**, 17172–17205 (2007). Link

[18] K. W. Murch, K. L. Moore, S. Gupta, and D. M. Stamper-Kurn. Observation of quantum-measurement backaction with an ultracold atomic gas. *Nature Physics* **4**, 561–564 (2008). Link

[19] M. Eichenfield, R. Camacho, J. Chan, K. J. Vahala, and O. Painter. A picogram- and nanometre-scale photonic-crystal optomechanical cavity. *Nature* **459**, 550–555 (2009). Link

[20] J. Aasi *et al.* Advanced LIGO. *Classical and Quantum Gravity* **32**, 074001 (2015). Link

[21] T. Carmon, H. Rokhsari, L. Yang, T. J. Kippenberg, and K. J. Vahala. Temporal Behavior of Radiation-Pressure-Induced Vibrations of an Optical Microcavity Phonon Mode. *Phys. Rev. Lett.* **94**, 223902 (2005). Link

[22] A. Schliesser, P. Del'Haye, N. Nooshi, K. J. Vahala, and T. J. Kippenberg. Radiation Pressure Cooling of a Micromechanical Oscillator Using Dynamical Backaction. *Phys. Rev. Lett.* **97**, 243905 (2006). Link

[23] R. Rivière *et al.* Optomechanical sideband cooling of a micromechanical oscillator close to the quantum ground state. *Phys. Rev. A* **83**, 063835 (2011). Link

[24] E. Verhagen, S. Deléglise, S. Weis, A. Schliesser, and T. J. Kippenberg. Quantum-coherent coupling of a mechanical oscillator to an optical cavity mode. *Nature* **482**, 63–67 (2012). Link

[25] O. Arcizet, P.-F. Cohadon, T. Briant, M. Pinard, and A. Heidmann. Radiation-pressure cooling and optomechanical instability of a micromirror. *Nature* **444**, 71–74 (2006). Link

[26] S. Gigan *et al.* Self-cooling of a micromirror by radiation pressure. *Nature* **444**, 67–70 (2006). Link

[27] J. D. Thompson, B. M. Zwickl, A. M. Jayich, F. Marquardt, S. M. Girvin, and J. G. E. Harris. Strong dispersive coupling of a high-finesse cavity to a micromechanical membrane. *Nature* **452**, 72–75 (2008). Link

[28] I. Favero *et al.* Fluctuating nanomechanical system in a high finesse optical microcavity. *Opt. Express* **17**, 12813–12820 (2009). Link

[29] X. Jiang, Q. Lin, J. Rosenberg, K. Vahala, and O. Painter. High-Q double-disk microcavities for cavity optomechanics. *Opt. Express* **17**, 20911–20919 (2009). Link

[30] G. S. Wiederhecker, L. Chen, A. Gondarenko, and M. Lipson. Controlling photonic structures using optical forces. *Nature* **462**, 633–636 (2009). Link

[31] A. Schliesser. Cavity Optomechanics and Optical Frequency Comb Generation with Silica Whispering-Gallery-Mode Microresonators. *PhD thesis*. Ludwig Maximilian University of Munich (2009). Link

[32] R. Ma, A. Schliesser, P. Del'Haye, A. Dabirian, G. Anetsberger, and T. J. Kippenberg. Radiation-pressure-driven vibrational modes in ultrahigh-Q silica microspheres. *Opt. Lett.* **32**, 2200–2202 (2007). Link

[33] F. Brennecke, S. Ritter, T. Donner, and T. Esslinger. Cavity Optomechanics with a Bose-Einstein Condensate. *Science* **322**, 235–238 (2008). Link

[34] H. M. Doeleman, T. Schatteburg, R. Benevides, S. Vollenweider, D. Macri, and Y. Chu. Brillouin optomechanics in the quantum ground state. *Phys. Rev. Res.* **5**, 043140 (2023). Link

[35] B. P. Abbott *et al.* Observation of Gravitational Waves from a Binary Black Hole Merger. *Phys. Rev. Lett.* **116**, 061102 (2016). Link

[36] J. D. Teufel *et al.* Sideband cooling of micromechanical motion to the quantum ground state. *Nature* **475**, 359–363 (2011). Link

[37] J. Chan *et al.* Laser cooling of a nanomechanical oscillator into its quantum ground state. *Nature* **478**, 89–92 (2011). Link

[38] M. Aspelmeyer, T. J. Kippenberg, and F. Marquardt. Cavity optomechanics. *Rev. Mod. Phys.* **86**, 1391–1452 (2014). Link

[39] A. Blais, A. L. Grimsmo, S. M. Girvin, and A. Wallraff. Circuit quantum electrodynamics. *Rev. Mod. Phys.* **93**, 025005 (2021). Link

[40] C. A. Regal, J. D. Teufel, and K. W. Lehnert. Measuring nanomechanical motion with a microwave cavity interferometer. *Nature Physics* **4**, 555–560 (2008). Link

[41] A. D. O'Connell *et al.* Quantum ground state and single-phonon control of a mechanical resonator. *Nature* **464**, 697–703 (2010). Link

[42] Y. Chu *et al.* Quantum acoustics with superconducting qubits. *Science* **358**, 199–202 (2017). Link

[43] J. D. Teufel, T. Donner, M. A. Castellanos-Beltran, J. W. Harlow, and K. W. Lehnert. Nanomechanical motion measured with an imprecision below that at the standard quantum limit. *Nature Nanotechnology* **4**, 820–823 (2009). Link

[44] J. D. Teufel *et al.* Circuit cavity electromechanics in the strong-coupling regime. *Nature* **471**, 204–208 (2011). Link

[45] E. E. Wollman *et al.* Quantum squeezing of motion in a mechanical resonator. *Science* **349**, 952–955 (2015). Link

[46] J.-M. Pirkkalainen, E. Damskägg, M. Brandt, F. Massel, and M. A. Sillanpää. Squeezing of Quantum Noise of Motion in a Micromechanical Resonator. *Phys. Rev. Lett.* **115**, 243601 (2015). Link

[47] S. Kotler *et al.* Direct observation of deterministic macroscopic entanglement. *Science* **372**, 622–625 (2021). Link

[48] T. Bagci *et al.* Optical detection of radio waves through a nanomechanical transducer. *Nature* **507**, 81–85 (2014). Link

[49] R. A. Barton *et al.* Photothermal Self-Oscillation and Laser Cooling of Graphene Optomechanical Systems. *Nano Letters* **12**, 4681–4686 (2012). Link

[50] R. J. Dolleman *et al.* Optomechanics for thermal characterization of suspended graphene. *Phys. Rev. B* **96**, 165421 (2017). Link

[51] R. W. Andrews *et al.* Bidirectional and efficient conversion between microwave and optical light. *Nature Physics* **10**, 321–326 (2014). Link

[52] L. Diósi. A universal master equation for the gravitational violation of quantum mechanics. *Physics Letters A* **120**, 377–381 (1987). Link

[53] R. Penrose. On Gravity's role in Quantum State Reduction. *General Relativity and Gravitation* **28**, 581–600 (1996). Link

[54] A. Bassi, K. Lochan, S. Satin, T. P. Singh, and H. Ulbricht. Models of wave-function collapse, underlying theories, and experimental tests. *Rev. Mod. Phys.* **85**, 471–527 (2013). Link

[55] R. C. Ritter, C. E. Goldblum, W.-T. Ni, G. T. Gillies, and C. C. Speake. Experimental test of equivalence principle with polarized masses. *Phys. Rev. D* **42**, 977–991 (1990). Link

[56] J. Schmöle, M. Dragosits, H. Hepach, and M. Aspelmeyer. A micromechanical proof-of-principle experiment for measuring the gravitational force of milligram masses. *Classical and Quantum Gravity* **33**, 125031 (2016). Link

[57] Y. Liu, J. Mummery, J. Zhou, and M. A. Sillanpää. Gravitational Forces Between Nonclassical Mechanical Oscillators. *Phys. Rev. Appl.* **15**, 034004 (2021). Link

[58] T. M. Fuchs *et al.* Measuring gravity with milligram levitated masses. *Science Advances* **10**, eadk2949 (2024). Link

[59] R. Penrose. On the Gravitization of Quantum Mechanics 1: Quantum State Reduction. *Foundations of Physics* **44**, 557–575 (2014). Link

[60] A. Bassi, A. Großardt, and H. Ulbricht. Gravitational decoherence. *Classical and Quantum Gravity* **34**, 193002 (2017). Link

[61] W. Marshall, C. Simon, R. Penrose, and D. Bouwmeester. Towards Quantum Superpositions of a Mirror. *Phys. Rev. Lett.* **91**, 130401 (2003). Link

[62] M. Bahrami, M. Paternostro, A. Bassi, and H. Ulbricht. Proposal for a Noninterferometric Test of Collapse Models in Optomechanical Systems. *Phys. Rev. Lett.* **112**, 210404 (2014). Link

[63] M. F. Gely and G. A. Steele. Superconducting electro-mechanics to test Diósi–Penrose effects of general relativity in massive superpositions. *AVS Quantum Science* **3**, 035601 (2021). Link

[64] R. W. Andrews. Quantum Signal Processing with Mechanical Oscillators. *PhD thesis*. University of Colorado (2015). Link

[65] M. Yuan, V. Singh, Y. M. Blanter, and G. A. Steele. Large cooperativity and microkelvin cooling with a three-dimensional optomechanical cavity. *Nature Communications* **6**, (2015). Link

[66] M. Yuan, M. A. Cohen, and G. A. Steele. Silicon nitride membrane resonators at millikelvin temperatures with quality factors exceeding 10^8. *Applied Physics Letters* **107**, 263501 (2015). Link

[67] A. Noguchi *et al.* Ground state cooling of a quantum electromechanical system with a silicon nitride membrane in a 3D loop-gap cavity. *New J. Phys.* **18**, 103036 (2016). Link

[68] A. P. Higginbotham *et al.* Harnessing electro-optic correlations in an efficient mechanical converter. *Nature Physics* **14**, 1038–1042 (2018). Link

[69] Y. Seis. Ultra-Coherent Electro-Mechanics in the Quantum Regime. *PhD thesis*. University of Copenhagen (2021). Link

[70] Y. Seis, T. Capelle, E. Langman, S. Saarinen, E. Planz, and A. Schliesser. Ground state cooling of an ultracoherent electromechanical system. *Nature Communications* **13**, 1507 (2022). Link

[71] S. R. Peiter. Cavity electromechanics using flipped silicon nitride membranes. *PhD thesis*. Delft University of Technology (2022). Link

[72] B. M. Brubaker *et al.* Optomechanical Ground-State Cooling in a Continuous and Efficient Electro-Optic Transducer. *Phys. Rev. X* **12**, 021062 (2022). Link

[73] R. D. Delaney *et al.* Superconducting-qubit readout via low-backaction electro-optic transduction. *Nature* **606**, 489–493 (2022). Link

[74] Y. Liu, J. Zhou, L. Mercier de Lépinay, and M. A. Sillanpää. Quantum backaction evading measurements of a silicon nitride membrane resonator. *New Journal of Physics* **24**, 083043 (2022). Link

[75] K. Gerashchenko *et al.* Probing the quantum motion of a macroscopic mechanical oscillator with a radio-frequency superconducting qubit. (2025). Link

[76] J. D. Teufel, F. Lecocq, and R. W. Simmonds. Overwhelming Thermomechanical Motion with Microwave Radiation Pressure Shot Noise. *Phys. Rev. Lett.* **116**, 013602 (2016). Link

[77] J. Suh, A. J. Weinstein, and K. C. Schwab. Optomechanical effects of two-level systems in a back-action evading measurement of micro-mechanical motion. *Appl. Phys. Lett.* **103**, 052604 (2013). Link

[78] T. Lindström, J. Burnett, M. Oxborrow, and A. Y. Tzalenchuk. Pound-locking for characterization of superconducting microresonators. *Review of Scientific Instruments* **82**, (2011). Link

[79] J. Gao, J. Zmuidzinas, B. A. Mazin, H. G. Leduc, and P. K. Day. Noise properties of superconducting coplanar waveguide microwave resonators. *Applied Physics Letters* **90**, (2007). Link

[80] D. Bothner, I. C. Rodrigues, and G. A. Steele. Photon-pressure strong coupling between two superconducting circuits. *Nature Physics* **17**, 85–91 (2021). Link

[81] V. Vadakkumbatt, M. Hirschel, J. Manley, T. J. Clark, S. Singh, and J. P. Davis. Prototype superfluid gravitational wave detector. *Phys. Rev. D* **104**, 082001 (2021). Link

[82] R. Khatiwada *et al.* Axion dark matter experiment: Detailed design and operations. *Rev. Sci. Instrum.* **92**, 124502 (2021). Link

[83] C. A. Potts, E. Varga, V. A. S. V. Bittencourt, S. Viola-Kusminskiy, and J. P. Davis. Dynamical backaction magnomechanics. *Phys. Rev. X* **11**, 031053 (2021). Link

[84] C. A. Potts, Y. Huang, V. A. S. V. Bittencourt, S. Viola Kusminskiy, and J. P. Davis. Dynamical backaction evading magnomechanics. *Phys. Rev. B* **107**, L140405 (2023). Link

[85] X. Zhang, C.-L. Zou, L. Jiang, and H. X. Tang. Cavity magnomechanics. *Sci. Adv.* **2**, e1501286 (2016). Link

[86] R.-C. Shen, J. Li, Z.-Y. Fan, Y.-P. Wang, and J. Q. You. Mechanical bistability in kerr-modified cavity magnomechanics. *Phys. Rev. Lett.* **129**, 123601 (2022). Link

[87] K. E. Khosla, M. R. Vanner, N. Ares, and E. A. Laird. Displacemon Electromechanics: How to Detect Quantum Interference in a Nanomechanical Resonator. *Phys. Rev. X* **8**, 021052 (2018). Link

[88] V. Bergholm, W. Wieczorek, T. Schulte-Herbrüggen, and M. Keyl. Optimal control of hybrid optomechanical systems for generating non-classical states

of mechanical motion. *Quantum Science and Technology* **4**, 034001 (2019). Link

[89] M. Kounalakis, Y. M. Blanter, and G. A. Steele. Synthesizing multi-phonon quantum superposition states using flux-mediated three-body interactions with superconducting qubits. *npj Quantum Information* **5**, 100 (2019). Link

[90] M. Kounalakis, Y. M. Blanter, and G. A. Steele. Flux-mediated optomechanics with a transmon qubit in the single-photon ultrastrong-coupling regime. *Phys. Rev. Res.* **2**, 023335 (2020). Link

[91] B. D. Hauer, J. Combes, and J. D. Teufel. Nonlinear Sideband Cooling to a Cat State of Motion. *Phys. Rev. Lett.* **130**, 213604 (2023). Link

[92] P. Schmidt *et al.* Ultrawide-range photon number calibration using a hybrid system combining nano-electromechanics and superconducting circuit quantum electrodynamics. *Applied Physics Letters* **113**, 152601 (2018). Link

[93] I. C. Rodrigues, D. Bothner, and G. A. Steele. Coupling microwave photons to a mechanical resonator using quantum interference. *Nature Communications* **10**, 5359 (2019). Link

[94] D. Zoepfl, M. L. Juan, C. M. F. Schneider, and G. Kirchmair. Single-Photon Cooling in Microwave Magnetomechanics. *Phys. Rev. Lett.* **125**, 023601 (2020). Link

[95] P. Schmidt *et al.* Sideband-resolved resonator electromechanics based on a nonlinear Josephson inductance probed on the single-photon level. *Communications Physics* **3**, 233 (2020). Link

[96] I. C. Rodrigues. Coupling Harmonic Oscillators to Superconducting Quantum Interference Cavities. *PhD thesis*. Delft University of Technology (2021). Link

[97] D. Bothner, I. C. Rodrigues, and G. A. Steele. Four-wave-cooling to the single phonon level in Kerr optomechanics. *Communications Physics* **5**, 33 (2022). Link

[98] P. D. Nation, M. P. Blencowe, and E. Buks. Quantum analysis of a nonlinear microwave cavity-embedded dc SQUID displacement detector. *Phys. Rev. B* **78**, 104516 (2008). Link

[99] H.-K. Lau and A. A. Clerk. Ground-State Cooling and High-Fidelity Quantum Transduction via Parametrically Driven Bad-Cavity Optomechanics. *Phys. Rev. Lett.* **124**, 103602 (2020). Link

[100] J. Monsel *et al.* Optomechanical cooling with coherent and squeezed light: The thermodynamic cost of opening the heat valve. *Phys. Rev. A* **103**, 063519 (2021). Link

[101] D. Zoepfl *et al.* Kerr Enhanced Backaction Cooling in Magnetomechanics. *Phys. Rev. Lett.* **130**, 033601 (2023). Link

[102] N. Diaz-Naufal *et al.* Kerr-enhanced optomechanical cooling in the unresolved-sideband regime. *Phys. Rev. A* **111**, 053505 (2025). Link

[103] G. A. Brawley, M. R. Vanner, P. E. Larsen, S. Schmid, A. Boisen, and W. P. Bowen. Nonlinear optomechanical measurement of mechanical motion. *Nature Communications* **7**, 10988 (2016). Link

[104] P. Schmidt *et al.* Remote sensing of a levitated superconductor with a flux-tunable microwave cavity. *Phys. Rev. Appl.* **22**, 014078 (2024). Link

[105] M.-A. Lemonde, N. Didier, and A. A. Clerk. Nonlinear Interaction Effects in a Strongly Driven Optomechanical Cavity. *Phys. Rev. Lett.* **111**, 053602 (2013). Link

[106] C. Laflamme and A. A. Clerk. Quantum-limited amplification with a nonlinear cavity detector. *Phys. Rev. A* **83**, 033803 (2011). Link

[107] C. A. Potts, R. C. Dekker, S. Deve, E. W. Strijbis, and G. A. Steele. Strong Intrinsic Longitudinal Coupling in Circuit Quantum Electrodynamics. *Phys. Rev. Lett.* **134**, 153603 (2025). Link

[108] A. P. Reed *et al.* Faithful conversion of propagating quantum information to mechanical motion. *Nature Physics* **13**, 1163–1167 (2017). Link

[109] E. I. Green. The story of Q. *American Scientist* **43**, 584–594 (1955). Link

[110] P. A. M. Dirac. The Principles of Quantum Mechanics. Oxford University Press, (1930). Link

[111] P. M. Morse. Vibration and sound. McGraw Hill, Inc, (1948). Link

[112] B. Hauer, C. Doolin, K. Beach, and J. Davis. A general procedure for thermomechanical calibration of nano/micro-mechanical resonators. *Annals of Physics* **339**, 181–207 (2013). Link

[113] *COMSOL Multiphysics*. Version 5.6. 2020. Link

[114] J. E. Sader, I. Larson, P. Mulvaney, and L. R. White. Method for the calibration of atomic force microscope cantilevers. *Review of Scientific Instruments* **66**, 3789–3798 (1995). Link

[115] M. Pinard, Y. Hadjar, and A. Heidmann. Effective mass in quantum effects of radiation pressure. *The European Physical Journal D - Atomic, Molecular, Optical and Plasma Physics* **7**, 107–116 (1999). Link

[116] M. Eichenfield, J. Chan, R. M. Camacho, K. J. Vahala, and O. Painter. Optomechanical crystals. *Nature* **462**, 78–82 (2009). Link

[117] S. Gröblacher *et al.* Demonstration of an ultracold micro-optomechanical oscillator in a cryogenic cavity. *Nature Physics* **5**, 485–488 (2009). Link

[118] M. Poot and H. S. van der Zant. Mechanical systems in the quantum regime. *Physics Reports* **511**, 273–335 (2012). Mechanical systems in the quantum regime. Link

[119] M. Dykman. Fluctuating nonlinear oscillators: from nanomechanics to quantum superconducting circuits. Oxford University Press, (2012). Link

[120] J. Chaste, A. Eichler, J. Moser, G. Ceballos, R. Rurali, and A. Bachtold. A nanomechanical mass sensor with yoctogram resolution. *Nature Nanotechnology* **7**, 301–304 (2012). Link

[121] M. de Jong. Dynamical behavior of trampoline membranes. *PhD thesis*. Delft University of Technology (2022). Link

[122] S. Schmid and C. Hierold. Damping mechanisms of single-clamped and prestressed double-clamped resonant polymer microbeams. *Journal of Applied Physics* **104**, 093516 (2008). Link

[123] A. Naesby, S. Naserbakht, and A. Dantan. Effects of pressure on suspended micromechanical membrane arrays. *Applied Physics Letters* **111**, 201103 (2017). Link

[124] S. Schmid, L. G. Villanueva, and M. L. Roukes. Fundamentals of Nanomechanical Resonators. 2nd. Springer International Publishing, (2016), 1–207. Link

[125] B. Suurmeijer, T. Mulder, and J. Verhoeven. Vacuum science and technology. High Tech Institute, (2016). Link

[126] C. Zener. Internal Friction in Solids. I. Theory of Internal Friction in Reeds. *Phys. Rev.* **52**, 230–235 (1937). Link

[127] T. Roszhart. The effect of thermoelastic internal friction on the Q of micromachined silicon resonators. *IEEE 4th Technical Digest on Solid-State Sensor and Actuator Workshop* 13–16 (1990). Link

[128] P.-L. Yu, T. P. Purdy, and C. A. Regal. Control of Material Damping in High-Q Membrane Microresonators. *Phys. Rev. Lett.* **108**, 083603 (2012). Link

[129] Q. P. Unterreithmeier, T. Faust, and J. P. Kotthaus. Damping of Nanomechanical Resonators. *Phys. Rev. Lett.* **105**, 027205 (2010). Link

[130] S. Schmid, K. D. Jensen, K. H. Nielsen, and A. Boisen. Damping mechanisms in high-Q micro and nanomechanical string resonators. *Phys. Rev. B* **84**, 165307 (2011). Link

[131] S. A. Fedorov *et al.* Generalized dissipation dilution in strained mechanical resonators. *Phys. Rev. B* **99**, 054107 (2019). Link

[132] D. Shin, A. Cupertino, M. H. J. de Jong, P. G. Steeneken, M. A. Bessa, and R. A. Norte. Spiderweb Nanomechanical Resonators via Bayesian Op-

timization: Inspired by Nature and Guided by Machine Learning. *Advanced Materials* **34**, 2106248 (2022). Link

[133] I. Wilson-Rae. Intrinsic dissipation in nanomechanical resonators due to phonon tunneling. *Phys. Rev. B* **77**, 245418 (2008). Link

[134] J. T. Karvonen, T. Kühn, and I. J. Maasilta. Phonon transport in suspended silicon nitride membranes at low temperatures. *Journal of Physics: Conference Series* **150**, 012019 (2009). Link

[135] G. D. Cole, I. Wilson-Rae, K. Werbach, M. R. Vanner, and M. Aspelmeyer. Phonon-tunnelling dissipation in mechanical resonators. *Nature Communications* **2**, 231 (2011). Link

[136] Y. Tsaturyan *et al.* Demonstration of suppressed phonon tunneling losses in phononic bandgap shielded membrane resonators for high-Q optomechanics. *Optics Express* **22**, 6810 (2014)

[137] Z. Li, Q. Zhang, X. You, Y. Li, and K. Peng. Suppression of phonon tunneling losses by microfiber strings for high-Q membrane microresonators. *Applied Physics Letters* **109**, 191903 (2016). Link

[138] N. P. Mauranyapin, E. Romero, R. Kalra, G. Harris, C. G. Baker, and W. P. Bowen. Tunneling of Transverse Acoustic Waves on a Silicon Chip. *Phys. Rev. Appl.* **15**, 054036 (2021). Link

[139] S. Chakram, Y. S. Patil, L. Chang, and M. Vengalattore. Dissipation in Ultrahigh Quality Factor SiN Membrane Resonators. *Phys. Rev. Lett.* **112**, 127201 (2014). Link

[140] G. S. MacCabe *et al.* Nano-acoustic resonator with ultralong phonon lifetime. *Science* **370**, 840–843 (2020). Link

[141] I. Wilson-Rae *et al.* High-Q Nanomechanics via Destructive Interference of Elastic Waves. *Phys. Rev. Lett.* **106**, 047205 (2011). Link

[142] J. Rieger, A. Isacsson, M. J. Seitner, J. P. Kotthaus, and E. M. Weig. Energy losses of nanomechanical resonators induced by atomic force microscopy-controlled mechanical impedance mismatching. *Nature Communications* **5**, 3345 (2014). Link

[143] A. Jöckel *et al.* Spectroscopy of mechanical dissipation in micro-mechanical membranes. *Applied Physics Letters* **99**, 143109 (2011). Link

[144] D. J. Wilson. Cavity Optomechanics with High-Stress Silicon Nitride Films. *PhD thesis*. California Institute of Technology (2012). Link

[145] J. M. L. Miller *et al.* Effects of Remote Boundary Conditions on Clamping Loss in Micromechanical Resonators. *Journal of Microelectromechanical Systems* **31**, 204–216 (2022). Link

[146] P. R. Saulson. Thermal noise in mechanical experiments. *Phys. Rev. D* **42**, 2437–2445 (1990). Link

[147] B. S. Berry, W. C. Pritchet, and C. E. Uzoh. Dynamical method for the thermomechanical study of thin membranes. *Journal of Vacuum Science Technology B: Microelectronics Processing and Phenomena* **7**, 1565–1569 (1989). Link

[148] Y. L. Huang and P. R. Saulson. Dissipation mechanisms in pendulums and their implications for gravitational wave interferometers. *Review of Scientific Instruments* **69**, 544–553 (1998). Link

[149] P.-L. Yu *et al.* A phononic bandgap shield for high-Q membrane microresonators. *Applied Physics Letters* **104**, 023510 (2014). Link

[150] V. A. Seleznev, S. V. Golod, A. B. Vorob'ev, E. V. Kozik, A. V. rinz, and V. Y. Prinz. Corrugated Semiconductor Nanomembranes Based on Strained Heterostructures: Fabrication and Magnetotransport. *Optoelectronics, Instrumentation and Data Processing* **60**, 488–494 (2024). Link

[151] L. Catalini, M. Rossi, E. C. Langman, and A. Schliesser. Modeling and Observation of Nonlinear Damping in Dissipation-Diluted Nanomechanical Resonators. *Phys. Rev. Lett.* **126**, 174101 (2021). Link

[152] Y. Tsaturyan, A. Barg, E. S. Polzik, and A. Schliesser. Ultracoherent nanomechanical resonators via soft clamping and dissipation dilution. *Nature Nanotechnology* **12**, 776–783 (2017). Link

[153] S. Fedorov. Mechanical resonators with high dissipation dilution in precision and quantum measurements. *PhD thesis*. EPFL (2021). Link

[154] M. J. Bereyhi *et al.* Hierarchical tensile structures with ultralow mechanical dissipation. *Nature Communications* **13**, 3097 (2022). Link

[155] L. Catalini. *Nonlinear phenomena in dissipation-diluted nanomechanical resonators*. PhD thesis. 2023. Link

[156] A. Beccari. Nanomechanical resonators with low dissipation for quantum optomechanics. *PhD thesis*. EPFL (2023). Link

[157] A. Ciers *et al.* Nanomechanical Crystalline AlN Resonators with High Quality Factors for Quantum Optoelectromechanics. *Advanced Materials* **36**, 2403155 (2024). Link

[158] M. Göppl *et al.* Coplanar waveguide resonators for circuit quantum electrodynamics. *Journal of Applied Physics* **104**, 113904 (2008). Link

[159] D. Pozar. Microwave engineering. 4th. Wiley, (1990). Link

[160] M. Morita, T. Ohmi, E. Hasegawa, M. Kawakami, and M. Ohwada. Growth of native oxide on a silicon surface. *Journal of Applied Physics* **68**, 1272–1281 (1990). Link

[161] C. R. H. McRae *et al.* Materials loss measurements using superconducting microwave resonators. *Review of Scientific Instruments* **91**, 091101 (2020). Link

[162] C. W. Gardiner and M. J. Collett. Input and output in damped quantum systems: Quantum stochastic differential equations and the master equation. *Phys. Rev. A* **31**, 3761–3774 (1985). Link

[163] F. F. Walls and G. J. Milburn. Quantum Optics. 2nd ed. Springer, (2008). Link

[164] W. Bowen and G. J. Milburn. Quantum Optomechanics. CRC Press, (2016). Link

[165] G. A. Peterson *et al.* Ultrastrong Parametric Coupling between a Superconducting Cavity and a Mechanical Resonator. *Phys. Rev. Lett.* **123**, 247701 (2019). Link

[166] L. Bakemeier, A. Alvermann, and H. Fehske. Route to Chaos in Optomechanics. *Phys. Rev. Lett.* **114**, 013601 (2015). Link

[167] F. Monifi *et al.* Optomechanically induced stochastic resonance and chaos transfer between optical fields. *Nature Photonics* **10**, 399–405 (2016). Link

[168] S. Meilof. Reducing the Gap Distance in a Microwave Cavity Flipchip Device. *MSc thesis*. Delft University of Technology (2024). Link

[169] Z. M. et al. *Qiskit Metal: An Open-Source Framework for Quantum Device Design Analysis*. Version 0.1.5a1. 2021. Link

[170] *Ansys HFSS*. Version 2020 R2. 2020. Link

[171] M. F. Gely and G. A. Steele. QuCAT: quantum circuit analyzer tool in Python. *New Journal of Physics* **22**, 013025 (2020). Link

[172] R. Meservey and P. M. Tedrow. Measurements of the Kinetic Inductance of Superconducting Linear Structures. *Journal of Applied Physics* **40**, 2028–2034 (1969). Link

[173] A. J. Annunziata *et al.* Tunable superconducting nanoinductors. *Nanotechnology* **21**, 445202 (2010). Link

[174] S. Hawaldar. *forked from qiskit-community/qiskit-metal*. Version 0.8.5.5. 2025. Link

[175] S. Hawaldar. *forked from zlatko-minev/pyEPR*. Version 0.0.4. 2025. Link

[176] C. Gorter. Chapter I The Two Fluid Model for Superconductors and Helium II. Vol. 1. *Progress in Low Temperature Physics*. Elsevier, (1955), 1–16. Link

[177] J. Bardeen. Two-Fluid Model of Superconductivity. *Phys. Rev. Lett.* **1**, 399–400 (1958). Link

[178] P. Drude. Zur Elektronentheorie der Metalle. *Annalen der Physik* **306**, 566–613 (1900). Link

[179] M. R. Rafique, I. Kataeva, H. Engseth, M. Tarasov, and A. Kidiyarova-Shevchenko. Optimization of superconducting microstrip interconnects for

rapid single-flux-quantum circuits. *Superconductor Science and Technology* **18**, 1065 (2005). Link

[180] M. Tinkham. Introduction to superconductivity. McGraw Hill, (1996), 454. Link

[181] D. J. Thoen, B. G. C. Bos, E. A. F. Haalebos, T. M. Klapwijk, J. J. A. Baselmans, and A. Endo. Superconducting NbTin Thin Films With Highly Uniform Properties Over a ∅ 100 mm Wafer. *IEEE Transactions on Applied Superconductivity* **27**, 1–5 (2017)

[182] A. I. Gubin, K. S. Il'in, S. A. Vitusevich, M. Siegel, and N. Klein. Dependence of magnetic penetration depth on the thickness of superconducting Nb thin films. *Phys. Rev. B* **72**, 064503 (2005). Link

[183] V. G. Kogan. Interaction of vortices in thin superconducting films and the Berezinskii-Kosterlitz-Thouless transition. *Phys. Rev. B* **75**, 064514 (2007). Link

[184] Q. P. de Montserrat. Study of the penetration depth in thin aluminium layers. *BSc thesis*. Universitat Autònoma de Barcelona (2022). Link

[185] J. Koch *et al.* Charge-insensitive qubit design derived from the Cooper pair box. *Phys. Rev. A* **76**, 042319 (2007). Link

[186] W. J. M. Franse. Quantum Acoustics with high-overtone bulk resonators and superconducting qubits High-Q planar devices, phonon lasers, and quantum ghosts. *PhD thesis*. Delft University of Technology (2024). Link

[187] J. D. Koenig. Parametrically Activated Interactions in Circuit Quantum Electrodynamical Systems. *PhD thesis*. Delft University of Technology (2025). Link

[188] R. Igreja and C. Dias. Analytical evaluation of the interdigital electrodes capacitance for a multi-layered structure. *Sensors and Actuators A: Physical* **112**, 291–301 (2004). Link

[189] G. González, E. S. Kolosovas-Machuca, E. López-Luna, H. Hernández-Arriaga, and F. J. González. Design and Fabrication of Interdigital Nanocapacitors Coated with HfO2. *Sensors* **15**, 1998–2005 (2015). Link

[190] N. van Huijkelom. Increasing the Optomechanical Coupling between a Superconducting Microwave Cavity and a Mechanical Resonator. *MSc thesis*. Delft University of Technology (2022). Link

[191] *Kavli Nanolab Delft*. [Online, accessed 21-04-2025]. Link

[192] A. Megrant *et al.* Planar superconducting resonators with internal quality factors above one million. *Applied Physics Letters* **100**, 113510 (2012). Link

[193] J. M. Sage, V. Bolkhovsky, W. D. Oliver, B. Turek, and P. B. Welander. Study of loss in superconducting coplanar waveguide resonators. *Journal of Applied Physics* **109**, 063915 (2011). Link

[194] A. Premkumar *et al.* Microscopic relaxation channels in materials for superconducting qubits. *Communications Materials* **2**, 72 (2021). Link

[195] R. Barends *et al.* Contribution of dielectrics to frequency and noise of NbTiN superconducting resonators. *Applied Physics Letters* **92**, 223502 (2008). Link

[196] R. Barends *et al.* Noise in NbTiN, Al, and Ta Superconducting Resonators on Silicon and Sapphire Substrates. *IEEE Transactions on Applied Superconductivity* **19**, 936–939 (2009). Link

[197] *Netherlands Institute for Space Research.* [Online; accessed 21-04-2025]. Link

[198] H. G. Leduc *et al.* Titanium nitride films for ultrasensitive microresonator detectors. *Applied Physics Letters* **97**, 102509 (2010). Link

[199] H. K. Lee, K. S. Chung, and J. S. Yu. Selective Etching of Thick Si3N4, SiO2 and Si by Using CF4/O2 and C2F6 Gases with or without O2 or Ar Addition. *Journal of the Korean Physical Society* **54**, 1816–1823 (2009). Link

[200] N. Burham, G. Sugandi, M. M. Nor, and B. Y. Majlis. Effect of temperature on the etching rate of nitride and oxide layer using Buffered Oxide Etch. *2016 International Conference on Advances in Electrical, Electronic and Systems Engineering (ICAEES)* 516–519 (2016). Link

[201] G. J. Dolan. Offset masks for lift-off photoprocessing. *Applied Physics Letters* **31**, 337–339 (1977). Link

[202] G. Dolan and J. Dunsmuir. Very small (20 nm) lithographic wires, dots, rings, and tunnel junctions. *Physica B: Condensed Matter* **152**, 7–13 (1988). Link

[203] A. Potts, G. Parker, J. Baumberg, and P. de Groot. CMOS compatible fabrication methods for submicron Josephson junction qubits. *IEE Proceedings - Science, Measurement and Technology* **148**, 225–228 (2001). Link

[204] M. V. Costache, G. Bridoux, I. Neumann, and S. O. Valenzuela. Lateral metallic devices made by a multiangle shadow evaporation technique. *Journal of Vacuum Science Technology B* **30**, 04E105 (2012). Link

[205] J. M. Kreikebaum, K. P. O'Brien, A. Morvan, and I. Siddiqi. Improving wafer-scale Josephson junction resistance variation in superconducting quantum coherent circuits. *Superconductor Science and Technology* **33**, 06LT02 (2020). Link

[206] A. Osman *et al.* Simplified Josephson-junction fabrication process for reproducibly high-performance superconducting qubits. *Applied Physics Letters* **118**, 064002 (2021). Link

[207] P. Duivestein. *Wafer scale fabrication of Josephson junctions*. MSc thesis. Delft University of Technology, 2021. Link

[208] N. Muthusubramanian *et al.* Wafer-scale uniformity of Dolan-bridge and bridgeless Manhattan-style Josephson junctions for superconducting quantum processors. *Quantum Science and Technology* **9**, 025006 (2024). Link

[209] A. Gupta and J. Leck. An evaluation of the titanium sublimation pump. *Vacuum* **25**, 362–372 (1975). Link

[210] H. Younan, X. Z. Xiang, and L. Xiaomin. Characterization studies of fluorine-induced corrosion crystal defects on microchip Al bondpads using X-ray photoelectron spectroscopy. *Proceedings of the 21th International Symposium on the Physical and Failure Analysis of Integrated Circuits (IPFA)* 90–93 (2014). Link

[211] S. K. Pani, R. H. Hogan, M. Pandurangan, and R. R. Nistala. Crystalline defect formation on aluminum bond pads during CMOS wafer storage and process strategies for defect elimination. *Journal of Vacuum Science Technology B* **36**, 031202 (2018). Link

[212] D. H. Douglass and R. Meservey. Energy Gap Measurements by Tunneling Between Superconducting Films. I. Temperature Dependence. *Phys. Rev.* **135**, A19–A23 (1964). Link

[213] V. Ambegaokar and A. Baratoff. Tunneling Between Superconductors. *Phys. Rev. Lett.* **10**, 486–489 (1963). Link

[214] S. Kono. Quantum Measurement of Itinerant Microwave Photons Using Superconducting Circuits. *PhD thesis*. University of Tokyo (2019). Link

[215] A. Pamp and G. G. A. and. Deformation of bowed silicon chips due to adhesion and applied pressure. *Journal of Adhesion Science and Technology* **21**, 1021–1043 (2007). Link

[216] C.-M. Gärtner. Advanced membrane architectures for multimode optomechanics. *PhD thesis*. University of Vienna (2020). Link

[217] *Norcada - A MEMS Technology Company*. [Online; accessed 07-03-2025]. Link

[218] W. Flechsig. Kathodenstrahlröhre zur Erzeugung mehrfarbiger Bilder auf einem Leuchtschirm. *German Reich Patent 736,575*. 1943

[219] M. A. Cohen. Optomechanics in a 3D microwave cavity. *PhD thesis*. Delft University of Technology (2019). Link

[220] J. H. Lau. Recent Advances and New Trends in Flip Chip Technology. *Journal of Electronic Packaging* **138**, 030802 (2016). Link

[221] D. J. Wilson, C. A. Regal, S. B. Papp, and H. J. Kimble. Cavity Optomechanics with Stoichiometric SiN Films. *Phys. Rev. Lett.* **103**, 207204 (2009). Link

[222] M. Rossi, D. Mason, J. Chen, Y. Tsaturyan, and A. Schliesser. Measurement-based quantum control of mechanical motion. *Nature* **563**, 53–58 (2018). Link

[223] M. Rossi, D. Mason, J. Chen, and A. Schliesser. Observing and Verifying the Quantum Trajectory of a Mechanical Resonator. *Phys. Rev. Lett.* **123**, 163601 (2019). Link

[224] D. Mason, J. Chen, M. Rossi, Y. Tsaturyan, and A. Schliesser. Continuous force and displacement measurement below the standard quantum limit. *Nature Physics* **15**, 745–749 (2019). Link

[225] J. Chen, M. Rossi, D. Mason, and A. Schliesser. Entanglement of propagating optical modes via a mechanical interface. *Nature Communications* **11**, 943 (2020). Link

[226] D. Hälg *et al.* Membrane-Based Scanning Force Microscopy. *Phys. Rev. Appl.* **15**, L021001 (2021). Link

[227] W. Whyte. Cleanroom Technology: Fundamentals of Design, Testing and Operation. Electronic and electrical engineering. Wiley, (2001). Link

[228] S. Linge Johnsen, J. Bollmann, H. Lee, and Y. Zhou. Accurate representation of interference colours (Michel–Lévy chart): from rendering to image colour correction. *Journal of Microscopy* **269**, 321–337 (2018). Link

[229] M. de Wit *et al.* Vibration isolation with high thermal conductance for a cryogen-free dilution refrigerator. *Review of Scientific Instruments* **90**, 015112 (2019). Link

[230] G. R. Fowles and G. L. Cassiday. Analytical Mechanics. 7th ed. Thomson Learning, Inc., (2005)

[231] Q. D. Team. *Qucs: Quite Universal Circuit Simulator*. Version 0.0.19. 2017. Link

[232] *Supercon, Inc.* [Online; accessed 23-04-2025]. Link

[233] A. M. Den Haan *et al.* Atomic resolution scanning tunneling microscopy in a cryogen free dilution refrigerator at 15 mK. *Rev. Sci. Instrum.* **85**, 035112 (2014). Link

[234] D. Niepce, J. J. Burnett, M. Kudra, J. H. Cole, and J. Bylander. Stability of superconducting resonators: Motional narrowing and the role of Landau-Zener driving of two-level defects. *Sci. Adv.* **7**, eabh0462 (2021). Link

[235] R. T. Learn, E. Varga, V. Vadakkumbatt, and J. P. Davis. Precision measurements of the zero-temperature dielectric constant and density of liquid ^{4}He. *Phys. Rev. B* **106**, 214509 (2022). Link

[236] B. L. Brock, M. P. Blencowe, and A. J. Rimberg. Frequency Fluctuations in Tunable and Nonlinear Microwave Cavities. *Phys. Rev. Appl.* **14**, 054026 (2020). Link

[237] C. Müller, J. Lisenfeld, A. Shnirman, and S. Poletto. Interacting two-level defects as sources of fluctuating high-frequency noise in superconducting circuits. *Phys. Rev. B* **92**, 035442 (2015). Link

[238] F. M. Buters *et al.* High-Q nested resonator in an actively stabilized optomechanical cavity. *Appl. Phys. Lett.* **110**, 104104 (2017). Link

[239] T. J. Clark, V. Vadakkumbatt, F. Souris, H. Ramp, and J. P. Davis. Cryogenic microwave filter cavity with a tunability greater than 5 GHz. *Rev. Sci. Instrum.* **89**, 114704 (2018). Link

[240] C. Lee *et al.* Vibration Mitigation for a Cryogen-Free Dilution Refrigerator for the AMoRE-Pilot Experiment. *J. Low Temp. Phys.* **193**, 786–792 (2018). Link

[241] S. Kanhirathingal *et al.* Feedback Stabilization of the Resonant Frequency in a Tunable Microwave Cavity with Single-Photon Occupancy. *Phys. Rev. Appl.* **18**, 064033 (2022). Link

[242] A. Vepsäläinen *et al.* Improving qubit coherence using closed-loop feedback. *Nat. Commun* **13**, 1932 (2022). Link

[243] R. V. Pound. Electronic frequency stabilization of microwave oscillators. *Rev. Sci. Instrum.* **17**, 490–505 (1946). Link

[244] R. W. P. Drever *et al.* Laser phase and frequency stabilization using an optical resonator. *Appl. Phys. B* **31**, 97–105 (1983). Link

[245] G. C. Bjorklund, M. D. Levenson, W. Lenth, and C. Ortiz. Frequency modulation (FM) spectroscopy: theory of lineshapes and signal-to-noise analysis. *Appl. Phys. B* **32**, 145–152 (1983). Link

[246] E. D. Black. An introduction to Pound–Drever–Hall laser frequency stabilization. *Am. J Phys.* **69**, 79–87 (2001). Link

[247] T. Carmon, T. J. Kippenberg, L. Yang, H. Rokhsari, S. Spillane, and K. J. Vahala. Feedback control of ultra-high-Q microcavities: application to micro-Raman lasers and microparametric oscillators. *Opt. Express* **13**, 3558 (2005). Link

[248] S. A. Fedorov, A. Beccari, A. Arabmoheghi, D. J. Wilson, N. J. Engelsen, and T. J. Kippenberg. Thermal intermodulation noise in cavity-based measurements. *Optica* **7**, 1609–1616 (2020). Link

[249] *Red Pitaya.* [Online; accessed 09-03-2023]. Link

[250] D. Rieger, S. Günzler, M. Spiecker, A. Nambisan, W. Wernsdorfer, and I. Pop. Fano Interference in Microwave Resonator Measurements. *Phys. Rev. Appl.* **20**, 014059 (2023). Link

[251] S. Weis *et al.* Optomechanically Induced Transparency. *Science* **330**, 1520–1523 (2010). Link

[252] A. H. Safavi-Naeini *et al.* Electromagnetically induced transparency and slow light with optomechanics. *Nature* **472**, 69–73 (2011). Link

[253] G. Anetsberger *et al.* Measuring nanomechanical motion with an imprecision below the standard quantum limit. *Phys. Rev. A* **82**, 061804 (2010). Link

[254] R. W. Peterson *et al.* Laser Cooling of a Micromechanical Membrane to the Quantum Backaction Limit. *Phys. Rev. Lett.* **116**, 063601 (2016). Link

[255] J. M. Fink *et al.* Quantum electromechanics on silicon nitride nanomembranes. *Nature Communications* **7**, 12396 (2016). Link

[256] W. Jiang *et al.* Efficient bidirectional piezo-optomechanical transduction between microwave and optical frequency. *Nature Communications* **11**, 1166 (2020). Link

[257] R. Fischer *et al.* Optical probing of mechanical loss of a Si3N4 membrane below 100 mK. (2016). Link

[258] E. Hebestreit, M. Frimmer, R. Reimann, C. Dellago, F. Ricci, and L. Novotny. Calibration and energy measurement of optically levitated nanoparticle sensors. *Review of Scientific Instruments* **89**, (2018). Link

[259] T. Briant *et al.* Photonic and Optomechanical Thermometry. *Optics* **3**, 159–176 (2022). Link

[260] H. Liu, H. Brahmi, C. Boix-Constant, H. S. J. van der Zant, P. G. Steeneken, and G. J. Verbiest. Optomechanical methodology for characterizing the thermal properties of 2D materials. *APL Materials* **12**, 021126 (2024). Link

[261] J. D. Teufel, J. W. Harlow, C. A. Regal, and K. W. Lehnert. Dynamical Backaction of Microwave Fields on a Nanomechanical Oscillator. *Phys. Rev. Lett.* **101**, 197203 (2008). Link

[262] T. P. Purdy, R. W. Peterson, P.-L. Yu, and C. A. Regal. Cavity optomechanics with Si3N4 membranes at cryogenic temperatures. *New Journal of Physics* **14**, 115021 (2012). Link

[263] A. Chowdhury *et al.* Calibrated quantum thermometry in cavity optomechanics. *Quantum Science and Technology* **4**, 024007 (2019). Link

[264] M. Fleischhauer, A. Imamoglu, and J. P. Marangos. Electromagnetically induced transparency: Optics in coherent media. *Rev. Mod. Phys.* **77**, 633–673 (2005). Link

[265] V. Singh, S. J. Bosman, B. H. Schneider, Y. M. Blanter, A. Castellanos-Gomez, and G. A. Steele. Optomechanical coupling between a multilayer graphene mechanical resonator and a superconducting microwave cavity. *Nature Nanotechnology* **9**, 820–824 (2014). Link

[266] T. Rocheleau, T. Ndukum, C. Macklin, J. B. Hertzberg, A. A. Clerk, and K. C. Schwab. Preparation and detection of a mechanical resonator near the ground state of motion. *Nature* **463**, 72–75 (2010). Link

[267] A. A. Clerk, M. H. Devoret, S. M. Girvin, F. Marquardt, and R. J. Schoelkopf. Introduction to quantum noise, measurement, and amplification. *Rev. Mod. Phys.* **82**, 1155–1208 (2010). Link

[268] R. Maisonobe *et al.* Vibration decoupling system for massive bolometers in dry cryostats. *Journal of Instrumentation* **13**, T08009 (2018). Link

[269] M. Rossi. Quantum Measurement and Control of a Mechanical Resonator. *PhD thesis*. University of Copenhagen (2020). Link

[270] J. S. Huber *et al.* Spectral Evidence of Squeezing of a Weakly Damped Driven Nanomechanical Mode. *Phys. Rev. X* **10**, 021066 (2020). Link

[271] F. Fani Sani, I. C. Rodrigues, D. Bothner, and G. A. Steele. Level attraction and idler resonance in a strongly driven Josephson cavity. *Phys. Rev. Res.* **3**, 043111 (2021). Link

[272] M. S. Khalil, M. J. A. Stoutimore, F. C. Wellstood, and K. D. Osborn. An analysis method for asymmetric resonator transmission applied to superconducting devices. *Journal of Applied Physics* **111**, 054510 (2012). Link

[273] D. Rieger, S. Günzler, M. Spiecker, A. Nambisan, W. Wernsdorfer, and I. Pop. Fano Interference in Microwave Resonator Measurements. *Phys. Rev. Appl.* **20**, 014059 (2023). Link

[274] A. H. Nayfeh and D. T. Mook. Nonlinear Oscillations. Wiley, (2024). Link

[275] P. Krantz, M. Kjaergaard, F. Yan, T. P. Orlando, S. Gustavsson, and W. D. Oliver. A quantum engineer's guide to superconducting qubits. *Applied Physics Reviews* **6**, 021318 (2019). Link

[276] T. Yamamoto *et al.* Flux-driven Josephson parametric amplifier. *Applied Physics Letters* **93**, 042510 (2008). Link

[277] G. Kirchmair *et al.* Observation of quantum state collapse and revival due to the single-photon Kerr effect. *Nature* **495**, 205–209 (2013). Link

[278] J. Bourassa, F. Beaudoin, J. M. Gambetta, and A. Blais. Josephson-junction-embedded transmission-line resonators: From Kerr medium to in-line transmon. *Phys. Rev. A* **86**, 013814 (2012). Link

[279] C. K. Andersen, A. Kamal, N. A. Masluk, I. M. Pop, A. Blais, and M. H. Devoret. Quantum Versus Classical Switching Dynamics of Driven Dissipative Kerr Resonators. *Phys. Rev. Appl.* **13**, 044017 (2020). Link

[280] T. Yamaji *et al.* Spectroscopic observation of the crossover from a classical Duffing oscillator to a Kerr parametric oscillator. *Phys. Rev. A* **105**, 023519 (2022). Link

[281] B. Yurke *et al.* Observation of 4.2-K equilibrium-noise squeezing via a Josephson-parametric amplifier. *Phys. Rev. Lett.* **60**, 764–767 (1988). Link

[282] B. Yurke *et al.* Observation of parametric amplification and deamplification in a Josephson parametric amplifier. *Phys. Rev. A* **39**, 2519–2533 (1989). Link

[283] I. Siddiqi *et al.* RF-Driven Josephson Bifurcation Amplifier for Quantum Measurement. *Phys. Rev. Lett.* **93**, 207002 (2004). Link

[284] R. Vijay, M. H. Devoret, and I. Siddiqi. Invited Review Article: The Josephson bifurcation amplifier. *Review of Scientific Instruments* **80**, 111101 (2009). Link

[285] A. J. Hoffman *et al.* Dispersive Photon Blockade in a Superconducting Circuit. *Phys. Rev. Lett.* **107**, 053602 (2011). Link

[286] P. E. Schmidt. Nanomechanical Quantum Systems. *PhD thesis*. Technische Universität München (2020). Link

[287] L. Catalini *et al.* Slow and fast topological dynamical phase transitions in a Duffing resonator driven by two detuned tones. *Phys. Rev. Res.* **7**, 033058 (2025). Link

[288] G. Stan, S. B. Field, and J. M. Martinis. Critical Field for Complete Vortex Expulsion from Narrow Superconducting Strips. *Phys. Rev. Lett.* **92**, 097003 (2004). Link

[289] C. Song *et al.* Microwave response of vortices in superconducting thin films of Re and Al. *Phys. Rev. B* **79**, 174512 (2009). Link

[290] A. Kremen, N. Wissberg Shaiand Haham, E. Persky, Y. Frenkel, and B. Kalisky. Mechanical Control of Individual Superconducting Vortices. *Nano Letters* **16**, 1626–1630 (2016). Link

[291] S. K. Sahu, S. Mandal, S. Ghosh, M. M. Deshmukh, and V. Singh. Superconducting Vortex-Charge Measurement Using Cavity Electromechanics. *Nano Letters* **22**, 1665–1671 (2022). Link

[292] T. Luschmann *et al.* Mechanical frequency control in inductively coupled electromechanical systems. *Scientific Reports* **12**, 1608 (2022). Link

[293] W. M. van Weerdenburg *et al.* Extreme enhancement of superconductivity in epitaxial aluminum near the monolayer limit. *Science Advances* **9**, eadf5500 (2023). Link

[294] I. C. Rodrigues, D. Bothner, and G. A. Steele. Cooling photon-pressure circuits into the quantum regime. *Science Advances* **7**, eabg6653 (2021). Link

[295] I. C. Rodrigues, G. A. Steele, and D. Bothner. Parametrically enhanced interactions and nonreciprocal bath dynamics in a photon-pressure Kerr amplifier. *Science Advances* **8**, eabq1690 (2022). Link

[296] B. Yurke and E. Buks. Performance of Cavity-Parametric Amplifiers, Employing Kerr Nonlinearites, in the Presence of Two-Photon Loss. *Journal of Lightwave Technology* **24**, 5054–5066 (2006)

[297] S. Boutin, D. M. Toyli, A. V. Venkatramani, A. W. Eddins, I. Siddiqi, and A. Blais. Effect of Higher-Order Nonlinearities on Amplification and Squeezing in Josephson Parametric Amplifiers. *Phys. Rev. Appl.* **8**, 054030 (2017). Link

[298] N. Lauk *et al.* Perspectives on quantum transduction. *Quantum Science and Technology* **5**, 020501 (2020). Link

[299] M. Mirhosseini, A. Sipahigil, M. Kalaee, and O. Painter. Superconducting qubit to optical photon transduction. *Nature* **588**, 599–603 (2020). Link

[300] H. Eleuch and I. Rotter. Exceptional points in open and pt-symmetric systems. *Acta Polytechnica* **54**, 106–112 (2014). Link

[301] N. R. Bernier, E. G. Dalla Torre, and E. Demler. Unstable Avoided Crossing in Coupled Spinor Condensates. *Phys. Rev. Lett.* **113**, 065303 (2014). Link

[302] N. R. Bernier, L. D. Tóth, A. K. Feofanov, and T. J. Kippenberg. Level attraction in a microwave optomechanical circuit. *Phys. Rev. A* **98**, 023841 (2018). Link

[303] M.-A. Miri and A. Alù. Exceptional points in optics and photonics. *Science* **363**, eaar7709 (2019). Link

[304] S. Yanai. Coherence and nonlinearity in mechanical and Josephson superconducting devices. *PhD thesis*. Delft University of Technology (2018). Link

[305] M. Gely. Measuring and controlling radio-frequency quanta with superconducting circuits. *PhD thesis*. Delft University of Technology (2020). Link

[306] L. F. Deeg, D. Zoepfl, N. Diaz-Naufal, M. L. Juan, A. Metelmann, and G. Kirchmair. Optomechanical backaction in the bistable regime. *Phys. Rev. Appl.* **23**, 014082 (2025). Link

[307] S. Hofer. Quantum Control of Optomechanical Systems. *PhD thesis*. University of Vienna (2015). Link



ISBN 978-94-6384-864-0